



**INSTITUTO POTOSINO DE INVESTIGACIÓN
CIENTÍFICA Y TECNOLÓGICA, A.C.**

POSGRADO EN CONTROL Y SISTEMAS DINÁMICOS

**Synchronization of a Distributed Power
Generation System with the Electric Grid by
means of Current Injection**

Tesis que presenta

Erick Israel Vázquez Oviedo

Para obtener el grado de

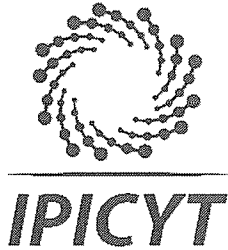
Doctor en Control y Sistemas Dinámicos

Directores de la Tesis:

Dr. Alejandro Ricardo Femat Flores

Dr. Nimrod Vázquez Nava

San Luis Potosí, S.L.P., enero de 2019



Constancia de aprobación de la tesis

La tesis “*Synchronization of a Distributed Power Generation System with the Electric Grid by means of Current Injection*” presentada para obtener el Grado de Doctor en Control y Sistemas Dinámicos, fue elaborada por **Erick Israel Vázquez Oviedo** y aprobada el **diecisiete de enero del dos mil diecinueve** por los suscritos, designados por el Colegio de Profesores de la División de Matemáticas Aplicadas del Instituto Potosino de Investigación Científica y Tecnológica, A.C.



Dr. Alejandro Ricardo Femat Flores
Codirector de la tesis



Dr. Nimrod Vázquez Nava
Codirector de la tesis



Dr. Cesar Octavio Maldonado Ahumada
Jurado en el Examen



Dr. Jesús Leyva Ramos
Jurado en el Examen



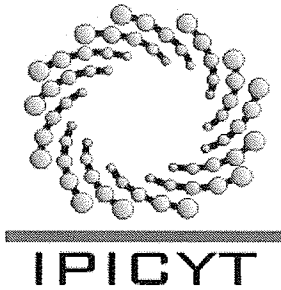
Dr. Diego Langarica Córdoba
Jurado en el Examen



Institutional Credits

This dissertation was elaborated in the Division of the Applied Mathematics of the Instituto Potosino de Investigación Científica y Tecnológica (IPICYT), A.C, under the supervision of Dr. Alejandro Ricardo Femat Flores and in the Energy Quality Laboratory of the Instituto Tecnológico de Celaya, under the supervision of Dr. Nimrod Vázquez Nava.

During this period, the author received an academic scholarship from the National Council of Science and Technology (CONACYT) #264045, and from the IPICYT, A.C.



Instituto Potosino de Investigación Científica y Tecnológica, A.C.

Acta de Examen de Grado

El Secretario Académico del Instituto Potosino de Investigación Científica y Tecnológica, A.C., certifica que en el Acta 007 del Libro Primero de Actas de Exámenes de Grado del Programa de Doctorado en Control y Sistemas Dinámicos está asentado lo siguiente:

En la ciudad de San Luis Potosí a los 17 días del mes de enero del año 2019, se reunió a las 10:00 horas en las instalaciones del Instituto Potosino de Investigación Científica y Tecnológica, A.C., el Jurado integrado por:

Dr. Jesús Leyva Ramos	Presidente	IPICYT
Dr. Alejandro Ricardo Femat Flores	Secretario	IPICYT
Dr. Cesar Octavio Maldonado Ahumada	Sinodal	IPICYT
Dr. Diego Langarica Córdoba	Sinodal externo	UASLP
Dr. Nimrod Vázquez Nava	Sinodal externo	ITCELAYA

a fin de efectuar el examen, que para obtener el Grado de:

DOCTOR EN CONTROL Y SISTEMAS DINÁMICOS

sustentó el C.

Erick Israel Vázquez Oviedo

sobre la Tesis intitulada:

Synchronization of a Distributed Power Generation System with the Electric Grid by means of Current Injection

que se desarrolló bajo la dirección de

Dr. Alejandro Ricardo Femat Flores
Dr. Nimrod Vázquez Nava (ITCELAYA)

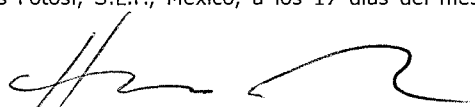
El Jurado, después de deliberar, determinó

APROBARLO

Dándose por terminado el acto a las 12:05 horas, procediendo a la firma del Acta los integrantes del Jurado. Dando fe el Secretario Académico del Instituto.

A petición del interesado y para los fines que al mismo convengan, se extiende el presente documento en la ciudad de San Luis Potosí, S.L.P., México, a los 17 días del mes de enero de 2019.


Mtra. Ivonne Lizette Cuevas Vélez
Jefa del Departamento del Posgrado


Dr. Horacio Flores Zúñiga
Secretario Académico



*To all those who
love me, in special
to my mother
of whose authentic gray hairs
not a few were caused by me*

Acknowledgments

I would like to express my gratitude to my mother Yolanda Oviedo Hernandez for the values transmitted to me. It might had been almost impossible to get to this stage of my life without her unconditional support and inspiration.

Moreover, I would like to thank my advisors Dr. Nimrod Vázquez Nava and Dr. Alejandro Ricardo Femat Flores for their tremendous support, motivation and help during my doctoral education, because they shared their knowledge and guided me through the scientific research path. I really appreciate their friendship and time.

I would also like to thank Dr. Josep M. Guerrero for his important contribution to this dissertation and support during my stay in Aalborg University, Denmark.

I also want to thank the members of the electronic department of the Technological Center of Celaya, who added a lot of value and strength to my professional development. They supported and provided me with all their hospitality during my stay in that Technological Center.

To all the researchers and technicians of the Applied Mathematics Division from IPICYT, for transmitting an important host of invaluable knowledge, which has been a great help for me.

Finally, I also acknowledge CONACYT for the financial support provided (No. of scholarship: 264045).

Contents

1. INTRODUCTION	1
1.1 Distributed Power Generation Systems	1
1.2 Faults Classification in Three-Phase Systems.....	3
1.3 Motivation, Hypothesis, and Objectives	14
1.4 Structure of the manuscript.....	15
2. SYNCHRONIZATION SYSTEMS FOR THE ELECTRIC GRID	16
2.1 Zero Crossing Detector (ZCD).....	16
2.2 Phase Locked Loop (PLL)	17
2.3 Enhanced Phase Locked Loop (EPLL).....	19
2.4 Quadrature Phase Locked Loop (QPLL)	20
2.5 Second Order Generalized Integrator-Phase Locked Loop (SOGI-PLL)	22
2.6 Second Order Generalized Integrator-Frequency Locked Loop (SOGI-FLL)	23
2.7 Adaptive Notch Filter (ANF).....	24
3. LIMIT CYCLE OSCILLATOR – FREQUENCY LOCKED LOOP (LCO-FLL) ...	26
3.1 The Limit Cycle Oscillator	27
3.2 The Interconnection of LCO-FLL	29
3.3 Stability Analysis of LCO-FLL	31
3.4 Synchronization Stability Numerical Analysis of the LCO-FLL.....	32
3.5 Three-Phase LCO-FLL Case and Sequence-Components Detection	35
3.6 Experimental Results.....	37
3.7 Harmonic Detection System for Critical Loads, an application of the LCO-FLL	48
3.8 Harmonic Detection Tests Simulation.....	49
3.9 Remarks on LCO-FLL	51
4. CURRENT CONTROL BASED ON LYAPUNOV THEORY AND LCO	53

4.1	Active Power Strategies	56
4.1.1	Balanced Injected Current Strategy.....	56
4.1.2	Constant Active Power Strategy.....	57
4.2	Lyapunov Control Law	58
4.3	Current Control for the Inverter-Grid Connected System.....	62
4.4	Simulation Results.....	63
4.5	Experimental Test Results.....	66
4.6	Comparison with other schemes	70
4.7	Remarks on Current Control.....	71
5.	MODIFIED SANDIA VOLTAGE SHIFT ANTI-ISLANDING TECHNIQUE	73
5.1	Modified Sandia Voltage Shift.....	75
5.2	Experimental Tests.....	77
5.3	Remarks on MSVS	79
6.	RE-CONNECTION OF A DPGS TO THE GRID NETWORK WITH A CRITICAL LOAD.....	80
6.1	Proposed DPGS System with Islanding Capability	81
6.2	Simulation tests	84
7.	CONCLUSION AND FINAL REMARKS.....	89
7.1	Future Work.....	91
8.	REFERENCES	93
9.	APPENDIX.....	101
9.1	Lyapunov stability analysis of LCO	101
9.2	Technical specifications.....	102

Resumen

Esta tesis desarrolla un nuevo sistema capaz de manejar o incluso rechazar perturbaciones de la red eléctrica para establecer una interconexión y sincronización confiable, efectiva y segura entre un Sistema de Generación de Potencia Distribuida (DPGS) y la red eléctrica. En este sentido, se presenta una nueva técnica de sincronización de convertidores de potencia basada en un Oscilador de Ciclo Límite (LCO) y un lazo de amarre en frecuencia (FLL), el cual hace que la frecuencia del sistema sea adaptable. La técnica propuesta LCO-FLL ofrece un alto grado de inmunidad y robustez frente a perturbaciones en el nivel de voltaje, armónicos y cambios de fase y frecuencia. El LCO-FLL tiene la ventaja de realizar la sincronía con la red desde cualquier condición inicial establecida para el LCO, asegurando un transitorio aceptable en el proceso de sincronización. Otras ventajas del esquema propuesto son que no requiere un lazo de amarre en fase (PLL), ni funciones trigonométricas y proporciona información útil para estimar las componentes de secuencia positiva y negativa de una red trifásica altamente contaminada. Además, se presenta un análisis de estabilidad local y un análisis numérico del LCO-FLL. El comportamiento y el rendimiento de la técnica propuesta se comparan con técnicas de sincronización actuales mediante resultados experimentales. Asimismo, una aplicación trifásica de la técnica de sincronización se evalúa experimentalmente. Se describe el funcionamiento y desarrollo de un controlador basado en teoría no lineal, en combinación con una ley de control de Lyapunov, la cual proporciona estabilidad para el correcto funcionamiento de un sistema fotovoltaico (PV) conectado a la red. Igualmente se garantiza una inyección de corriente eficiente y una regulación de potencia activa con una ley de control de orden menor en comparación con otras técnicas de control. El modelo de control propuesto ofrece un alto grado de inmunidad y robustez contra perturbaciones en la red, gracias a la técnica de sincronización LCO-FLL. Este LCO-FLL calcula las componentes de secuencia positiva y negativa, que son utilizados por la ley de control de Lyapunov para controlar las corrientes inyectadas a la red, así también se considera la tensión de entrada del inversor en el diseño del controlador. Este control es probado mediante dos estrategias de manejo de la energía: corrientes inyectadas equilibradas y potencia activa constante en presencia de una red desbalanceada. Se presentan pruebas experimentales y de simulación para demostrar la fiabilidad y rendimiento de la técnica propuesta para sistemas PV conectados a la red. Se desarrolla una técnica anti-islanding modificada de Sandia Voltage Shift (MSVS), que mejora los tiempos de detección de modo isla. Esto se debe a la modificación del producto exponencial realizada en la retroalimentación positiva para inyectar corriente, lo que hace que la respuesta sea más rápida que la SVS. Asimismo, este esquema propuesto ha sido validado con resultados experimentales. Se describe un sistema de reconexión, que tiene un bloque de pre-sincronización que mantiene la calidad de la energía generada por el DPGS durante el proceso de conmutación del modo isla al modo conectado a la red.

Palabras clave: control de corriente por Lyapunov, detección de componentes de secuencia, oscilador de ciclo límite (LCO), sincronización de red, sistema de reconexión, técnica activa de anti-islanding.

Abstract

This dissertation develops a new system capable to manage or even to reject electric disturbances from the grid network in order to set a reliable, effective and safe interconnection and synchronization between a Distributed Power Generation System (DPGS) and the electric grid. In this sense, a new synchronization technique of power converters based on a Limit Cycle Oscillator (LCO) and a Frequency-Locked Loop (FLL) is introduced, which makes the system frequency adaptive. The proposed technique LCO-FLL offers a high degree of immunity and robustness against swells, sags, harmonics and phase-frequency shift. Furthermore, the LCO-FLL has the advantage of performing the synchrony with the grid from any initial condition set for LCO, ensuring an acceptable transient onto the synchronization process. Other advantages of the proposed scheme are that it does not require a Phase Locked Loop (PLL), neither trigonometric functions and it gives useful information to estimate the positive and negative sequence components in a three-phase system with a highly polluted grid scenario. Also, a local stability analysis and a numerical analysis of the LCO-FLL is shown. The behavior and performance of the proposed technique are compared with synchronization techniques by means of experimental results. Furthermore, a three-phase application of the synchronization technique is evaluated experimentally. Moreover, the role and development of a current controller based on the LCO nonlinear theory with the combination of a Lyapunov control law is described, which provide stability for the proper operation of a Photovoltaic (PV) - grid-connected system during grid faults. It ensures an efficient current injection and active power regulation with a minor order differential equation for the control law in comparison with previous control techniques. The proposed control model offers a high degree of immunity and robustness against perturbation on the grid, thanks to the LCO-FLL synchronization technique. This LCO-FLL computes the positive and negative sequence components of the grid, which are used by a Lyapunov control law in order to control the injected currents to the grid, but also the inverter input voltage is considered in the controller design. This control configuration is proved for two different strategies, balanced injected currents and constant active power in presence of an unbalanced voltage grid. Simulation and experimental test results are given to demonstrate the proficiency and performance of the proposed technique in PV-Grid connected systems. Furthermore, a Modified Sandia Voltage Shift (MSVS) anti-islanding technique is developed, improving detection times for islanded faults. This is due to the exponential-product modification made in the positive feedback to inject current, making faster response than SVS. Moreover, this proposed scheme has been validated with experimental results. In addition, a re-connection system is depicted, which has a pre-synchronization block in order to maintain the energy quality generated by the DPGS during the switching process from islanded to grid-connected mode.

Keywords: active anti-islanding technique, grid synchronization, Limit Cycle Oscillator (LCO), Lyapunov current control, re-connection system, sequence-components detection.

1.

INTRODUCTION

Due to the increase and the expansion of different types of Distributed Power Generation Systems (DPGSs) connected to a centralized power grid, there is the need of more flexible and efficient controllers to manage the mixed distributed electrical network. Therefore, current controllers, synchronization techniques, as well as anti-islanding techniques, are fundamental in order to fulfill the requirements of power quality and to ensure stability in the frequency and grid voltage, even in a highly perturbed grid. In this sense, this chapter gives an overall description of different kinds of DPGSs connected to the grid, as well as the most common perturbations in the electric grid. After that, different types of faults in three-phase systems are summarized. Finally, the motivation, hypothesis, objectives, and document organization are exposed to contextualize the contribution of the present dissertation.

1.1 Distributed Power Generation Systems

Non-renewable energy sources as coal, oil or natural gas pollute the environment, which causes the rise in the average temperature of the planet due to the greenhouse effect. In other words, this kind of centralized power generation plants based on fossil fuels are not sustainable. That is the reason, the global energy agenda has been focused

on developing new and more diverse renewable energy sources, in order to reduce the CO2 levels on earth.

Some of the most important renewable energy sources installed in the world are Hydropower (pumped storage and mixed plants), Wind Energy, Solar Photovoltaic (PV) Energy, Concentrated Solar Power, Solid Biomass, Biogas, Liquid Biofuels, Geothermal, and Marine Energy (Tide, wave, and ocean energy). As it can be seen in Figure 1.1, the hydropower has the most installed capacity but it has a slow rate of growth due to the physical limitations of rivers and lake resources. On the contrary, Wind and Solar Energy have the highest growth rates with more than 17% and 27% respectively, in 2017 [1], [2].

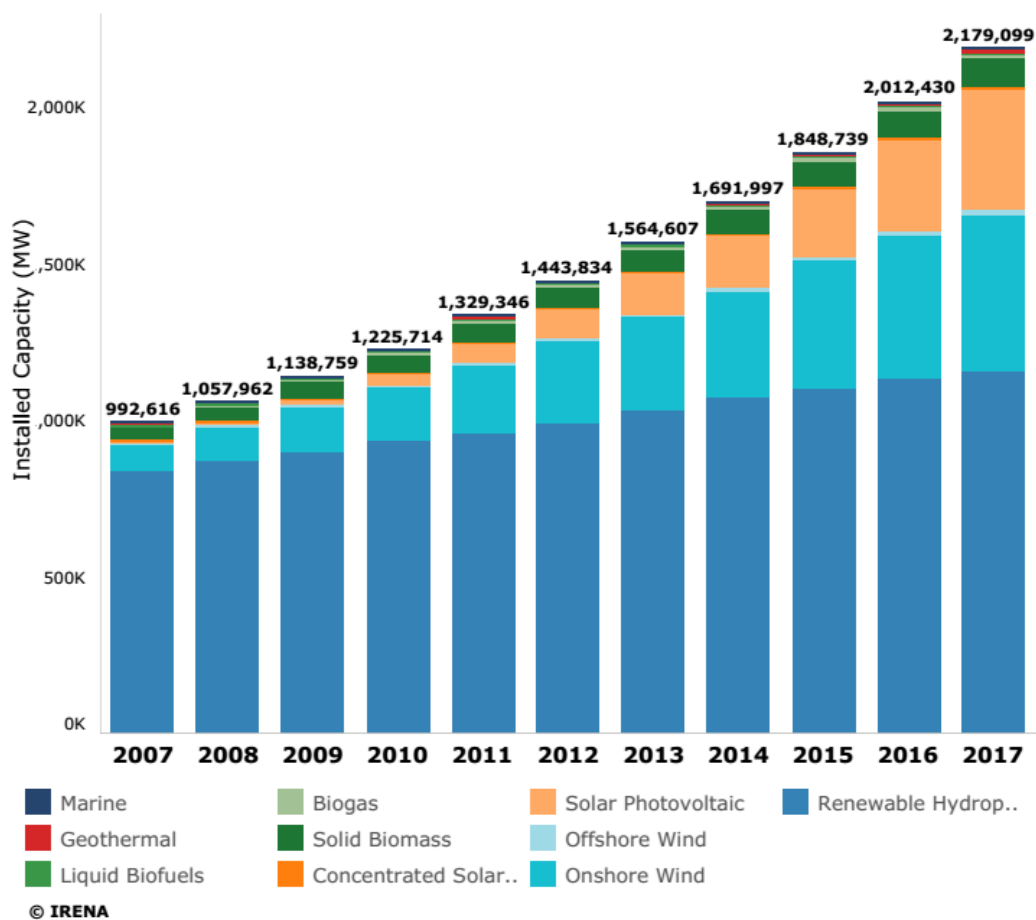


Figure 1.1. Total accumulative installed capacity of renewable energy from 2007-2017 (Cf. Figure 5 in [1]).

Under no islanding conditions, the renewable energy sources are interconnected to one or more centralized sources, making them DPGSs. Depending on the renewable

energy resource, every DPGS should have different topologies of power electronic converters with a controller, which is capable to operate in harsh environments and to withstand perturbations and abnormal interruptions in the grid network [3].

1.2 Faults Classification in Three-Phase Systems

Disturbances in Power Quality are distortions in voltage or current that present unexpected, uncertain, and unmodelled variations in magnitude or frequency regarding to nominal values during a time interval. Standards and recommendations as the IEEE1159 and EN50160 identify and classify each disturbance on grid networks into seven categories, depending on their magnitude, duration, and spectral content [4], [5]:

Transients. This category includes two transient types: impulsive and oscillatory; which are commented below:

An impulsive transient is a sudden, unipolar, frequency change in the steady-state condition of voltage, current, or both. This kind of transients is normally characterized by their rise and decay times. A typical voltage impulsive transient rises to its peak value of 2 kV in 1.2 ms and then decays to half its peak value in 50 ms. Commonly, lighting is the principal cause [6]. Figure 1.2 (Right side) shows a typical impulsive transient.

The second type of transients is oscillatory transients in voltage or current, which change their polarity rapidly. Oscillatory transients with a frequency greater than 500 kHz are considered high-frequency oscillatory transients. They are almost always due to some type of switching event, or due to a local system response to an impulsive transient. Power electronic devices produce oscillatory voltage transients as a result of commutation and RLC snubber circuits. Oscillatory transients can have repetition rates of several times per 60 Hz cycle and magnitudes of 0.1 pu.

Remarkable transients are the following. A transient with a frequency between 5-500 kHz is called a medium-frequency transient. They are due to Back-to-back capacitor energization, cable switching, or the response of a system to an impulsive transient. A transient with a frequency less than 5 kHz is a low-frequency transient. They are frequently encountered on sub-transmission and distribution systems. They are caused mostly by primarily capacitor bank energization. Figure 1.2 (Left side) shows a low-frequency oscillatory transient. Oscillatory transients with frequencies less than 300 Hz

can also be found on the distribution system and they are generally associated with ferro-resonance and transformer energization [5].

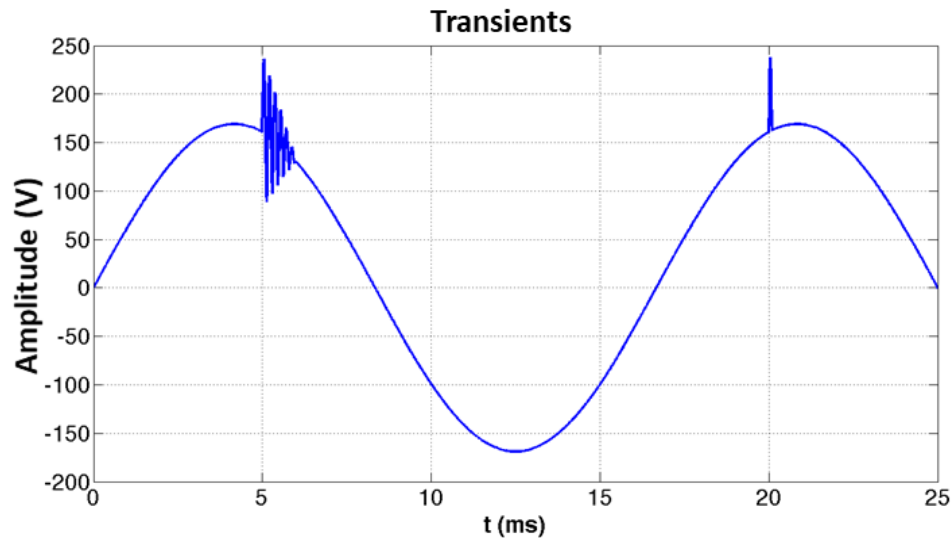


Figure 1.2. Oscillatory (left) and impulsive (right) transients.

Short-duration variations. Additional disturbances with regard to short-duration faults are variations caused by energization of large loads that require high starting currents, or intermittent loose connections in power wiring. Depending on the system conditions, and the fault location, they can cause either a complete loss of voltage (interruptions), temporary voltage drops (sags), or voltage rises (swells).

Complementary, an interruption occurs when the voltage supply or load current decreases to less than 0.1 pu for less than 1 minute, and they are the result of power system faults, equipment failures, and control malfunctions. Some interruptions may be preceded by a voltage sag when these interruptions are due to faults on the source system. The duration of the interruption will depend on the reclosing capability of the protective device. Instantaneous reclosing generally will limit the interruption caused by a non-permanent fault to less than 30 cycles. Figure 1.3 depicts an interruption voltage for 2 cycles approximately.

Voltage sags are usually associated with system faults but can also be caused by switching of heavy loads or starting of large motors. Typical fault clearing times range from 2 to 30 cycles, depending on the fault current magnitude and the type of overcurrent detection and interruption.

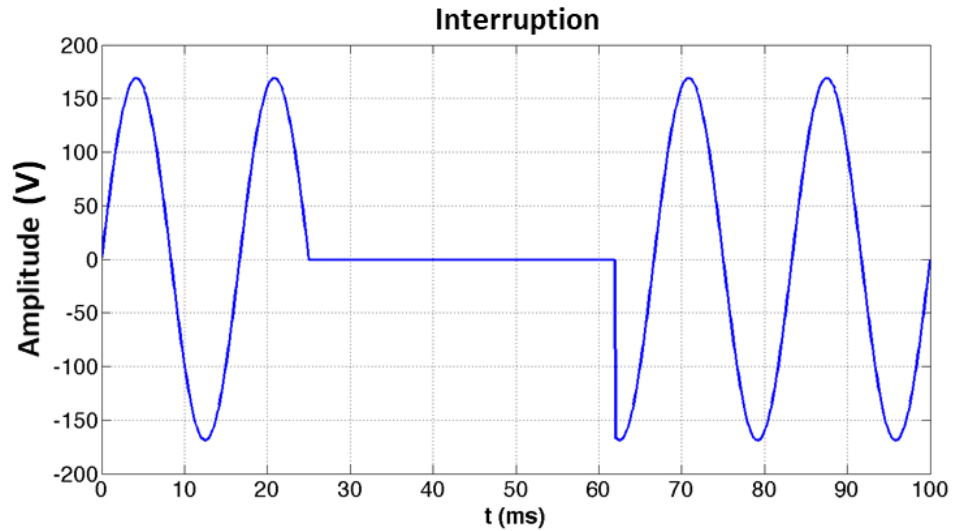


Figure 1.3. Interruption.

Voltage sags can also be caused by large load changes or motor starting. For example, an induction motor will draw six to ten times its full load current during starting. This lagging current causes a voltage drop in the impedance of the system. If the current magnitude is larger in comparison with the fault current, the resulting voltage sag can be significant [7]. In order to illustrate this, a voltage sag for 2.5 cycles is illustrated in Figure 1.4.

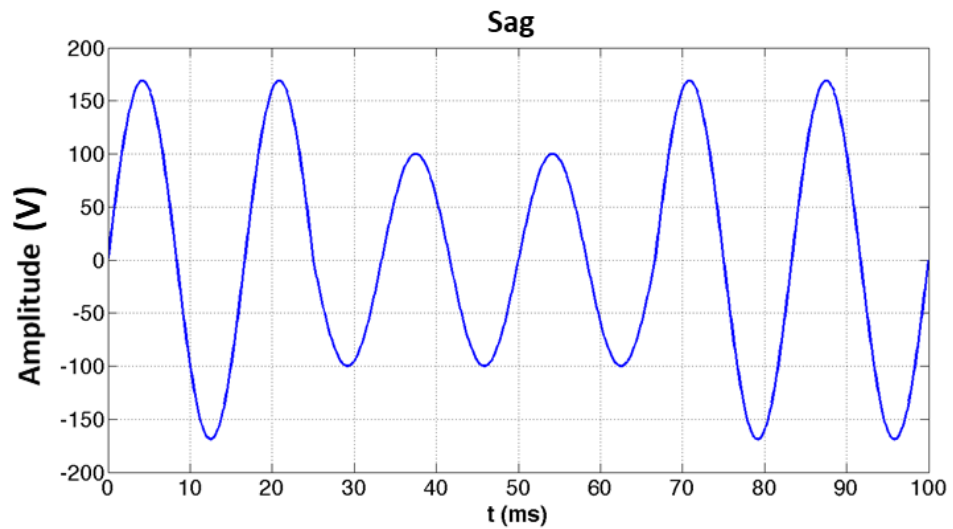


Figure 1.4. Sag.

A voltage swell is defined as a momentary increase in the voltage delivered by the grid, outside of the normal tolerances, with a duration of more than one cycle and less than a few seconds [6]. Typical magnitudes are between 1.1 and 1.8 pu. Voltage swells are usually associated with system fault conditions, but they are much less common than voltage sags. A voltage swell can occur due to a single line-to-ground fault on the system resulting in a temporary voltage rise on the unfaulted phases. Voltage swells can also be caused by switching off a large load or switching on a large capacitor bank. The severity of a voltage swell during a fault condition is a function of the fault location, system impedance, and grounding. On an ungrounded system, the line-to-ground voltages on the ungrounded phases will be 1.73 pu during a line-to-ground fault condition. Close to the substation on a grounded system, there will be no voltage rise on the unfaulted phases because the substation transformer is usually connected delta-wye, providing a low impedance zero sequence path for the fault current. Figure 1.5 depicts a swell voltage for 2.5 cycles.

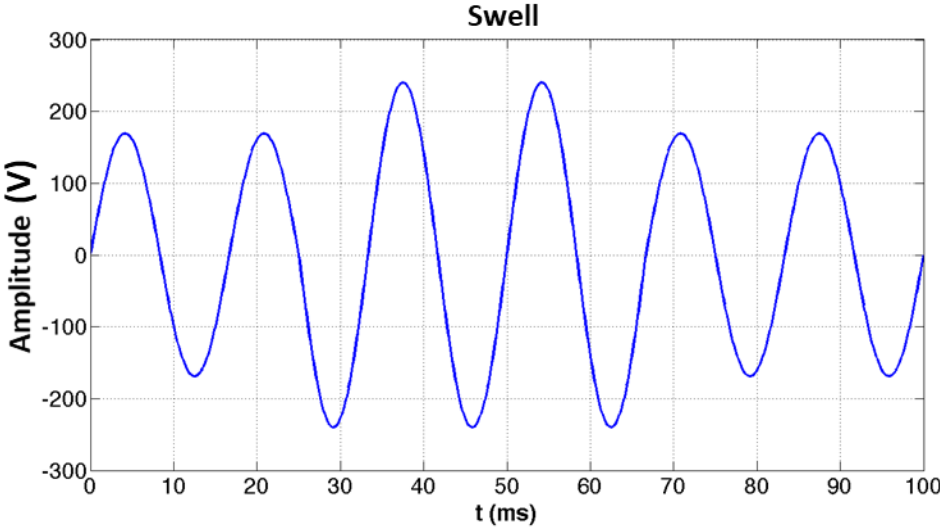


Figure 1.5. Swell.

Long duration variations. This kind of faults includes over, under-voltages, and current overloads longer than 1 minute. They are caused by load variations on the system and system switching operations.

Over-voltages can be the result of switching off a large load or variations in the reactive compensation on the system. Moreover, poor system voltage regulation capabilities or controls result in over-voltages. Incorrect tap settings on transformers can

also result in system over-voltages. Under-voltages are the result of a load switching on, or a capacitor bank switching off, or overloaded circuits. Moreover, the decrease to zero of the voltage supply for a period of time in excess of 1 minute is considered a sustained interruption. Voltage interruptions longer than 1 minute are often permanent in nature, and require manual intervention for restoration [5].

Imbalance. Voltage imbalance is defined as the ratio of the negative or zero sequence component, and the positive sequence component. Voltage imbalances are resulting from unbalanced loads causing negative or zero sequence currents. Imbalance can be estimated as the maximum deviation from the average of the three-phase voltages or currents, divided by the average of the three-phase voltages or currents, expressed in percent, this is [8]:

$$\text{Voltage imbalance} = 100 \times \frac{\text{max deviation from average voltage}}{\text{average voltage}}. \quad (1.1)$$

For example, with phase-to-phase voltages of 230, 232, and 225, the average is 229. The maximum deviation from the average among them is 4. The percent imbalance is $100 \times (4/229) = 1.7\%$.

The main cause of voltage imbalance (less than 2%) is unbalanced single phase loads on a three-phase circuit. Voltage imbalance can also be the result of capacitor bank anomalies, such as a blown fuse on one phase of a three-phase bank. Severe voltage imbalance (greater than 5%) can result from single-phasing conditions.

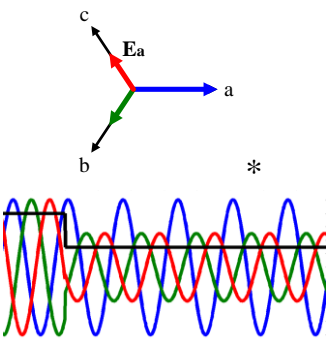
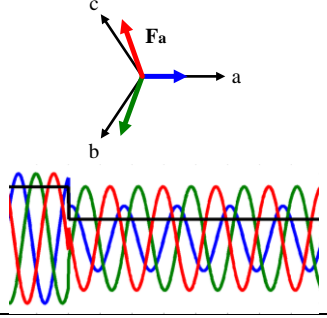
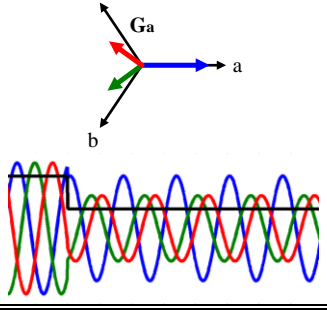
Nonsymmetrical faults lead to drops in one, two, or three phases, with not all phases having the same drop. A classification into four types is proposed in [9], and extended to seven types in [10] and [11]. Table I.I and Table I.II depict the seven different types of faults in three-phase voltage systems. It is important to highlight that fault types B and E are shown in systems where the grid zero-sequence voltage has influence, for instance, in no isolated wye connected systems.

TABLE I.I
CLASSIFICATION OF THE THREE-PHASE VOLTAGE FAULTS (A-D)

Type fault	Phasor expression	Fault condition
	<p>Type A</p> $\bar{V}_a = \frac{1}{2}V$ $\bar{V}_b = -\frac{1}{4}V - \frac{1}{4}jV\sqrt{3}$ $\bar{V}_c = -\frac{1}{4}V + \frac{1}{4}jV\sqrt{3}$	<ul style="list-style-type: none"> • Three-phase to ground fault. • Three-phase fault.
	<p>Type B</p> $\bar{V}_a = \frac{1}{2}V$ $\bar{V}_b = -\frac{1}{2}V - \frac{1}{2}jV\sqrt{3}$ $\bar{V}_c = -\frac{1}{2}V + \frac{1}{2}jV\sqrt{3}$	<ul style="list-style-type: none"> • Single-phase fault.
	<p>Type C</p> $\bar{V}_a = V$ $\bar{V}_b = -\frac{1}{2}V - \frac{1}{2}jV$ $\bar{V}_c = -\frac{1}{2}V + \frac{1}{2}jV$	<ul style="list-style-type: none"> • Single-phase to ground fault. • Phase to phase fault.
	<p>Type D</p> $\bar{V}_a = \frac{1}{2}V$ $\bar{V}_b = -\frac{1}{3}V - \frac{1}{3}jV\sqrt{8}$ $\bar{V}_c = -\frac{1}{3}V + \frac{1}{3}jV\sqrt{8}$	<ul style="list-style-type: none"> • Single-phase to ground fault. • Phase to phase fault after DY transformer.

* This fault is shown in systems where the grid zero-sequence voltage has influence, this is, in no isolated wye or delta connected systems [12], [13].

TABLE I.II
CLASSIFICATION OF THE THREE-PHASE VOLTAGE FAULTS (E-G)

Type fault	Phasor expression	Fault condition
	<p>Type E</p> $\bar{V}_a = V$ $\bar{V}_b = -\frac{1}{4}V - \frac{1}{4}jV\sqrt{3}$ $\bar{V}_c = -\frac{1}{4}V + \frac{1}{4}jV\sqrt{3}$	<ul style="list-style-type: none"> • Two-phase to ground fault.
	<p>Type F</p> $\bar{V}_a = \frac{1}{2}V$ $\bar{V}_b = -\frac{2}{9}V - \frac{2}{9}jV\sqrt{8}$ $\bar{V}_c = -\frac{2}{9}V + \frac{2}{9}jV\sqrt{8}$	<ul style="list-style-type: none"> • Three-phase fault. • Three-phase to ground fault. • Two-phase to ground fault.
	<p>Type G</p> $\bar{V}_a = \frac{2}{3}V$ $\bar{V}_b = -\frac{1}{2}V - \frac{1}{2}jV$ $\bar{V}_c = -\frac{1}{2}V + \frac{1}{2}jV$	<ul style="list-style-type: none"> • Three-phase fault. • Three-phase to ground fault. • Two-phase to ground fault.

* This fault is shown in systems where the grid zero-sequence voltage has influence, this is, in no isolated wye or delta connected systems [12], [13].

Waveform distortion. It is defined as the steady-state deviation from an ideal sine wave characterized by the spectral content of the deviation. There are five primary types of waveform distortion: DC offset, Harmonics, Inter-harmonics, Notching, and Noise.

The DC offset is a phenomenon that could occur as a consequence of half-wave rectification or due to the effect of a geomagnetic disturbance. The direct current in alternating current networks can be detrimental due to an increase in additional stressing of insulation, and transformer saturation. Figure 1.6 shows a DC offset in AC voltage.

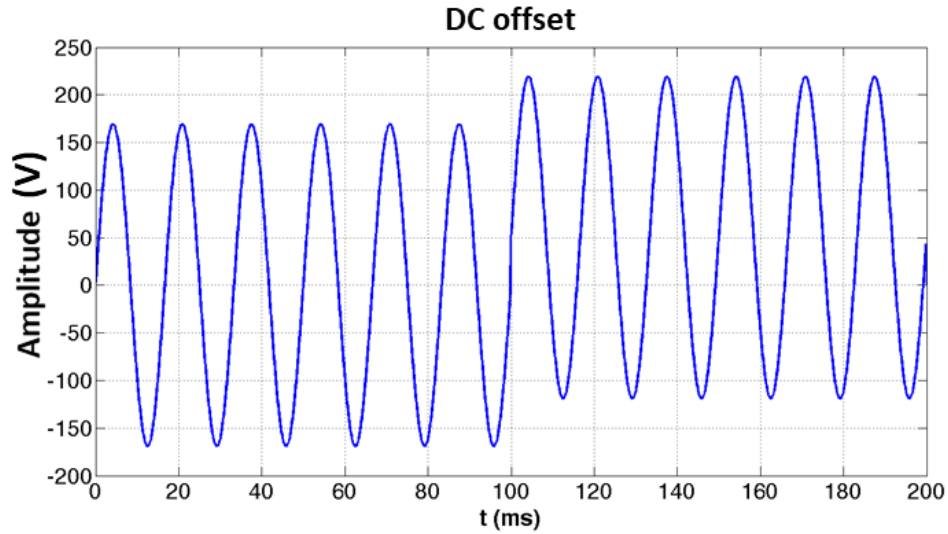


Figure 1.6. DC offset.

Harmonics are sinusoidal voltages or currents having frequencies that are integer multiples of the fundamental frequency at which the system supply is designed to operate (Normally 50 Hz or 60 Hz). These harmonics mixed with the fundamental voltage or current producing waveform distortion. Harmonic distortion is produced due to the nonlinear characteristics of devices and loads on the power system. These devices can usually be modeled as current sources that inject harmonic currents into the power system. These currents cause nonlinear voltage drops across the system impedance causing voltage distortion.

Harmonic distortion levels can be characterized by the complete harmonic spectrum with magnitudes and phase angles of each individual harmonic component. It is also common to use a single quantity, the Total Harmonic Distortion (THD), as a measure of the magnitude of harmonic distortion. Figure 1.7 illustrates the fundamental waveform and the 3rd, 5th, 7th and 9th harmonic, moreover, the total sum of all of them. Mathematically, the THD is defined as the ratio of the Root Mean Square (RMS) amplitude of a set of higher harmonic frequencies, and the RMS amplitude of the fundamental frequency [14]:

$$THD_F = \frac{\sqrt{\sum_{n=2}^{\infty} V_n^2}}{V_1}. \quad (1.2)$$

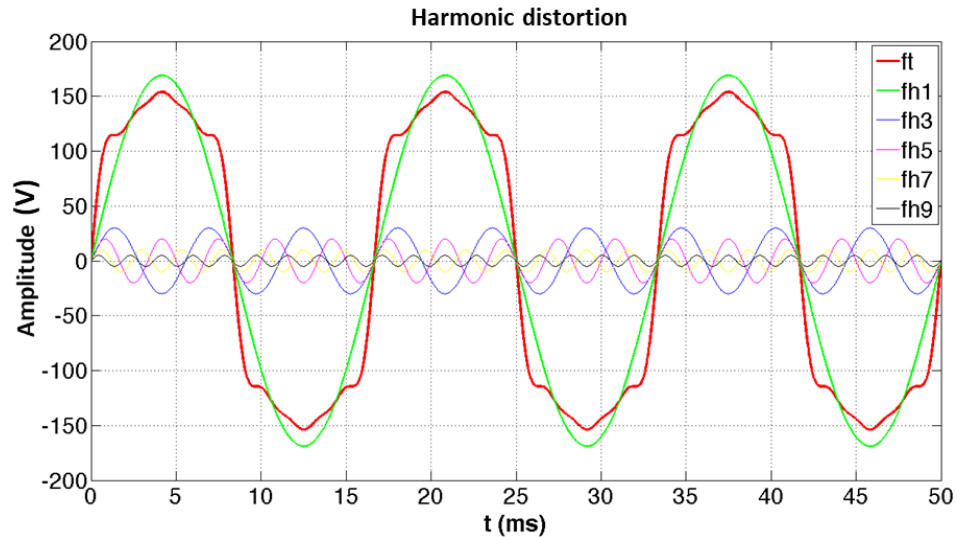


Figure 1.7. Harmonic distortion.

Interharmonics can be found in networks of all voltage classes. They can appear as discrete frequencies or as a wide-band spectrum. The main sources of interharmonic waveform distortion are static frequency converters, cyclo-converters, induction motors, and arcing devices.

The effects of interharmonics are not well known but it has been shown to affect power line carrier signal and to induce visual flicker in display devices such as Cathode Ray Tube (CRTs).

Notching is a periodic voltage disturbance caused by the normal operation of power electronics devices when the current is commutated from one phase to another. During this period, there is a momentary short circuit between two phases. The severity of the notch at any point in the system is determined by the inductance source and the isolating inductance between the converter and the point being monitored [15].

Voltage notching represents a special case that falls between transients and harmonic distortion. Since notching occurs continuously (steady state), it can be characterized through the harmonic spectrum of the affected voltage. However, the frequency components associated with notching can be quite high and may not be readily characterized by measurement equipment normally used for harmonic analysis. Three-phase converters that produce continuous dc current are the most important cause of voltage notching.

Noise is unwanted electrical signals with broadband spectral content lower than 200 kHz superimposed upon the power system voltage or current in phase conductors or

found on neutral conductors or signal lines. Noise in power systems can be caused by power electronic devices, control circuits, arcing equipment, loads with solid-state rectifiers, and switching power supplies. Noise problems are often exacerbated by improper grounding. Basically, noise consists of any unwanted distortion of the power signal that cannot be classified as harmonic distortion or transients.

The frequency range and magnitude level of noise depend on the source, which produces the noise and the specific characteristics. A typical magnitude of noise is less than 1% of the voltage magnitude. Noise disturbs electronic devices such as microcomputers and programmable controllers. The problem can be mitigated by using filters, isolation transformers, and some line conditioners. A characteristic noise in grid signals can be seen in Figure 1.8.

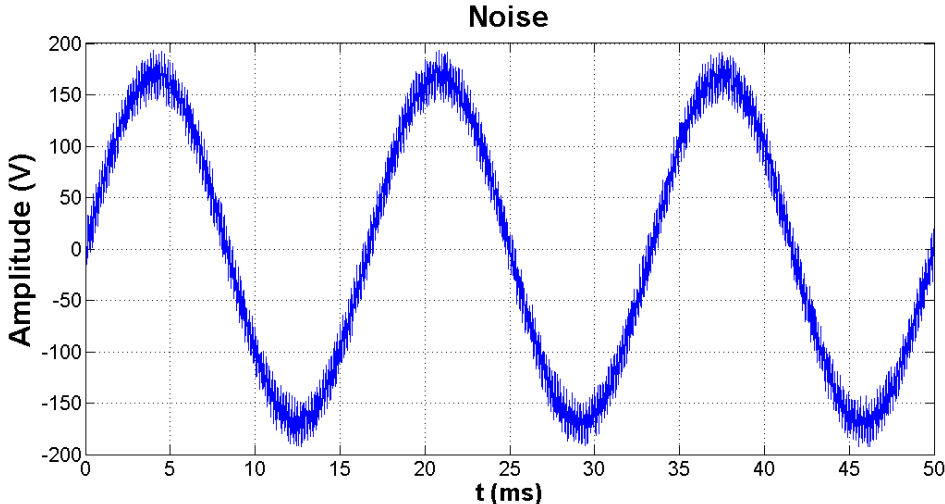


Figure 1.8. Electric noise in a voltage phase.

Voltage fluctuations and power frequency variations. They are systematic variations of the voltage waveform, or a series of random voltage changes. This voltage fluctuations do not exceed the voltage ranges of 0.95–1.05 pu. Any load that has significant current variations, especially in the reactive component, can cause voltage fluctuations. Arc furnaces are the most common cause of voltage fluctuations in the transmission and distribution system.

Voltage fluctuations are defined by their RMS magnitude expressed as a percent of the fundamental. An example of this type of voltage disturbance is shown in Figure 1.9. Voltage fluctuations generally appear as a modulation of the fundamental frequency

(similar to amplitude modulation of an am radio signal). Therefore, it is easy to define a magnitude for the voltage fluctuation as the RMS magnitude of the modulation signal. This can be obtained by demodulating the waveform to remove the fundamental frequency and then measuring the magnitude of the modulation components. Typically, magnitudes as low as 0.5% can result in perceptible light flicker if the frequencies are in the range of 6–8 Hz [5].

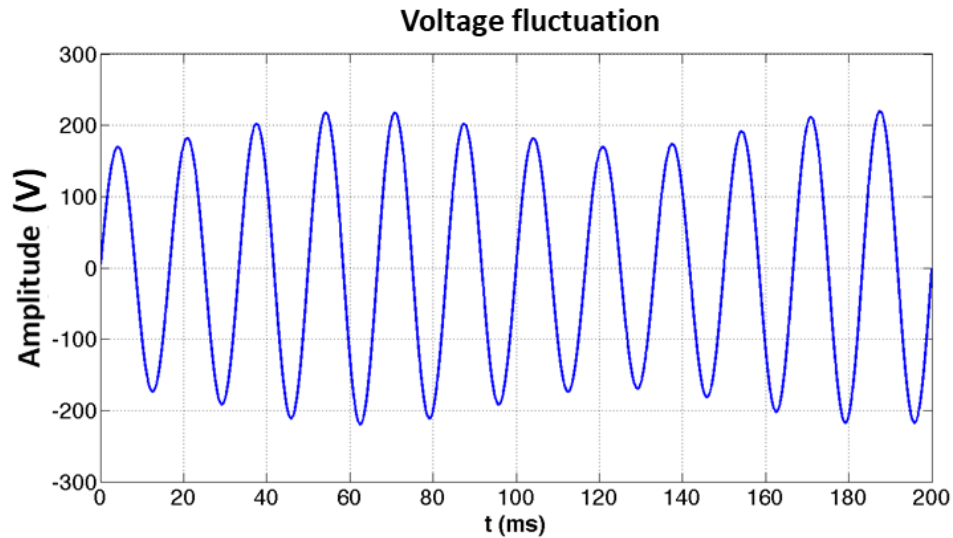


Figure 1.9. Voltage fluctuation in a voltage phase.

Frequency perturbations are directly related to the rotational speed of the generators on power systems. At any instant, the frequency depends on the balance between the load and the capacity of the available generation. When this dynamic balance changes, small changes in frequency occur. The size of the frequency shift and its duration depends on the load characteristics and the response of the generation system to load changes.

Frequency variations that are outside of accepted limits for normal steady-state operation of power systems are normally caused by faults on the bulk power transmission system, a large block of the load being disconnected, or a large source of generation going off-line. Frequency variations that affect the operation of rotating machinery, or processes that derive their timing from the power frequency (clocks), are rare on modern interconnected power systems. Figure 1.10 depicts a frequency variation in a voltage phase [4], [5].

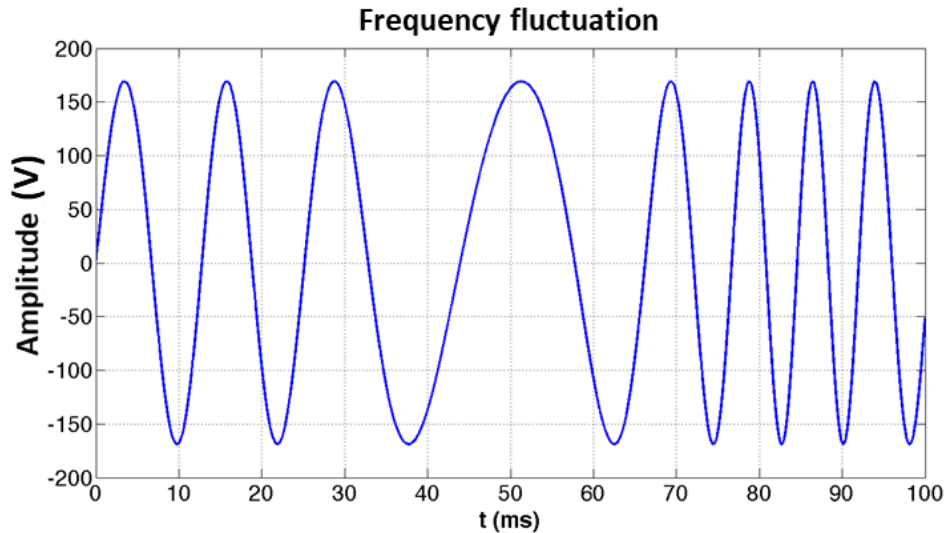


Figure 1.10. Frequency fluctuation in a voltage phase.

1.3 Motivation, Hypothesis, and Objectives

Motivation. The previously described perturbations incentive to develop synchronization systems in order to manage or in some cases diminish or disappear this kind of problems in the electric grid. Therefore, the next hypothesis is developed.

Hypothesis. It is possible to diminish electric grid disturbances by means of synchronization of Distributed Power Generation Systems (DPGS), in specific a Photovoltaic (PV) system, using Lyapunov control in combination with Limit Cycle Oscillators (LCOs).

General Objective: Synchronize a DPGS with the electric grid by means of current injection, utilizing Lyapunov control and LCOs.

Specific Objectives:

- Maintain the synchronization between the DPGS and the electric grid in spite of harmonic distortion effects induced by nonlinear loads.
- Contribute a new robust control scheme to handle nonlinear loads applied to the synchronization of a PV system with the electric grid, which apply current injection methods, Lyapunov control and LCOs.

1.4 Structure of the manuscript

The next Chapters and Sections are structured as follows: An introduction of the different types of synchronization systems for the electric grid is introduced in Chapter 2; this allows us to show the global context of different relevant approaches for synchronizing system with the grid. Chapter 3 includes the main contribution, which is the nonlinear synchronization system named as Limit Cycle Oscillator – Frequency Locked Loop (LCO-FLL). This Chapter is fully developed and published in IEEE Transactions on Industrial Electronics (TIE) in [16], also it is patented in Mexico with MX/a/2017/006644 and it has the US patent request with the reference number: 15/975,175. After that, a current control based on Lyapunov theory and the LCO is described in Chapter 4. This current control was submitted to TIE and it was in process of revision during the making of this dissertation. Afterward, in Chapter 5, an improvement in the Sandia Voltage Shift (SVS) anti-islanding technique is exposed. Moreover, a re-connection process of a DPGS to the grid network with a critical load is described in Chapter 6. Finally, the conclusion and final remarks are summarized in Chapter 7.

2.

SYNCHRONIZATION SYSTEMS FOR THE ELECTRIC GRID

Most of the grid-connected power converters, such as active power filters, Distributed Power Generation Systems (DPGSs), static VAR compensators, and Uninterruptible Power Supplies (UPSs), need a phase or frequency tracking system in order to synchronize with the grid voltage. In certain applications (e.g. DPGSs,) it is critical to have a synchronization system with a high degree of immunity to harmonics, unbalances, and power systems disturbances as sags and swells in the utility grid [17]. There are several state-of-the-art techniques in detecting the phase angle of the grid voltages. Some of the most important synchronization techniques are described below in order to introduce a new nonlinear technique in the next chapter.

2.1 Zero Crossing Detector (ZCD)

A simple and easy technique that is used to detect the phase angle is the zero-crossing voltage detector. Zero crossing detection is the most common method for measuring the frequency or the period of a periodic signal. When measuring the frequency of a signal, usually the number of cycles of a reference signal is measured over one or more time periods of the signal being measured. Measuring multiple periods helps to reduce errors caused by phase noise by making the perturbations in zero crossings

small relative to the total period of the measurement. The result is an accurate measurement at the expense of slow measurement rates [18]. However, voltage sags and harmonics can disturb greatly the output signal. As it can be seen in Figure 2.1, false zero crossing are detected due to harmonic disturbances.

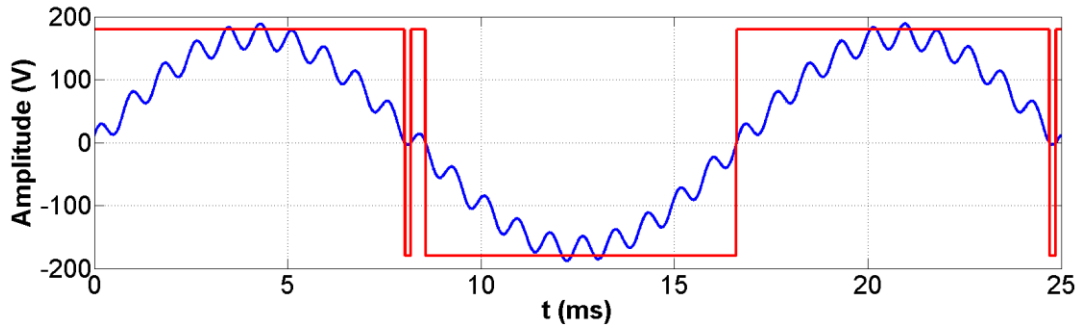


Figure 2.1. False zero crossing detection due to harmonic disturbances.

Digital schemes have improved zero-crossing methods by using filtering techniques: extended Kalman filters, low-pass filters, space-vector, and recursive weighted least-square estimation, for example [17], [19]. Despite these improvements, unexpected disturbances can slide the phase-angle signal [17], [20]; along with a significant delay in the processed signal [17].

2.2 Phase Locked Loop (PLL)

The earliest description of PLL is in [21] in 1923 and in [22] in 1932, where it can be explained as a device which causes one signal to track another one. It keeps an output signal synchronizing with a reference input signal in frequency as well as in phase. More precisely, the PLL is simply a servo system, which controls the phase of its output signal in such a way that the phase error between the output phase and reference phase reduces to a minimum. A functional block diagram of a PLL is shown in Figure 2.2, which consists of a phase detector (PD), a loop filter (LF), and a voltage-controlled oscillator (VCO).

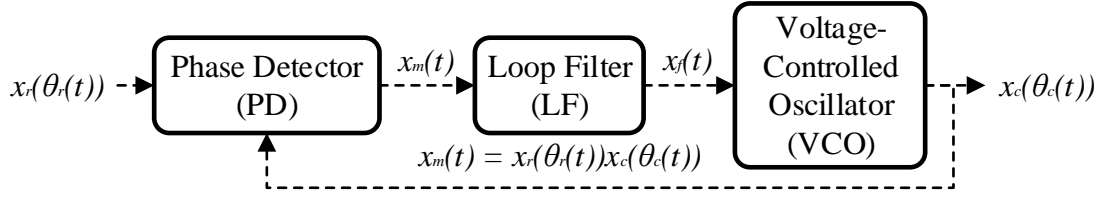


Figure 2.2. PLL Block diagram.

From Figure 2.2, let x_r and x_c be:

$$x_r(t) = A \cos(\omega_r t + \theta_r), \quad (2.1)$$

$$x_c(t) = B \cos(\omega_c t + \varphi_c), \quad (2.2)$$

where ω_r and ω_c are the angular frequencies of the input signal and the VCO, respectively. Moreover, θ_r and φ_c are their phase constants. If the loop is initially unlocked and the PD (Signal multiplier) has sinusoidal characteristics, then x_m at the PD is given by:

$$x_m(t) = K_d \{ \cos[(\omega_r - \omega_c)t + \theta_r - \varphi_c] + \cos[(\omega_r + \omega_c)t + \theta_r + \varphi_c] \}, \quad (2.3)$$

where K_d is the gain of the PD, and the higher frequency is eliminated by LF (Low-pass filter). Therefore, the output of the LF is:

$$x_f(t) = K_d \{ \cos[(\omega_r - \omega_c)t + \theta_r - \varphi_c] \}. \quad (2.4)$$

After a period of time sufficiently long, the VCO output signal x_c becomes synchronous with the input signal x_r . Then, the signal x_c can be expressed as:

$$x_c(t) = B \sin(\omega_r t + \varphi_c). \quad (2.5)$$

It can be seen from (2.2) and (2.5) that φ_c is a linear function given by:

$$\varphi_c = (\omega_r - \omega_c)t + \varphi_c \quad (2.6)$$

and then, the LF output signal x_f in (2.4) becomes a dc signal:

$$x_f(t) = K_d\{\cos[\theta_r - \phi_c]\}. \quad (2.7)$$

Therefore, the VCO is a frequency-modulated oscillator, where the instantaneous angular frequency ω_{inst} is a linear function of the controlled signal x_f , around the central angular frequency ω_r , this is:

$$\omega_{inst} = \frac{d}{dt}(\omega_c t + \phi_c) = \omega_c + K_v x_f(t), \quad (2.8)$$

where K_v is the VCO sensitivity. From (2.6), (2.7), and (2.8), yields:

$$\phi_c = \theta_r - \cos^{-1}\left(\frac{\omega_r - \omega_c}{K_d K_v}\right). \quad (2.9)$$

Note that if the angular frequency difference $\omega_r - \omega_c$ is much lower than the product $K_d K_v$, then $\theta_r - \phi_c \approx \cos^{-1}(0) = \pi/2$, indicating that the VCO signal is in phase quadrature with the input signal when the loop is in lock. This is, the phase quadrature corresponds to $\omega_r = \omega_c$. Thus, it is convenient to let $\theta_c = \phi_c + \pi/2$.

When the difference $|\omega_r - \omega_c|$ exceeds the loop gain $K_d K_v$ in a sinusoidal-characteristic PD, a proper θ_c is not suitable as it can be seen in (2.9). Under this condition, synchronization can no longer maintain and the loop falls out of lock [23]. That is why traditional PLL-based algorithms fail to handle the unbalanced situation [24], [25]. They show an unwanted large frequency swing during the phase angle fluctuations in grid fault conditions [26].

2.3 Enhanced Phase Locked Loop (EPLL)

The main point of the structure of the EPLL is the introduction of a novel phase detection scheme which is shown in more detail in Figure 2.3. Rather than multiplying the input signal by the output of VCO to generate a signal where the phase is expected to be the phase difference of these two signals, a refined variant of the VCO signal is subtracted from the input signal to produce an intermediary signal. This intermediary signal is then multiplied by the output of the VCO the same way as the input signal is multiplied by the output of VCO in conventional PLLs.

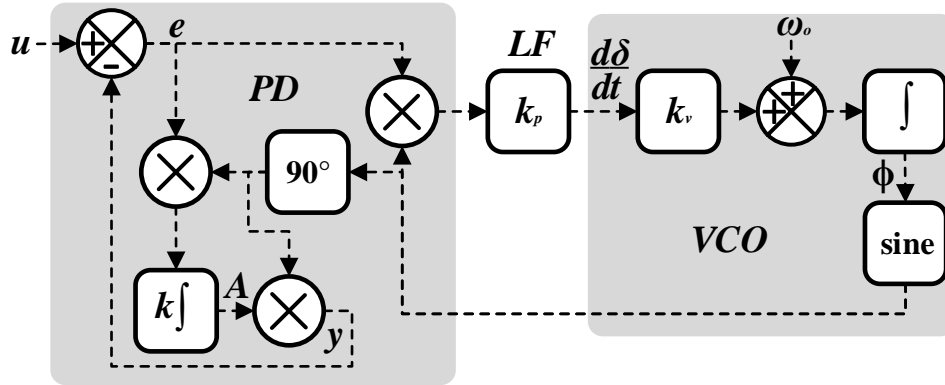


Figure 2.3. EPLL Block diagram [27].

As it can be seen in Figure 2.3 in the PD block, one multiplication, required by conventional PLLs, is replaced by a phase-shift of 90 degrees, three multiplications, one subtraction, and one integration. This makes that the output is locked both in phase and in amplitude. In contrast to a conventional PLL which provides only an output signal coherent with the input signal [27]. Nevertheless, EPLL has small oscillations in the synchronization signals under non-nominal frequency [28], which could make the system unstable.

2.4 Quadrature Phase Locked Loop (QPLL)

The QPLL structure is based on estimating in-phase and quadrature-phase amplitude of the fundamental component of the input signal [29], [30]. The QPLL provides an estimation of the frequency, instead amplitude and phase angle, which are not directly estimated. A block diagram of the QPLL is shown in Figure 2.4. where it can be seen that the phase detector (PD) in the conventional PLL is replaced with an alternative mechanism of multiplier block.

The QPLL considers a sum of two in-phase and quadrature-phase components for its output as:

$$y(t) = K_s(t) \sin(\theta(t)) + K_c(t) \cos(\theta(t)). \quad (2.10)$$

This signal is necessary to estimate the input fundamental component. The in-phase and quadrature-phase outputs of the VCO are multiplied by $K_s(t)$ and $K_c(t)$ (outputs of the integration units), and the results are added to generate the desired component $y(t)$. This component is subtracted from the input signal $v(t)$ to generate an error signal. This error is used to estimate the in-phase, the quadrature amplitudes ($K_s(t)$ and $K_c(t)$), and phase $\theta(t)$.

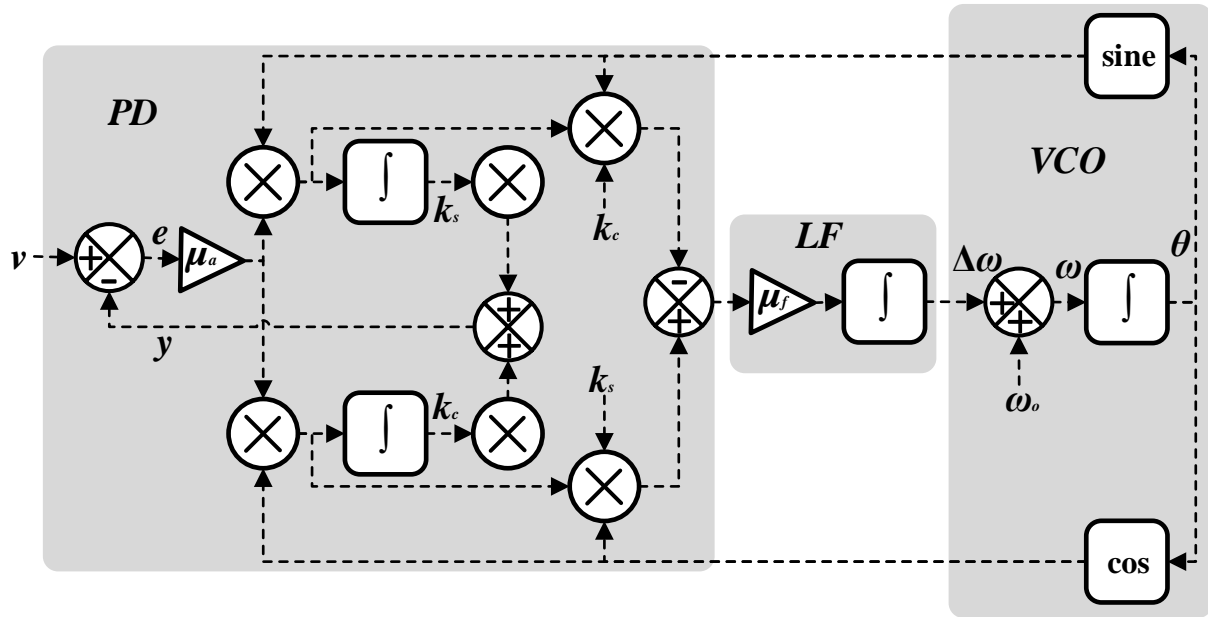


Figure 2.4. QPLL Block diagram [29].

The QPLL calculates the derivatives of these variables and then, it integrates them to yield the results. Thus, the frequency of the input signal is also estimated by the QPLL and it is equal to the derivative of the phase angle. The behavior of the QPLL is controlled by two internal parameters: μ_a controls the speed of convergence of the amplitude of the response, while μ_f controls the frequency. A larger value of each parameter provides a faster convergence of the corresponding variables. However, faster convergence is accompanied by a larger steady-state error, which is due to the presence of noise and distortions in the input signal of the estimator [31]. One important drawback is that QPLL consumes a considerable quantity of computation resources due to its multipliers [28].

2.5 Second Order Generalized Integrator-Phase Locked Loop (SOGI-PLL)

The concept of the Generalized Integrator (GI) for sinusoidal signals was formally introduced in [32]. This integrator stems from the principle that the time-domain convolution product of a sinusoidal function by itself gives rise to the original function multiplied by the time variable. Therefore, a processing block where the transfer function matches with the Laplace transform of a sinusoidal function (resonator), will act as an amplitude integrator for a sinusoidal signal applied to its input. Moreover, the quadrature combination of the sine and cosine transfer functions gives rise to an ideal integrator independent of the phase angle of the sinusoidal input signal. An adaptive filter structure, based on the GI structure, named Second Order Generalized Integrator (SOGI) was introduced in [33] and [34]. The structure of this resonant filter is shown in Figure 2.5, where it can be noticed how the resonance frequency of the SOGI is an external parameter called ω' .

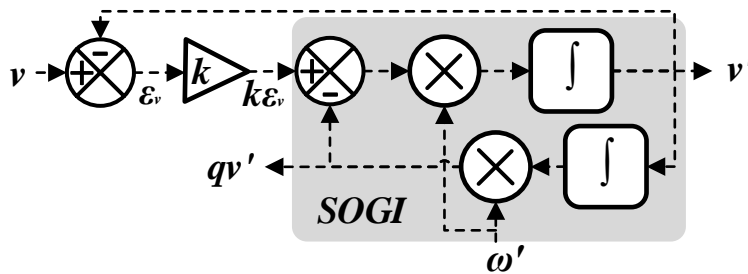


Figure 2.5. SOGI Block diagram [33].

The transfer function of the SOGI is given by:

$$SOGI(s) = \frac{v'}{k\varepsilon_v}(s) = \frac{\omega' s}{s^2 + \omega'^2}, \quad (2.11)$$

where the resonance frequency was called ω' to difference it from the input frequency ω . The two in-quadrature output signals of the adaptive filter in Figure 2.5, i.e., v' and qv' , are defined by the following transfer functions:

$$D(s) = \frac{v'}{v}(s) = \frac{k\omega' s}{s^2 + k\omega' s + \omega'^2}, \quad (2.12)$$

$$Q(s) = \frac{qv'}{v}(s) = \frac{k\omega'^2}{s^2 + k\omega' s + \omega'^2}. \quad (2.13)$$

As it can be concluded from (2.12), the bandwidth of the bandpass filter is exclusively set by the gain k and it is independent of the center frequency ω' . The same happens with the low-pass filter of (2.13), where the static gain only depends on k [35].

In order to control the angular frequency of the SOGI from Figure 2.5, a PLL is used to lock in phase with the sinusoidal input signal, as it can be seen in Figure 2.6. However, this configuration has trigonometric functions and a VCO which has a high cost in a digital implementation [36].

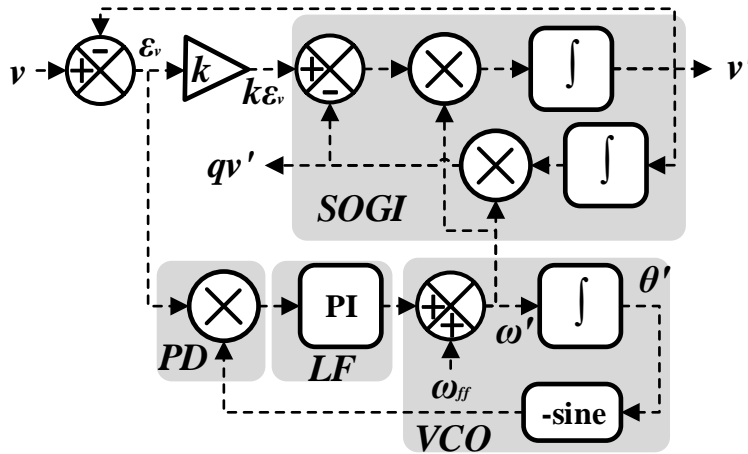


Figure 2.6. SOGI-PLL Block diagram [36].

2.6 Second Order Generalized Integrator-Frequency Locked Loop (SOGI-FLL)

The FLL was introduced in [37] as an effective mechanism for adapting the center frequency of the SOGI. The adaptive filter, including the FLL, is shown in Figure 2.7 where the frequency error variable ε_f can be defined as the product of qv' by ε_v , and an integral controller with a negative gain $-\gamma$ can be used to make zero the dc component of the frequency error by shifting the SOGI resonance frequency ω' until matching the input

frequency ω . The SOGI-FLL shown in Figure 2.7 is a single-phase synchronization system in which the input frequency is directly detected by the FLL.

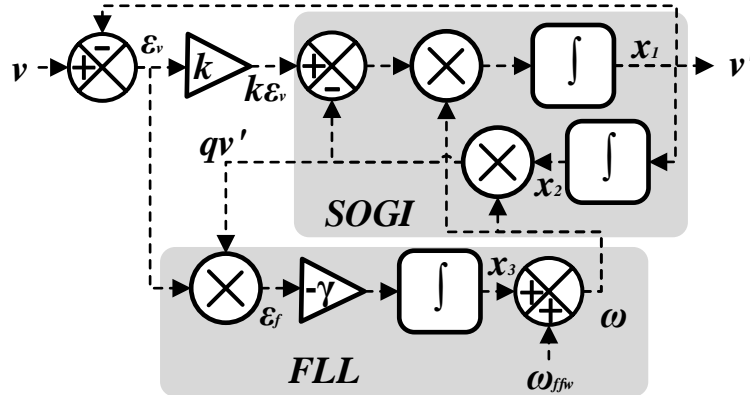


Figure 2.7. SOGI-FLL Block diagram [37].

2.7 Adaptive Notch Filter (ANF)

The dynamic behavior of this modified lattice-based discrete-time ANF is characterized by the following set of differential equations:

$$\ddot{x} + \theta^2 x = 2\zeta\theta e(t), \quad (2.14)$$

$$\dot{\theta} = -\gamma x \theta e(t), \quad (2.15)$$

$$e(t) = u(t) - \dot{x}, \quad (2.16)$$

where θ is the estimated frequency, $u(t)$ is the input signal, ζ and γ are adjustable real positive parameters that determine the estimation accuracy and the convergence speed of the ANF. A block diagram of this ANF can be seen in Figure 2.8.

This technique is simple and it offers a high degree of immunity and insensitivity to power system disturbances, harmonics and other types of pollution that exist in the grid signal. Moreover, it does not require a phase-locked loop for the synchronization. This ANF synchronization system is very similar to the SOGI-FLL and they have also similar performance depending on the tuning parameters [38]. These two techniques, SOGI-FLL and ANF estimate important grid parameters for single and three-phase systems, reducing undesirable frequency swings during phase angle jumps [35], [39]. However,

they are affected by swells and sags perturbations due to the trajectories of their harmonic oscillators, which are dependent on the initial conditions of its integrators. This characteristic is undesirable in certain applications that need a constant amplitude on the synchronized signals despite swells and sags in the normal operation showed in IEEE 1547 Standard [40], that is within $(88\% \leq V \leq 110\%)$.

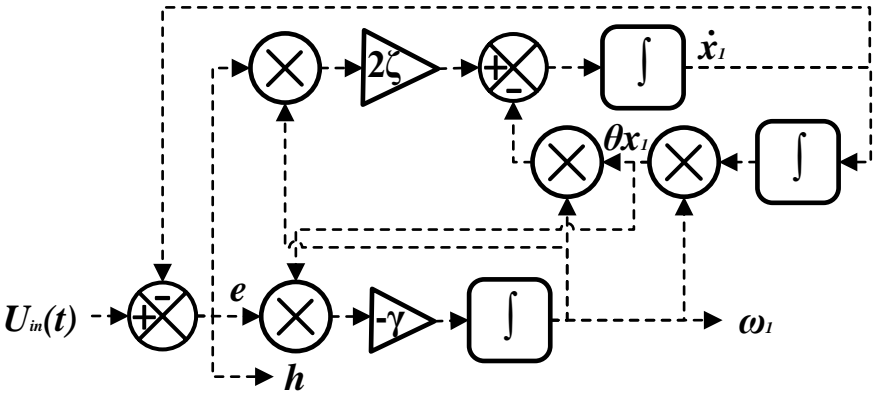


Figure 2.8. ANF Block diagram [38].

3.

LIMIT CYCLE OSCILLATOR – FREQUENCY LOCKED LOOP (LCO-FLL)

The main contribution of this doctoral research is focused on a novel grid synchronization scheme based on a nonlinear Limit Cycle Oscillator (LCO), which is able to produce synchronized signals with constant amplitude despite variations within the normal operation that has been marked in IEEE 1547 Standard [40]. The grid synchronization scheme ensures a well-behaved transient in the synchronization process, within an ample range of initial conditions. Moreover, this system rejects harmonics and handles a phase-frequency shift in a highly polluted grid. Such features, especially its amplitude robustness, gives an original characteristic to this technique, making it a good alternative to grid-synchronization systems where a stable current injection under disturbed grid circumstances is required [41]–[43].

The proposal scheme has been named as the Limit Cycle Oscillator-Frequency Locked Loop (LCO-FLL) since it is based on the limit cycles theory [44] and the frequency adaptive system FLL [37]. Some issues of the resulting scheme LCO-FLL has been reported in [16].

The following sections of this Chapter are organized as follows. A mathematical analysis of the LCO structure is given in section 3.1. Section 3.2 shows the interconnection process of LCO and FLL. Local stability analysis and synchronization stability numerical analysis of LCO-FLL is shown in section 3.3 and 3.4, respectively. Section 3.5 exposes a

three-phase LCO-FLL structure to detect sequence components. Experimental comparison results with nonlinear systems (SOGI-FLL, ANF, and PLL based algorithms) and three-phase LCO-FLL evaluation are depicted in section 3.6. Moreover, a harmonic detection system for critical loads and simulation tests are depicted in section 3.7 and 3.8, respectively. Finally, the conclusions are summarized in section 3.9.

3.1 The Limit Cycle Oscillator

A stable limit cycle can be described as the outcome of the evolution of the states of a two-dimensional dynamic system in which, its trajectories eventually tend to a closed orbit as the time tends to infinity. An isolated periodic orbit is called a limit cycle [44]. A nonlinear self-sustained sinusoidal oscillator with this property can be represented by the next second order dynamic system in polar coordinates:

$$\dot{r} = \left(1 - \frac{r^2}{A^2}\right) r \omega, \quad (3.1a)$$

$$\dot{\theta} = -\omega, \quad (3.1b)$$

where r is the oscillation radius, ω is the angular frequency, and A is the peak amplitude of r . Equation (3.1a) has three equilibrium points, one of them is unstable in $r^* = 0$, and two are stable in $r^{**} = \pm A$ (Refer to Appendix 9.1 for Lyapunov stability analysis). Hereafter, it will be assumed that $r > 0$. Figure 3.1 (a) shows that the entire vector field points to a drain in $r = A$ and the solutions go through of it, with a velocity of $-\omega$; i.e.:

$$r_1 < A \rightarrow \dot{r} > 0, \quad (3.2a)$$

$$r_2 > A \rightarrow \dot{r} < 0. \quad (3.2b)$$

The system (3.1) is written in Cartesian coordinates as:

$$\dot{x}_1 = \left[x_1 + x_2 - \frac{x_1}{A^2} (x_1^2 + x_2^2) \right] \omega, \quad (3.3a)$$

$$\dot{x}_2 = \left[-x_1 + x_2 - \frac{x_2}{A^2} (x_1^2 + x_2^2) \right] \omega, \quad (3.3b)$$

where x_1 and x_2 are two in-quadrature signals. The behavior of the vector field (3.2) over the system (3.3) is depicted in Figure 3.1 (b). It is demonstrated by Poincaré-Bendixson Theorem [45], that (3.3) is a closed orbit and it can be named as LCO, as shown in Figure 3.1 (c) where all the vector field points towards the limit cycle, irrespective of initial conditions.

The solutions of system (3.3) are given by:

$$x_1(t) = -A \cos(\omega t), \quad (3.4a)$$

$$x_2(t) = A \sin(\omega t), \quad (3.4b)$$

which can be seen in Figure 3.1 (d) as trajectories for x_1 and x_2 in a temporal chart.

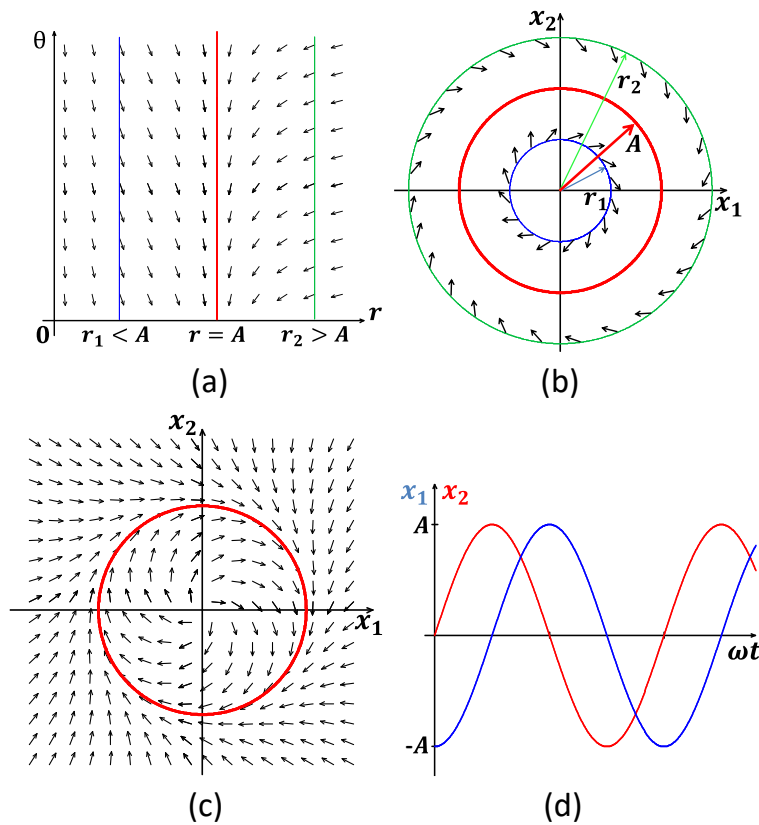


Figure 3.1. (a) Direction of the vector field of (3.1) in two surfaces, smaller and greater than $r = A$. (b) Direction of the vector field (3.2) in the transformed system (3.3) in Cartesian coordinates. (c) Phase portrait of (3.3) and the limit cycle. (d) Temporal chart of the solutions of system (3.3).

In the case of a linear harmonic oscillator as SOGI, there is a continuum of closed orbits, whereas, in the LCO (3.3), there is only one isolated closed orbit. This characteristic makes the LCO robust for perturbations as swells and sags near of the oscillation radius A , and it makes the system structurally stable in a highly polluted grid. Another feature of (3.3) is the robustness on initial conditions; in other words, the system (3.3) guarantees an acceptable transient from any particular initial condition to the limit cycle, as depicted in Figure 3.1 (c).

3.2 The Interconnection of LCO-FLL

The FLL was formally introduced in [37] as an effective tool to adapt the center frequency of the linear harmonic oscillator SOGI, by means of the product of the quadrature signal and the voltage error signal, which is processed by an integrator to obtain the estimated center grid frequency. The FLL does not use phase-angles or trigonometric functions. Moreover, results on local stability and tuning were shown in [35].

The FLL is utilized in order to give a frequency adaptation to the LCO. The interconnection between the LCO and the FLL is made in a way that the features and advantages of both systems are preserved. This is achieved by making adaptive only the phase and frequency variation of (3.1), reducing the error signal between an input signal v and the oscillation radius r . In this way, the LCO (3.1) and the FLL are interconnected and the LCO-FLL is written in polar coordinates as:

$$\dot{\theta} = -[r - k\varepsilon_v \cos(\theta)] \frac{\omega}{r}, \quad (3.5a)$$

$$\dot{r} = \left(r - \frac{r^3}{A^2} + k\varepsilon_v \sin(\theta) \right) \omega, \quad (3.5b)$$

$$\dot{x}_3 = -\gamma\varepsilon_v r \cos(\theta), \quad (3.5c)$$

where $\gamma, k \in R^+$ are gains, $\omega = x_3 + \omega_{ffw}$ is the angular frequency with ω_{ffw} as a constant, and the $\varepsilon_v = v - r \sin(\theta)$ is the voltage error signal between the input signal v and one component of the oscillation radius $r \sin(\theta)$. The other component of the oscillation radius $r \cos(\theta)$ is multiplying the ε_v in the FLL (3.5c) in order to get the phase and frequency of the reference v . Now, transforming (3.5) to cartesian coordinates, the

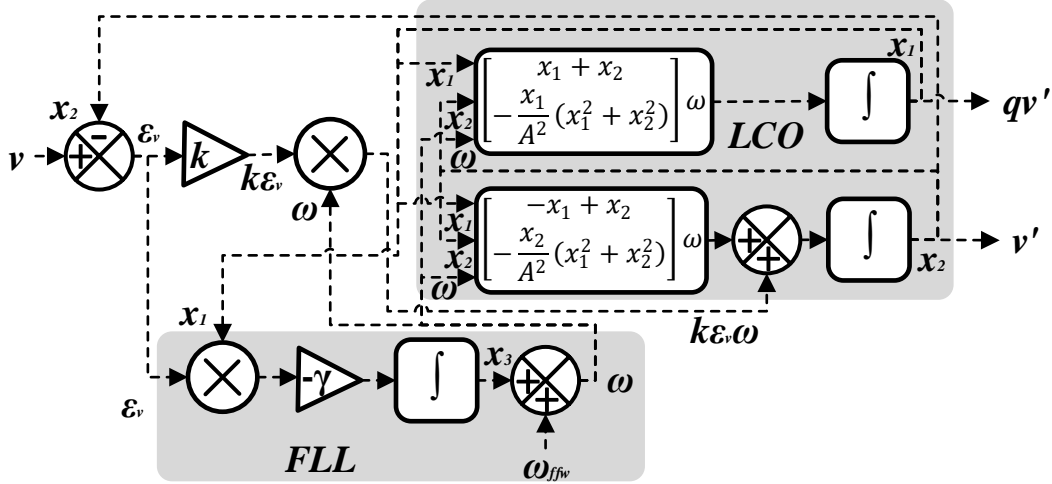


Figure 3.2. LCO-FLL block diagram.

following system is obtained:

$$\dot{x}_1 = \left(x_1 + x_2 - \frac{x_1}{A^2} (x_1^2 + x_2^2) \right) \omega, \quad (3.6a)$$

$$\dot{x}_2 = k\varepsilon_v \omega + \left(-x_1 + x_2 - \frac{x_2}{A^2} (x_1^2 + x_2^2) \right) \omega, \quad (3.6b)$$

$$\dot{x}_3 = -\gamma \varepsilon_v x_1, \quad (3.6c)$$

where $\varepsilon_v = v - x_2$ is the voltage error signal between the input signal v and the signal x_2 . It can be seen in (3.6c) the FLL as the product of the quadrature signal x_1 and the voltage error ε_v .

If the input signal v is chosen as a sinusoidal signal:

$$v = A \sin(\theta_{ref}), \quad (3.7a)$$

which is governed by:

$$\dot{\theta}_{ref} = -\omega_{ref}, \quad (3.7b)$$

with θ_{ref} and ω_{ref} as the input signal phase and angular frequency, respectively. It is straightforward to see that $k\varepsilon_v \omega$ from (3.6b) and (3.6c) tends to zero as the error signal ε_v vanishes. Thus, the LCO-FLL (3.6) has the behavior of (3.3) with the difference that (3.6) oscillates at the angular frequency ω_{ref} and phase θ_{ref} of the input signal (3.7a).

The interconnected dynamic system LCO-FLL (3.6) can be shown as a block diagram in Figure 3.2 where it can be seen two main outputs, the quadrature signal $qv' = x_1$ and

the signal $v' = x_2$, which is synchronized with the input v . Notice that A is a constant in (3.6), this makes the system (3.6) robust against amplitude perturbations such as spikes, notches, swells and sags within the normal operation in grid voltage.

3.3 Stability Analysis of LCO-FLL

In order to proof local stability, the system (3.5) is analyzed. Using the input signal (3.7a), it can be seen that (3.5c) vanishes as (3.5) synchronize with it. In order to include the dynamic of (3.7b), a phase error variable is created:

$$\Delta\theta = \theta - \theta_{ref}. \quad (3.8)$$

Therefore, the dynamic of (3.7b) and (3.5) is described by:

$$\dot{r} = \left(r - \frac{r^3}{A^2} + k\varepsilon_v \sin(\Delta\theta + \theta_{ref}) \right) \omega, \quad (3.9a)$$

$$\Delta\dot{\theta} = \omega_{ref} - \left(r - k\varepsilon_v \cos(\Delta\theta + \theta_{ref}) \right) \frac{\omega}{r}, \quad (3.9b)$$

$$\dot{x}_3 = -\gamma\varepsilon_v r \cos(\Delta\theta + \theta_{ref}), \quad (3.9c)$$

with $\varepsilon_v = v - r \sin(\Delta\theta + \theta_{ref})$. It can be seen that the system (3.9) has the following equilibrium point:

$$x^* = \{r = A, \Delta\theta = 0, x_3 = \omega_{ref} - \omega_{ffw}\}. \quad (3.10)$$

Jacobian evaluation of system (3.9) at the equilibrium point x^* is:

$$J(x^*) = \begin{bmatrix} (-2 - k \sin^2(\theta_{ref}))\omega_{ref} & kA \sin(\theta_{ref}) \cos(\theta_{ref})\omega_{ref} & 0 \\ k \sin(\theta_{ref}) \cos(\theta_{ref}) \frac{\omega_{ref}}{A} & -k \cos^2(\theta_{ref})\omega_{ref} & 1 \\ \gamma A \sin(\theta_{ref}) \cos(\theta_{ref}) & -\gamma A^2 \cos^2(\theta_{ref}) & 0 \end{bmatrix}. \quad (3.11)$$

Obtaining the characteristic polynomial from (3.11):

$$\lambda^3 + \lambda^2[\omega_{ref}(2+k)] + \lambda[(2\omega_{ref}^2 k + \gamma A^2)(\cos^2(\theta_{ref}))] + [2\omega_{ref}\gamma A^2 \cos^2(\theta_{ref})] = 0. \quad (3.12)$$

Analyzing (3.12) by the Routh stability criterion, it can be deduced that all three eigenvalues of (3.12) have always negative real part when $\cos^2(\theta_{ref}) \neq 0$, since

$$2\omega_{ref}^2(2+k) + \gamma A^2 > 0 \quad (3.13)$$

is always fulfilled. That is, x^* is an asymptotically stable equilibrium point. In the moment when the reference signal v crosses the zero, that is, when $\cos^2(\theta_{ref}) = 0$, there are two zero eigenvalues and the third-one is negative ($-\omega_{ref}(2+k)$), which makes x^* marginally stable two times per period of ω_{ref} .

3.4 Synchronization Stability Numerical Analysis of the LCO-FLL

A wide stability analysis over the LCO-FLL is depicted in this section. Using the following new variables:

$$y_1 = r - A, \quad (3.14a)$$

$$y_2 = \Delta\theta, \quad (3.14b)$$

$$y_3 = x_3 - \omega_{ref} + \omega_{ffw}, \quad (3.14c)$$

it is possible to put the equilibrium point of the LCO-FLL (3.9) in the origin:

$$\dot{y}_1 = \left((y_1 + A) - \frac{(y_1 + A)^3}{A^2} + k\varepsilon_v \sin(y_2 + \theta_{ref}) \right) \omega, \quad (3.15a)$$

$$\dot{y}_2 = \omega_{ref} - \left((y_1 + A) - k\varepsilon_v \cos(y_2 + \theta_{ref}) \right) \frac{\omega}{(y_1 + A)}, \quad (3.15b)$$

$$\dot{y}_3 = -\gamma\varepsilon_v(y_1 + A) \cos(y_2 + \theta_{ref}), \quad (3.15c)$$

with:

$$\varepsilon_v = A \sin(\theta_{ref}) - (y_1 + A)\sin(y_2 + \theta_{ref}), \quad (3.16a)$$

$$\omega = y_3 + \omega_{ref}. \quad (3.16b)$$

In this sense, the equilibrium point of (3.15) is:

$$y^* = \{y_{1,2,3} = 0\}. \quad (3.17)$$

Now, making (3.15) as:

$$\mathbf{f} = [\dot{y}_1, \dot{y}_2, \dot{y}_3]^T \quad (3.18)$$

and by means of Krasovskii's theorem (states below), It can be proven that there are regions where the equilibrium point in the origin is asymptotically stable.

Krasovskii's Theorem. *Consider the next autonomous system, with the equilibrium point of interest being the origin.*

$$\dot{\mathbf{x}} = \mathbf{f}(\mathbf{x}). \quad (3.19)$$

Let $\mathbf{A}(\mathbf{x})$ denote, the Jacobian matrix of the system, i.e.,

$$\mathbf{A}(\mathbf{x}) = \frac{\partial \mathbf{f}}{\partial \mathbf{x}} \quad (3.20)$$

if the matrix $\mathbf{F} = \mathbf{A} + \mathbf{A}^T$ is negative definite in a neighborhood Ω , then the equilibrium point at the origin is asymptotically stable. A Lyapunov function for this system is:

$$\mathbf{V}(\mathbf{x}) = \mathbf{f}^T(\mathbf{x})\mathbf{f}(\mathbf{x}) \quad (3.21)$$

if Ω is the entire state space and, in addition, $\mathbf{V}(\mathbf{x}) \rightarrow \infty$ as $\|\mathbf{x}\| \rightarrow \infty$, then the equilibrium point is globally asymptotically stable [46].

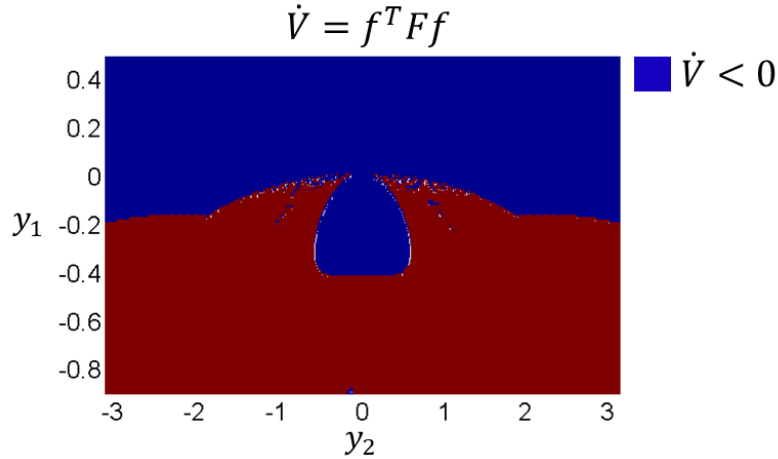


Figure 3.3. Region where $\dot{V} < 0$ is evaluated in an amplitude variation of (0.1A – 1.5A), and a frequency variation of ± 0.63 Hz. LCO-FLL parameters: $k = 1, \gamma = 5$. Range of amplitude, phase and frequency evaluated: $y_1 = [-0.9A, 0.5A], y_2 = [-\pi, \pi], y_3 = [-4, 4]$ respectively.

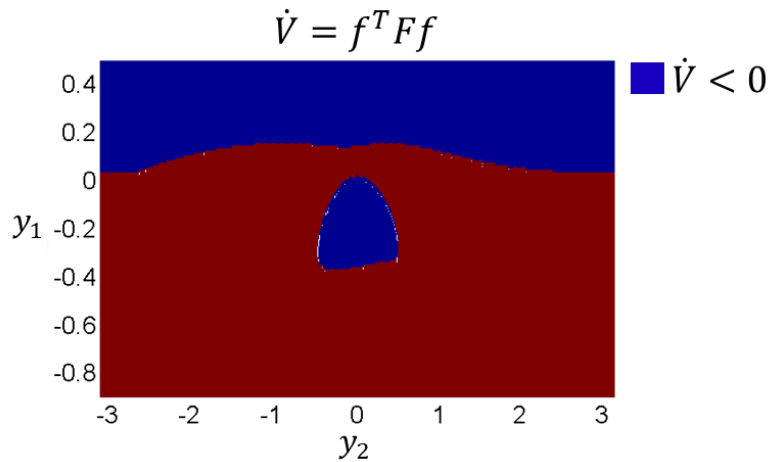


Figure 3.4. Region where $\dot{V} < 0$ is evaluated in an amplitude variation of (0.1A – 1.5A), and a frequency variation of ± 40.74 Hz. LCO-FLL parameters: $k = 1, \gamma = 5$. Range of amplitude, phase and frequency evaluated: $y_1 = [-0.9A, 0.5A], y_2 = [-\pi, \pi], y_3 = [-256, 256]$ respectively.

In Figure 3.3 it can be seen the region in blue where the Lyapunov function (3.21) applied to the system (3.15) has $\dot{V} < 0$. In this region it can be ensured that the equilibrium point in the origin (3.17) of the system (3.15) is asymptotically stable, depending in the range of amplitude, phase and frequency evaluated.

It is important to highlight that this region where it can be ensuring stability get narrow depending on the frequency variation evaluated in (3.21). In other words, the

more frequency variation, the narrower get this region, as it is depicted in Figure 3.4 where a bigger frequency variation of $\pm 40.74 \text{ Hz}$ is evaluated. This wider variation of frequency produces two disconnected regions where $\dot{V} < 0$, making this phenomenon an interesting topic for future work in stability analysis in synchronization systems, in order to find these regions theoretically, and to get at least, limits in function of amplitude, phase and frequency variations where stability can be guaranteed.

3.5 Three-Phase LCO-FLL Case and Sequence-Components Detection

It is well known [47] that a three-phase signal vector \mathbf{v}_{abc} can be separated into three instantaneous components named positive, negative, and zero sequence as follows:

$$\mathbf{v}_{abc} = \mathbf{v}_{abc}^+ + \mathbf{v}_{abc}^- + \mathbf{v}_{abc}^0, \quad (3.22a)$$

$$\mathbf{v}_{abc}^+ = [\mathbf{T}_+] \mathbf{v}_{abc}, \quad (3.22b)$$

$$\mathbf{v}_{abc}^- = [\mathbf{T}_-] \mathbf{v}_{abc}, \quad (3.22c)$$

$$\mathbf{v}_{abc}^0 = [\mathbf{T}_0] \mathbf{v}_{abc}, \quad (3.22d)$$

with

$$[\mathbf{T}_+] = \frac{1}{3} \begin{pmatrix} 1 & \alpha & \alpha^2 \\ \alpha^2 & 1 & \alpha \\ \alpha & \alpha^2 & 1 \end{pmatrix}, \quad (3.23a)$$

$$[\mathbf{T}_-] = \frac{1}{3} \begin{pmatrix} 1 & \alpha^2 & \alpha \\ \alpha & 1 & \alpha^2 \\ \alpha^2 & \alpha & 1 \end{pmatrix}, \quad (3.23b)$$

$$[\mathbf{T}_0] = \frac{1}{3} \begin{pmatrix} 1 & 1 & 1 \\ 1 & 1 & 1 \\ 1 & 1 & 1 \end{pmatrix}, \quad (3.23c)$$

where $\alpha = e^{j(2\pi/3)}$ is the operator applied over the input signals. The positive (3.22b) and negative sequence (3.22c) are a set of three balanced signals (120° phase shifted) and the zero sequence (3.22d) is a set of three signals with the same amplitude and phase.

The $\alpha\beta 0$ transformation allows to separate the zero sequence from the phases components (3.22b) and (3.22c); furthermore, the α and β components do not contribute to the zero-sequence components. This advantage can be used in three-wire power converters as well as in four-wire systems where the three-phase voltage is balanced. In such cases, the voltage zero-sequence is absent and the voltage can be synchronized just with the positive and negative sequence components of the grid voltage, using the Clarke transformation [47], which changes from the abc to the $\alpha\beta$ Stationary Reference Frames (SRF).

In order to synchronize the instantaneous positive and negative sequence components, a three-phase LCO-FLL is implemented using the single-phase structure depicted in Figure 3.2. The Clarke's transformation module ($\mathbf{T}_{\alpha\beta}$) is multiplied with the three-phase vector. The α and β signals are processed by two LCO-FLL modules. After that, the synchronized and the quadrature signals are multiplied by two matrices of positive [\mathbf{T}^+] and negative sequence [\mathbf{T}^-], which are multiplied by an inverse Clarke's transformation. Hence:

$$\mathbf{v}_{abc}^+ = [\mathbf{T}_{\alpha\beta}^{-1}][\mathbf{T}^+][LCO - FLL][\mathbf{T}_{\alpha\beta}]\mathbf{v}_{abc}, \quad (3.24a)$$

$$\mathbf{v}_{abc}^- = [\mathbf{T}_{\alpha\beta}^{-1}][\mathbf{T}^-][LCO - FLL][\mathbf{T}_{\alpha\beta}]\mathbf{v}_{abc}, \quad (3.24b)$$

where:

$$[\mathbf{T}_{\alpha\beta}] = \sqrt{\frac{2}{3}} \begin{pmatrix} 1 & -1/2 & -1/2 \\ 0 & \sqrt{3}/2 & -\sqrt{3}/2 \end{pmatrix}, \quad (3.25a)$$

$$[\mathbf{T}_{\alpha\beta}^{-1}] = \sqrt{\frac{2}{3}} \begin{pmatrix} 1 & 0 \\ -1/2 & \sqrt{3}/2 \\ -1/2 & -\sqrt{3}/2 \end{pmatrix}, \quad (3.25b)$$

$$[\mathbf{T}^+] = \frac{1}{2} \begin{pmatrix} 1 & 0 & 0 & 1 \\ 0 & -1 & 1 & 0 \end{pmatrix}, \quad (3.26a)$$

$$[\mathbf{T}^-] = \frac{1}{2} \begin{pmatrix} 1 & 0 & 0 & -1 \\ 0 & 1 & 1 & 0 \end{pmatrix}. \quad (3.26b)$$

It is important to highlight that the two LCO-FLL modules are working on the $\alpha\beta$ SRF with the output signals connected to a positive [\mathbf{T}^+] and negative sequence detection matrices [\mathbf{T}^-], which implement the transformations in (3.26). Since the LCO-FLL behaves

as a quadrature signal generator itself, the matrices for the two modules of LCO-FLL can be represented by:

$$[LCO - FLL] = \begin{pmatrix} 1 & 0 \\ q & 0 \\ 0 & 1 \\ 0 & q \end{pmatrix}, \quad (3.27)$$

with $q = e^{j(\pi/2)}$. Moreover, equations (3.22b), (3.22c) and (3.24) imply that:

$$\mathbf{T}_+ = [\mathbf{T}_{\alpha\beta}^{-1}][\mathbf{T}^+][LCO - FLL][\mathbf{T}_{\alpha\beta}], \quad (3.28a)$$

$$\mathbf{T}_- = [\mathbf{T}_{\alpha\beta}^{-1}][\mathbf{T}^-][LCO - FLL][\mathbf{T}_{\alpha\beta}], \quad (3.28b)$$

with the difference that in (3.24), the positive and negative sequence components are synchronized with \mathbf{v}_{abc} . The representation in block diagrams of the synchronization structure of (3.24) is shown in Figure 3.5, which resembles the one in [35].

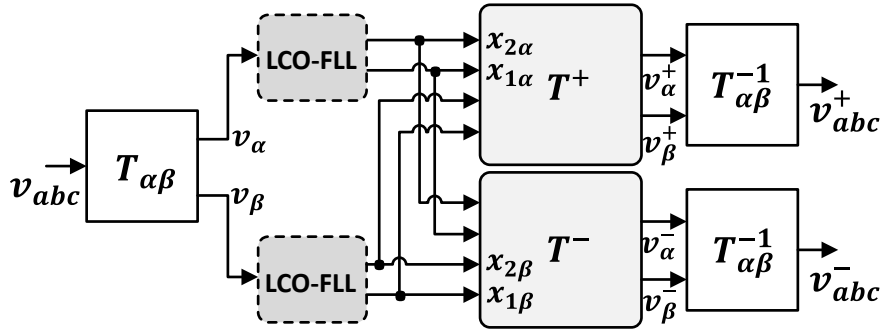


Figure 3.5. Block diagram of the three-phase LCO-FLL with sequence components detection.

3.6 Experimental Results

Nonlinear synchronization systems, as the SOGI-FLL [39], and the ANF [38] were chosen in order to have a comparison point of the LCO-FLL performance. These systems, LCO-FLL, SOGI-FLL, and ANF were implemented in a Single Board of National Instruments based on an FPGA Xilinx Spartan-6 LX45 at 2.5 MHz. The distorted input signals, single-phase, and three-phase cases, were generated by a programmable waveform source. The

experimental output signal result of each system was taken directly from the Digital Analog Converter (DAC) of the control board. Moreover, in Table III.I, the performance of the proposed technique is compared to the most representative PLL based algorithms of [48]. Which are the Low-pass-filters Synchronous Reference Frame - PLL (LSRF-PLL), Multiple Reference Frame - PLL (MRF-PLL), and the Dual Second Order Generalized Integrator - PLL (DSOGI-PLL).

A. INITIALIZATION SETTINGS

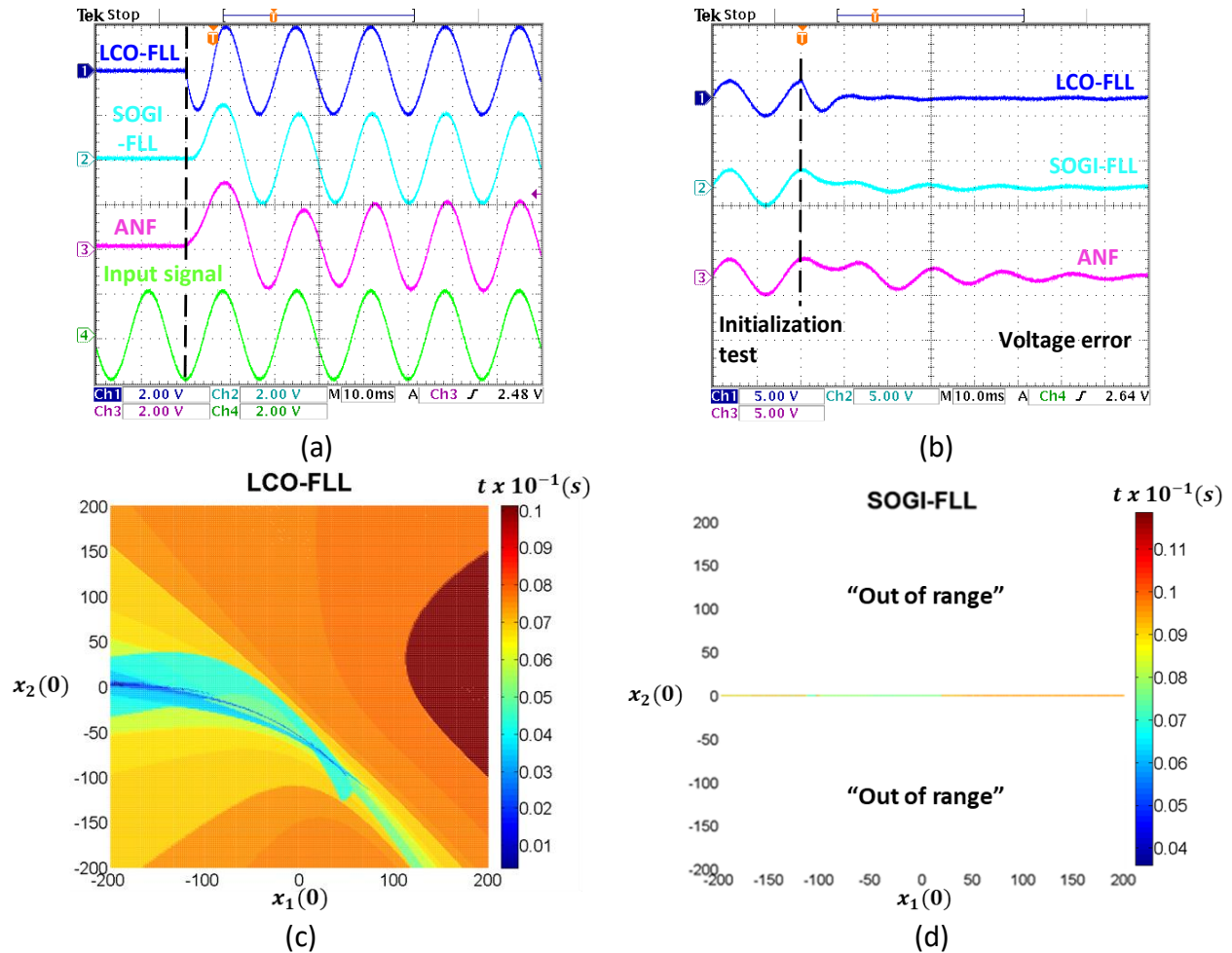


Figure 3.6. Initialization test. (a) Transient behavior (2 V/div-10 ms/div). (b) Voltage Error (5 V/div-10 ms/div). Convergence times in function of the initial conditions $x_1(0)$ and $x_2(0)$ for (c) LCO-FLL, and (d) SOGI-FLL.

A test to see the transient behavior of LCO-FLL, SOGI-FLL, and ANF systems is depicted in Figure 3.6 (a), which shows the LCO-FLL (Ch1), SOGI-LL (Ch2), ANF (Ch3), and the input signal (Ch4) trajectories. The frequency of the input signal is set to 50 Hz. Figure 3.6 (b) shows the voltage error between the input signal and every system. It can be seen that the LCO-FLL is locked to the input signal in about ~ 0.5 cycles with a good transient time. However, SOGI-FLL and ANF, show underdamped transient errors and longer settling times, 2 and 3.5 cycles respectively. Table III.I summarizes the optimized parameters and the settling times of every synchronization technique, including the PLL based algorithms. It can be seen that LSRF-PLL, MRF-PLL, and DSOGI-PLL takes between 1.5 and 3 cycles to lock the input signal [48], [49].

Optimized parameters for LCO-FLL were chosen in order to have a tradeoff between dynamical response and filtering capability. That is, a large value of k will make the LCO-FLL performance fast, reducing its immunity to the effects of harmonics in the input signal. On the contrary, a low value for k makes the LCO-FLL very selective in frequency but it takes longer stabilization times.

Another important element to analyze is the transient and the time that take the trajectories from a specific initial condition $x_1(0), x_2(0)$ to the equilibrium point x^* (3.10). In order to have a comparison point of view, the LCO-FLL was contrasted with the SOGI-FLL, and they are depicted in Figure 3.6 (c) and (d).

Both systems are set with initial conditions located in the voltage physical operation range of $D_{ini}: \{-200 \leq x_1(0), x_2(0) \leq 200\}$. Moreover, the reference (3.7a) with values $\omega_{ref} = 377$ rad/s, $\gamma = 1$ and $k = 1$ is considered. Differences between times of convergence as a function of the initial conditions can be observed in Figure 3.6 (c). In other words, LCO-FLL converges and synchronizes within a finite time to the reference in the whole range of D_{ini} . The section of the Figure 3.6 (d) with no data time (white zone) means that the trajectory solution of x_1 in the SOGI-FLL is out of range from D_{ini} , i.e. the trajectory for x_1 diverges at least in one period of time from D_{ini} , producing unwanted transients by the SOGI-FLL trajectories for those initial conditions. Nevertheless, within the narrow stripe showed in Figure 3.6 (d), SOGI-FLL synchronizes with the reference signal and the solution x_1 remains within the region defined by D_{ini} .

Summarizing above, LCO-FLL synchronizes with the reference for every initial condition in D_{ini} and its trajectories stay within the enclosed region D_{ini} . On the other hand, SOGI-FLL synchronizes with the reference just within a narrow stripe of initial conditions $x_1(0), x_2(0)$.

B. FREQUENCY STEP TEST

A frequency variation test was implemented for LCO-FLL, SOGI-FLL, and ANF systems. The input signal has a frequency step of +5 Hz from 50 to 55 Hz. As it can be seen in Figure 3.7 (a), the LCO-FLL takes about 1.8 cycles to lock the new frequency. However, SOGI-FLL and ANF take longer times, around 6 and 3 cycles, respectively.

Table III.I summarizes the settling times, phase errors, and frequency deviations of every system. It can be seen that PLL based algorithms have also longer settling times and greater peak phase-errors than LCO-FLL. Moreover, they present a frequency deviation, while the proposed method, SOGI-FLL, and ANF show a damped frequency trajectory.

C. PHASE STEP TEST

Figure 3.7 (b) shows the experimental response after a phase jump of 40° in the input signal. It can be seen that LCO-FLL takes less time to reach the new phase and greater frequency deviation than SOGI-FLL and ANF.

Table III.I shows the settling times, phase errors, and peak frequency deviations of every system. It can be seen that PLL based algorithms have similar settling times, but greater peak phase-errors and much greater peak frequency deviations than LCO-FLL, SOGI-FLL, and ANF.

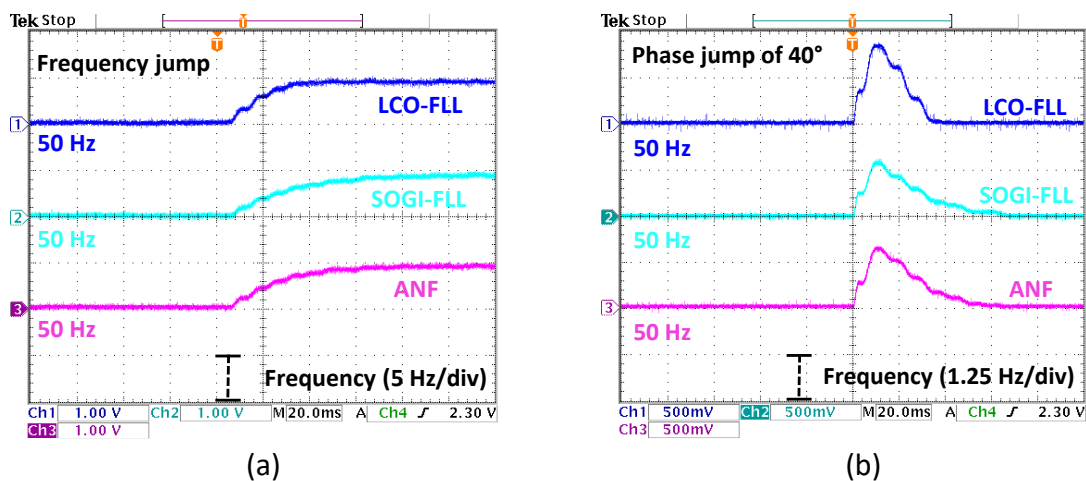


Figure 3.7. Experimental response when the input voltage undergoes a frequency step change of 5 Hz. (a) Frequency estimation (5 Hz/div-20 ms/div). Experimental response when the input voltage has a phase jump of 40° (b) Frequency estimation (1.25 Hz/div-20 ms/div).

D. AMPLITUDE CHANGE TEST

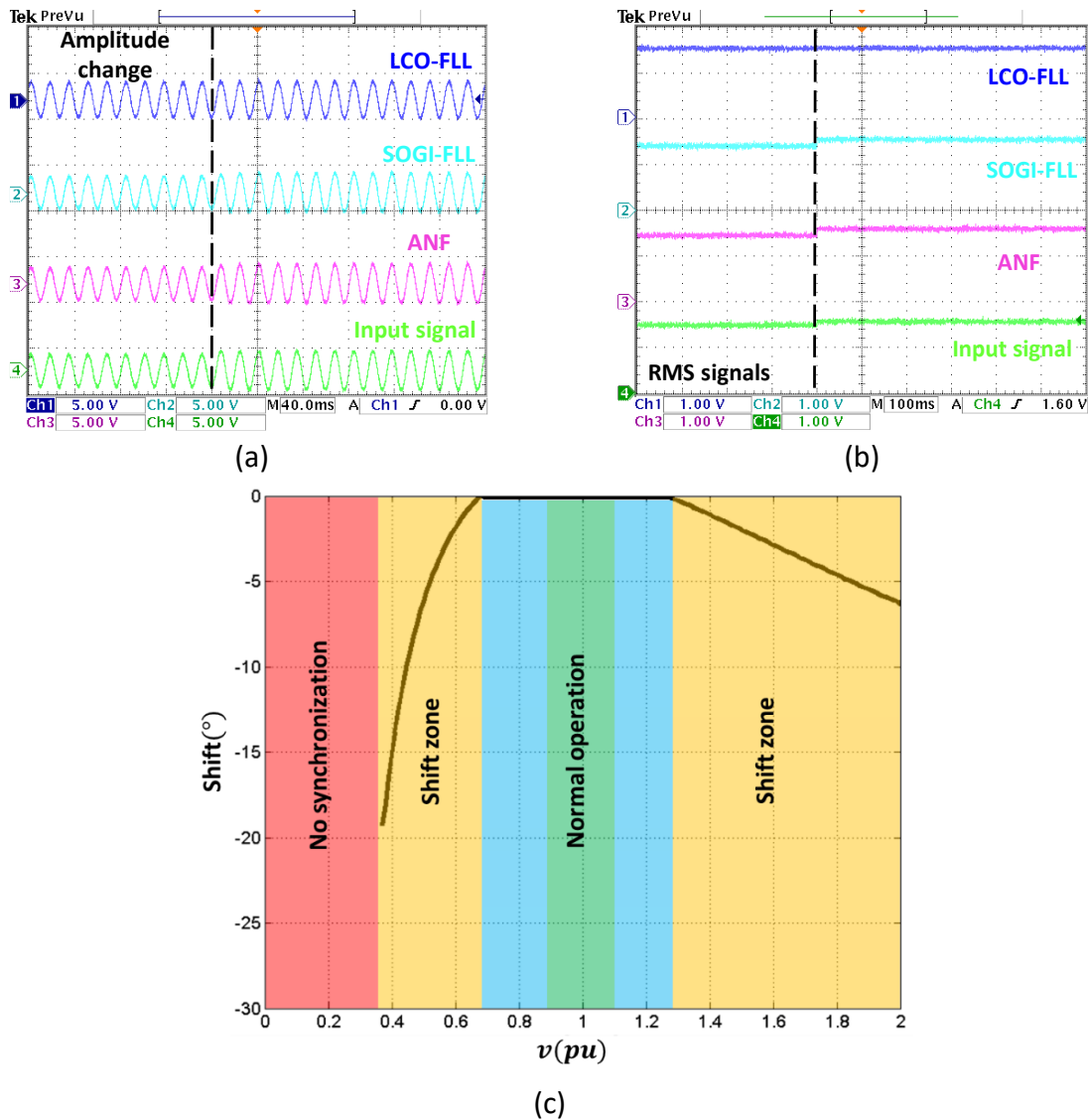


Figure 3.8. Experimental response of LCO-FLL, SOGI-FLL, and ANF under amplitude variations within $88\% \leq V \leq 110\%$. (a) Synchronized systems and the input signal (5V/div-40 ms/div). (b) RMS signals (1V/div-100 ms/div). (c) Zones of amplitude robustness of the LCO-FLL.

An amplitude variation test in the input signal was made within the normal operation zone marked by the IEEE 1547 Standard, which is $88\% \leq V \leq 110\%$. Figure 3.8 (a) illustrates the LCO-FLL, SOGI-FLL, and ANF locked to the input signal, under an amplitude variation. Figure 3.8 (b) shows the RMS signals of every system. Notice that the RMS signal of the LCO-FLL remains constant in the presence of amplitude variations in the

input signal, however, the SOGI-FLL and the ANF RMS signals follow the input, which is not desirable if the output is used as a constant amplitude signal for a controller.

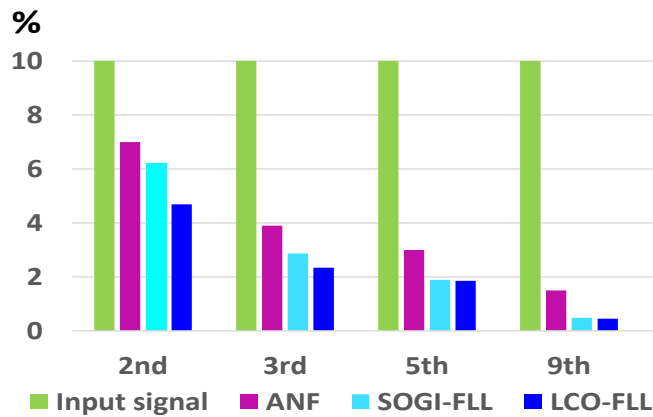
The synchronization and the voltage amplitude robustness of the LCO-FLL remain within (0.88-1.1) p.u. Even more, these characteristics are maintained in a wider range $\sim(0.69-1.27)$ p.u. due to the robustness of the LCO. Outside of this range, the synchronized signal has a delay with respect to the grid signal, however, it is still synchronized in frequency, thanks to the FLL. Under ~ 0.36 p.u., there will be no synchronization due to the significant difference of amplitude between A and the input signal, nevertheless, the proposed method is still stable, even in the absence of an input signal, as it can be seen in Figure 3.8 (c). It is important to highlight that there are islanding detection methods that manage these type of circumstances in which, the system is disconnected [50].

E. DISTORTION TEST

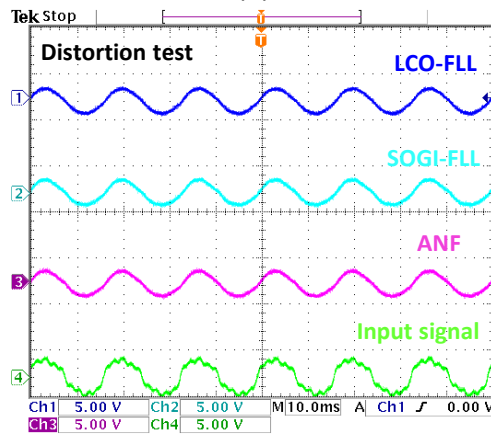
A distorted input voltage test was generated with the 2nd, 3rd, 5th, and 9th harmonic with the percentage indicated in Figure 3.9 (a). The Total Harmonic Distortion (THD) of the input voltage is 20%. The LCO-FLL, SOGI-FLL, and ANF systems reduce the THD to 5.5%, 7.2%, and 9% respectively, the signals are depicted in Figure 3.9 (b). These techniques have good filtering characteristics; however, LCO-FLL has a better performance in reducing the harmonic disturbance (cf. Figure 3.9 (a)). As it can be seen in Figure 3.9 (c) and Table III.I, the frequency and phase errors of LCO-FLL, SOGI-FLL, and ANF are relatively smaller than in PLL base algorithms.

F. IMPLEMENTATION DETAILS

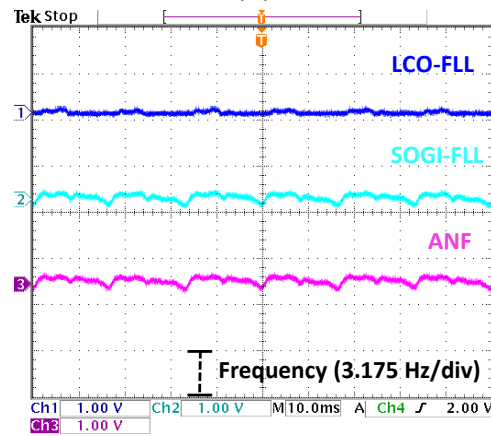
Table III.I synthesizes the computation burden comparison, performance and features of LCO-FLL, SOGI-FLL, ANF, and PLL based algorithms. It shows that LCO-FLL has better performance than SOGI-FLL and ANF, by practically using the same number of slices, registers, and look-up tables (LUTs). It also shows that LCO-FLL consumes fewer computation resources and it has better performance than PLL based algorithms [51], [48]. It is important to highlight that LCO-FLL is the only one with output amplitude robustness.



(a)



(b)



(c)

Figure 3.9. Experimental response of LCO-FLL, SOGI-FLL, and ANF under distorted input signal. (a) Harmonic percentage table. (b) Synchronized systems and the input signal (5 V/div-10 ms/div). (c) Frequency error (3.175 Hz/div-10 ms/div).

TABLE III.I
COMPARISON SUMMARY OF THE NONLINEAR SYNCHRONIZATION SYSTEMS

	Proposed LCO-FLL	SOGI-FLL ^a	ANF ^b	LSRF-PLL ^c	MRF-PLL ^c	DSOGI-PLL ^c
Initialization settings						
<i>Optimized parameters</i>	$k=1$ $\gamma=5$	$k=\text{sqrt}(2)$ $\gamma=4$	$\zeta=0.6$ $\gamma=800$	$k_p=96.13$ $k_i=3850$ $\omega_p=73.44 \pi$	$k_p=138.23$ $k_i=7961$ $\omega_p=105.6\pi$ $k=2.11$	$k_p=138.23$ $k_i=7961$ $\omega_p=105.6\pi$ $k=2.11$
<i>Settling time (2% error)</i>	≈ 0.5 cycles	≈ 2 cycles	≈ 3.5 cycles	≈ 3 cycles	≈ 2 cycles	≈ 1.5 cycles
Frequency step +5Hz						
<i>Settling time (2% error)</i>	≈ 1.8 cycles	≈ 6 cycles	≈ 3 cycles	≈ 3.1 cycles	≈ 2.1 cycles	≈ 2.2 cycles
<i>Peak phase-error</i>	9.5°	10.5°	10.1°	16.2°	11.9°	11.8°
<i>Peak frequency deviation</i>	0 Hz	0 Hz	0 Hz	1.7 Hz	2 Hz	1.9 Hz
Phase step +40°						
<i>Settling time (2% error)</i>	≈ 1.9 cycles	≈ 3.1 cycles	≈ 3 cycles	≈ 3.1 cycles	≈ 2.1 cycles	≈ 2.2 cycles
<i>Peak phase-error</i>	10.6°	10.3°	11.1°	13.5°	16.3°	14.9°
<i>Peak frequency deviation</i>	2.1 Hz	1.5 Hz	1.7 Hz	8.5 Hz	13.9 Hz	14.2 Hz
Amplitude change						
<i>Output amplitude robustness</i>	yes	no	no	-	-	no
Distortion						
<i>THD reduction ^d</i>	5.5%	7.2%	9%	-	-	-
<i>Steady-state p-to-p phase error</i>	$\approx 0^\circ$	$\approx 0^\circ$	$\approx 0^\circ$	0.7°	0.15°	0.15°
<i>Steady-state p-to-p freq. error</i>	0.5 Hz	1.3 Hz	1.4 Hz	1.5 Hz	0.8 Hz	0.8 Hz
Implementation details						
<i>States variables / integrations</i>	3	3	3	2	4	4
<i>Multiplications / scaling operations</i>	10	5	5	9	23	15
<i>Additions / subtractions</i>	8	3	3	7	19	11
<i>Computation burden time</i>	0.4 μ s @ 2.5MHz	0.4 μ s @ 2.5MHz	0.4 μ s @ 2.5MHz	- @ 150MHz	- @ 150MHz	- @ 150MHz
<i>Slices-Registers-LUTs ^e</i>	551-1276-938	548-1276-927	563-1276-921	-	-	-
<i>Trigonometric functions</i>	no	no	no	yes	yes	yes

^a [39]; ^b [38]; ^c [48],[49]; ^d THD input = 20%; ^e Each slice is comprised of 4 LUTs and 8 flip-flops.

G. THREE-PHASE LCO-FLL SYSTEM EVALUATION

The experimental evaluations of the three-phase structure in Figure 3.5 are shown in Figure 3.10 and Figure 3.11. The optimized parameters for the two LCO-FLL modules are the same as in Table III.I. The Figure 3.10 (a) shows two scenarios defined in Table III.II: a prefault grid voltage scenario (half left side), which is a balanced three-phase sinusoidal voltage signal, i.e. $V_a = 1 \angle 120^\circ$ pu, $V_b = 1 \angle -120^\circ$ pu, and $V_c = 1 \angle 0^\circ$ pu. The second scenario is a fault grid (half right side), which is the same balanced three-phase system, plus a distorted voltage THD of 38.05% for every phase.

Figure 3.10 (b) and (c) shows the positive and negative sequence outputs from the structure in Figure 3.5, respectively. In this case, the system detects just a negative sequence before and after the fault grid, since the system is balanced. Despite the distorted grid voltage input, the system detects effectively the negative sequence, and

filtering characteristics in the half right side of Figure 3.10 (c) with a THD of 7.59% for every phase can be observed.

Finally, the next test is made in order to evaluate the system with an unbalanced input signal. Figure 3.11 (a) shows the scenarios defined in Table III.III: a prefault grid voltage scenario (half left side), which is a balanced three-phase sinusoidal voltage signal with a negative sequence. The second scenario is a fault grid (half right side), which is a distorted voltage with THD of 38.05% for every phase. Furthermore, an unbalanced grid voltage in phase V_c , i.e. $V_a = 1 \angle 120^\circ$ pu, $V_b = 1 \angle -120^\circ$ pu, and $V_c = 1 \angle 60^\circ$ pu, plus harmonic components for every phase.

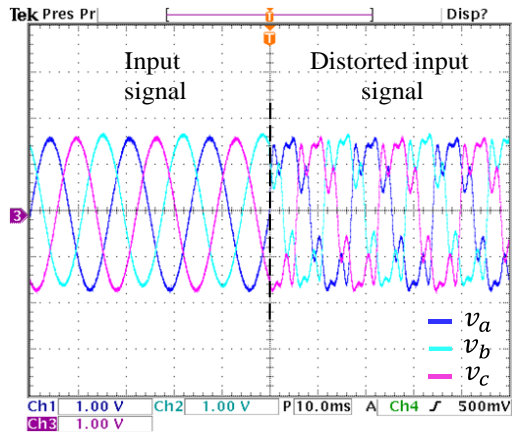
Figure 3.11 (b) and (c) shows the positive and negative sequence outputs from Figure 3.5, respectively. The system detects negative sequence in the prefault grid voltage scenario, since it is balanced, as it is shown in the half-left side of Figure 3.11 (c). On the half right side of Figure 3.11 (b) and (c), an increase of the positive sequence and the reduction of the negative sequence can be observed, due to the fault grid scenario. The system detects an unbalanced problem in less than a half grid voltage cycle, despite the distorted grid voltage input.

TABLE III.II
INPUT GRID VOLTAGE'S SCENARIOS FOR FIGURE 3.10 (A)

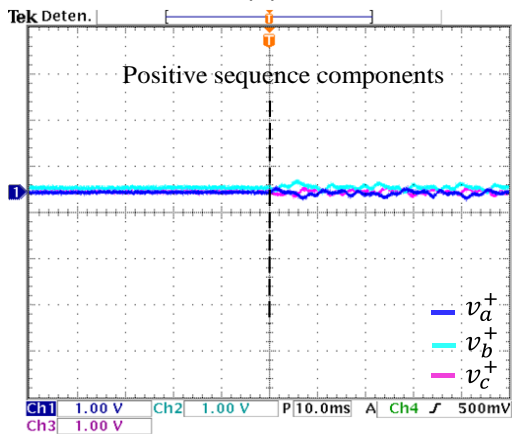
Prefault grid	Fault grid
$V_a=1 \angle 120^\circ$ pu	$V_a=1 \angle 120^\circ$ pu
$V_b=1 \angle -120^\circ$ pu	$V_b=1 \angle -120^\circ$ pu
$V_c=1 \angle 0^\circ$ pu	$V_c=1 \angle 0^\circ$ pu
THD=0%	THD=38.05%

TABLE III.III
INPUT GRID VOLTAGE'S SCENARIOS FOR FIGURE 3.11 (A)

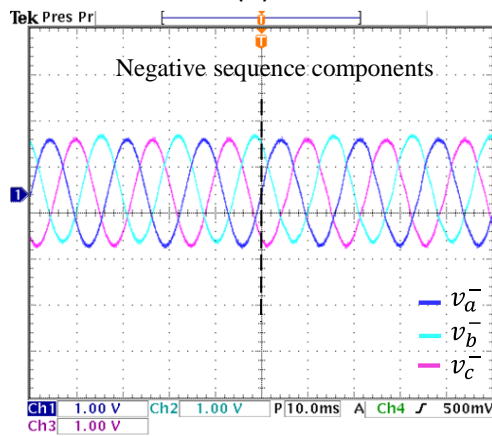
Prefault grid	Fault grid
$V_a=1 \angle 120^\circ$ pu	$V_a=1 \angle 120^\circ$ pu
$V_b=1 \angle -120^\circ$ pu	$V_b=1 \angle -120^\circ$ pu
$V_c=1 \angle 0^\circ$ pu	$V_c=1 \angle 60^\circ$ pu
THD=0%	THD=38.05%



(a)

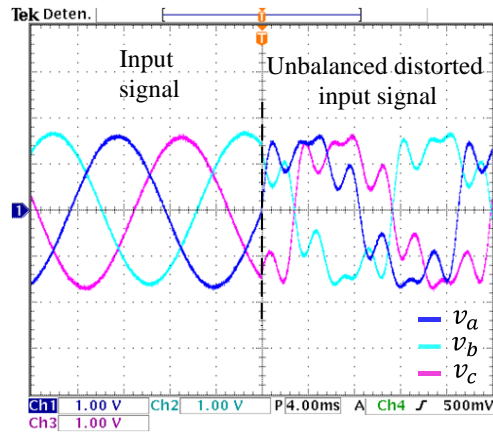


(b)

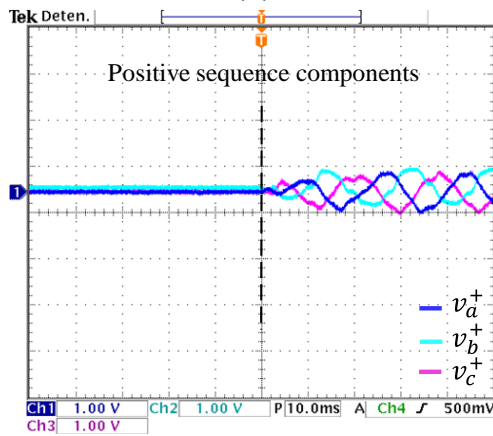


(c)

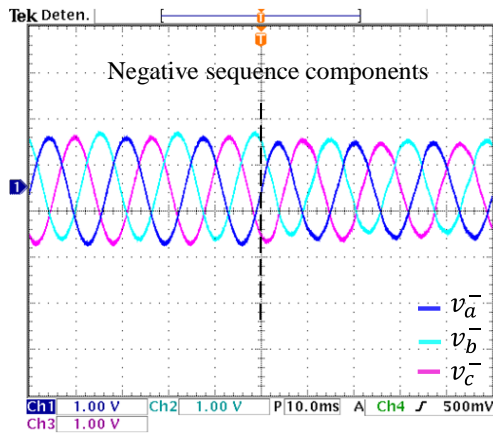
Figure 3.10. Experimental test of the Three-Phase LCO-FLL under sudden voltage distortion. (a) Three-phase input signal. (b) Positive sequence components. (c) Negative sequence components (1 V/div-10 ms/div).



(a)



(b)



(c)

Figure 3.11. Experimental test of the Three-Phase LCO-FLL under sudden voltage unbalance and distortion. (a) Three-Phase input signal (1 V/div-4 ms/div). (b) Positive sequence components. (c) Negative sequence components (1 V/div-10 ms/div).

3.7 Harmonic Detection System for Critical Loads, an application of the LCO-FLL

In this section, an extension of the block diagram of the three-phase LCO-FLL with sequence components detection of Figure 3.5 is shown. This system is called Multi-LCO for harmonics detection and it is depicted in Figure 3.12.

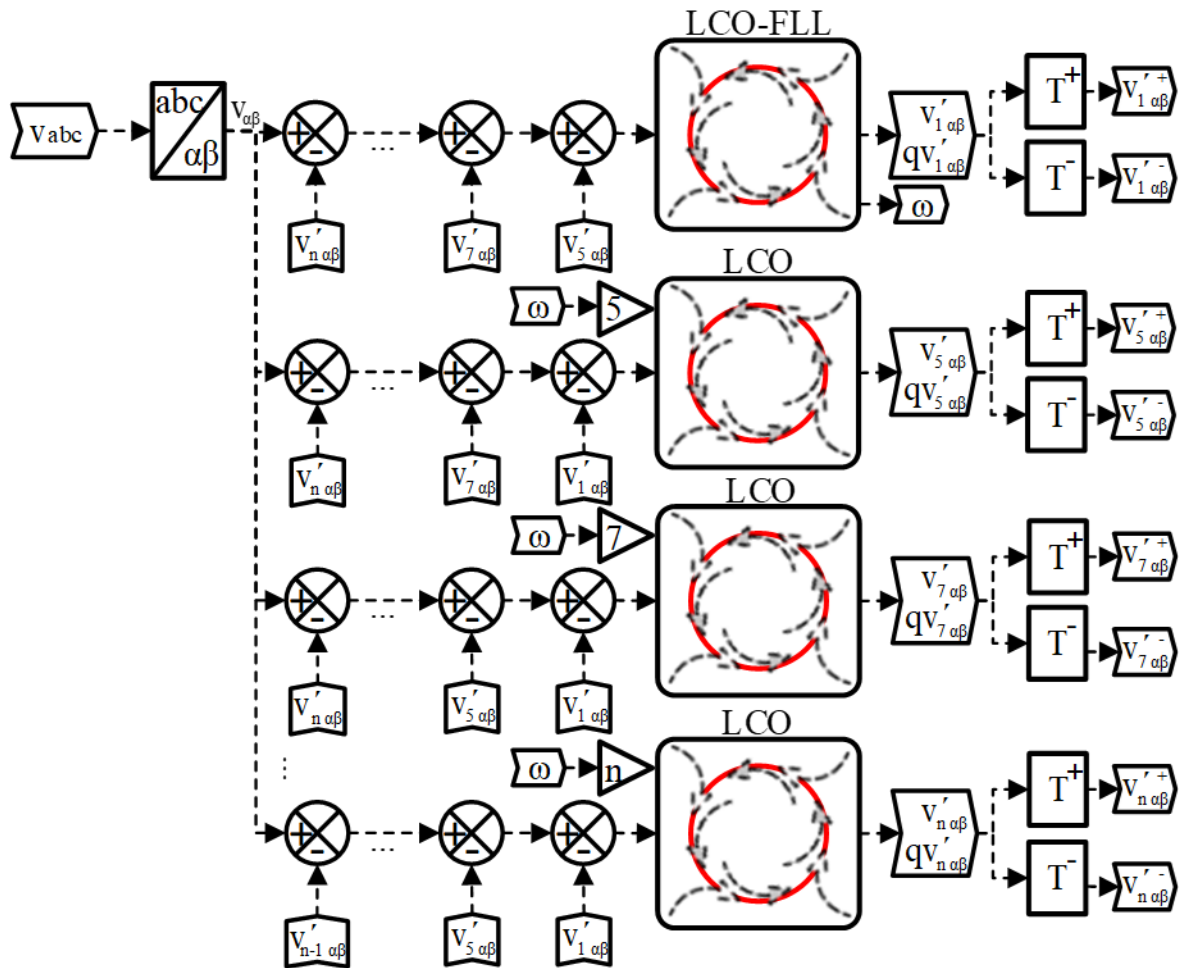


Figure 3.12. Block diagram of the three-phase Multi-LCO-FLL harmonics detection.

It can be seen in Figure 3.12 a master LCO-FLL at the top of the Figure, which is synchronized with the fundamental frequency of the reference. After that, there are n slaves synchronizers which are tuned to multiples of the fundamental frequency, i.e., if there exist the fifth harmonic in the input signal, the LCO slave with the frequency 5ω will

be synchronized with that harmonic and it will detect also the positive and negative sequence components of it. In this sense, the Figure 3.12 can be used to detect in voltage the different harmonics with their positive and negative sequence components of a nonlinear load, and then, inject in current that harmonics with their respective sequence components in order to diminish their effects in the grid.

3.8 Harmonic Detection Tests Simulation

The system from Figure 3.12 is tested with a disturbed input, which has the fifth harmonic with the positive sequence component with a magnitude of 0.2 p.u., and the seventh harmonic with the negative sequence component with a magnitude of 0.15 p.u. The system detects the sequence component of the fundamental frequency in less than 0.07 s, as it can be seen in Figure 3.13. Moreover, the system maintains the detection of positive sequence component even in a frequency shift of 10 Hz/s.

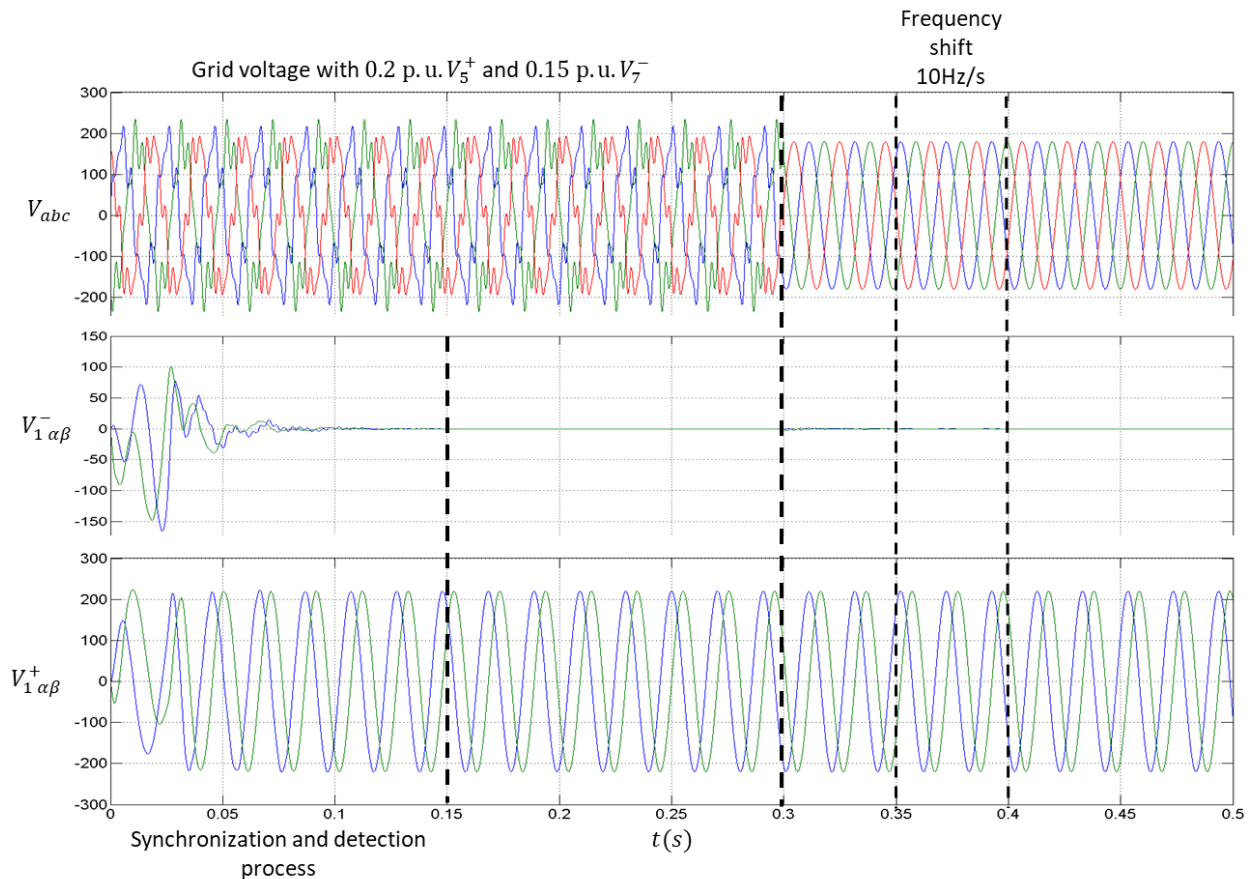


Figure 3.13. Detection of the sequence component of the fundamental frequency. V_{abc} Input signal. $V_{1\alpha\beta}^{-}$ Negative sequence component. $V_{1\alpha\beta}^{+}$ Positive sequence component.

Figure 3.14 depicts the detection of the fifth harmonic with its positive sequence component in less than 0.14 s. The disturbed input turns to an ideal sinusoidal input at 0.3 s, however, the system detects this change in the input signal in less than 0.04 s. Moreover, the system maintains the detection of positive sequence component of the fifth harmonic, even in a frequency shift of 10Hz/s.

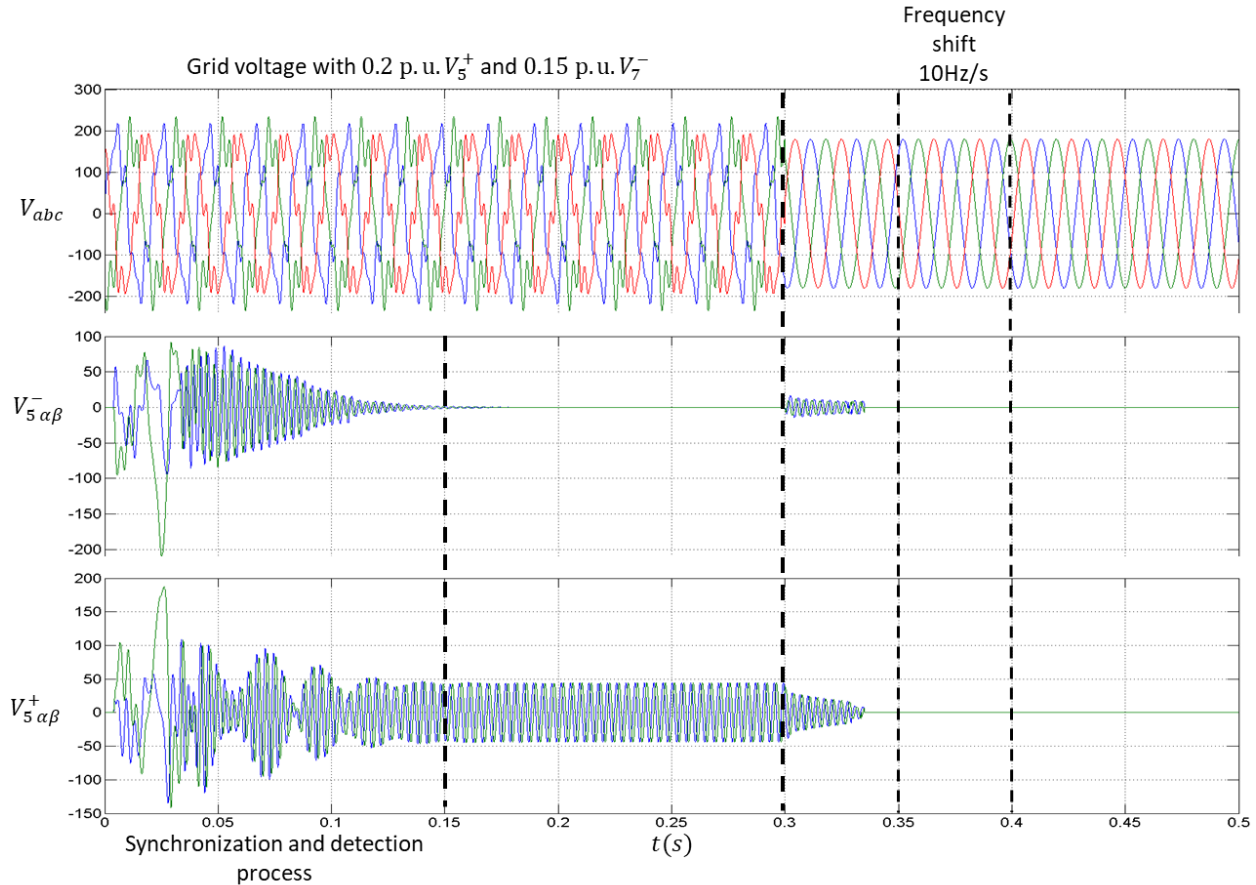


Figure 3.14. Detection of the sequence component of the fifth harmonic. V_{abc} Input signal. $V_{5\alpha\beta}^{-}$ Negative sequence component. $V_{5\alpha\beta}^{+}$ Positive sequence component.

Finally, it can be seen in Figure 3.15 the detection of the negative sequence component of the seventh harmonic in about 0.15 s. Furthermore, the system detects the absence of the seventh harmonic when the input signal turns into a signal without disturbance in 0.035 s approximately. A frequency shift is applied to the input signal, showing any disturbance in the detection of the seventh harmonic and its negative sequence component.

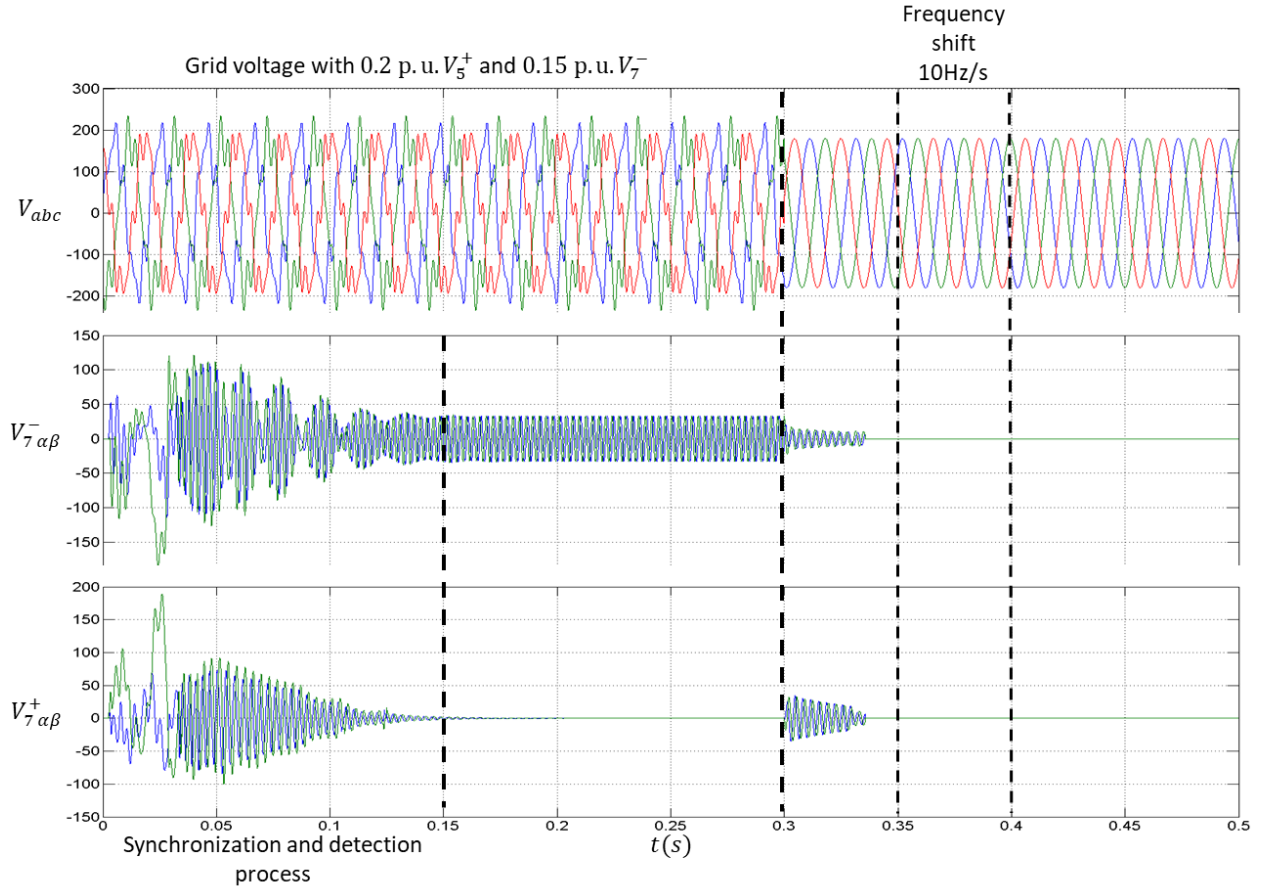


Figure 3.15. Detection of the sequence component of the seventh harmonic. V_{abc} Input signal. $V_{7\alpha\beta}^-$ Negative sequence component. $V_{7\alpha\beta}^+$ Positive sequence component.

3.9 Remarks on LCO-FLL

In essence, in this chapter, a new synchronization algorithm based on the concept of LCO for grid-connected converters is introduced. A stability analysis for the single LCO was depicted. Local stability analysis and numerical analysis confirms the stability of the interconnected LCO-FLL. The proposed method was compared with SOGI-FLL, ANF, and PLL based algorithms under optimized parameters for every system. Different tests were made, showing that the LCO-FLL provides suitable transients for initialization, frequency step, and phase jump tests, with better settling times than the compared systems. Harmonic rejection characteristics can be observed since the LCO-FLL reduces the THD from 20% to 5.5%, better than SOGI-FLL and ANF which reduce the THD to 7.2% and 9%

respectively. Moreover, the most important feature of the LCO-FLL is that produces synchronized signals with constant amplitude despite variations within the normal operation marked in IEEE 1547 Standard.

The three-phase LCO-FLL case was experimentally evaluated and it was demonstrated that the LCO-FLL is a suitable solution to accurately detect the fundamental-frequency positive and negative sequence components of the grid voltage, under highly distorted and unbalanced grid scenarios in less than a half grid voltage cycle. Another advantage of the LCO-FLL structure is that it is based on the estimation of the grid voltage frequency since the grid frequency variable is more robust than the voltage phase angle during transient faults. The LCO-FLL does not process any trigonometric function since any conventional voltage-controlled oscillator is used in its implementation. This feature contributes to reducing the time and computational resources.

4.

CURRENT CONTROL BASED ON LYAPUNOV THEORY AND LCO

Distributed Power Generation Systems (DPGSs), especially the grid-connected Photovoltaic (PV) systems have been a hot topic of high development and impact in the last decade. Power injection, with grid-connected PV systems, enhances the energy consumption efficiency and reduce the cost of energy consumption from the local loads [52], [53]. However, increasing the number of grid-connected PV systems in the utility network can lead to some problems, for instance, in the management and operation of the entire power grid. The main reason is that the power generation is not made in a centralized way, because the grid has more independent generators, most of them are intermittent due to weather conditions and faults, and then instability issues may occur [54].

In order to preserve a stable grid, in countries with a large penetration of grid-connected systems, stricter rules regarding the interconnection have been imposed [55]. Hence, a highly efficient control system of the grid-connected converter is mandatory in smart grid systems, especially for power management among the load, PV panels, and power network.

For instance, in [56]–[58] are proposed grid-connected PV-systems as a reactive power support in case of sags and swells on the grid voltage, as well as unbalanced voltage conditions. Moreover, in [59] fault current limiters are proposed in order to allow the PV-

system to operate under grid faults assuring grid sinusoidal currents. Other PV-systems have been developed with fault-ride-through capabilities in a grid-connected mode in order to compensate for unbalanced grid conditions and to provide reactive power in fault events [60]–[63], some of them, applying nonlinear controllers as fuzzy probabilistic wavelet neural network controller [64] and space vector Fourier transform concept [65]. In [5], [15], and [16], a PV system under grid fault is analyzed and it states the importance of a good operation even under these circumstances. However, in [66] a highly distorted current is obtained when the unsymmetrical grid fault occurs, not so for symmetrical. In [56], [67], other controllers for voltage unbalance fault is addressed, but no immunity to voltage harmonics is included.

It is of main concern the robustness of the DGPS [68], then riding-through grid voltage fault is necessary to consider it in PV systems, otherwise, a power outage may occur [68]. If the controller does not consider a robust synchronization system for unbalanced conditions, second-harmonic oscillations will be propagated into the system [69]. If a PV system is considered, also the maximum power point tracking (MPPT) should be affected. Grid-connected PV systems employ an MPPT algorithm [70], [71], this is because the power available depends on the environmental conditions. Additionally, in order to obtain the maximum power (MP), a constant power should be demanded, because even the current ripple deteriorate the power delivered [72], otherwise the operation at the MP is not completely assured. In this sense, although any standard [40], [73] set a limit in power quality or THD in current during voltage sags, is highly recommended to preserve the power quality, even with a certain magnitude and time duration of voltage sags [61].

In order to obtain an efficient grid-connected system, different works have been proposed. A flexible active power control for a grid-connected PV system during grid faults has been introduced in [41], where it has been proven that a DPGS can be very flexible power producer, that it is able to work in constant current, constant active power, or constant reactive power depending on the necessity. However, this scheme does not include the synchronization system.

Some advanced controllers as the Direct Lyapunov control (DLC) strategy have been proposed to regulate the active and reactive power changes, but also to compensate harmonic current components of nonlinear loads [43], [74], [75]. In [43] and [75] the PQ transformation and the inductor currents are considered for the controller design; however, the inverter input voltage is not considered into the controller. In [75] a

multilevel converter is considered, but the same type of current controller. A DLC is suggested in [74] for a single-phase converter, but again, only the output current is employed in the controller design. Therefore, the before mention control systems do not assure the stability for the inverter input voltage when it is combined with a MPPT algorithm, which it is strictly required in PV systems.

In addition to the current controller, a synchronization technique may be used. Some schemes are based on Phase Locked Loops (PLL) and Non-PLL methods [76]. One very popular Non-PLL synchronization scheme is the Second Order Generalized Integrator - Frequency Locked Loop (SOGI-FLL), which has been combined with wavelet transform (WT) and fuzzy logic controller (FLC). They provide good synchronization and an acceptable harmonic content [43], [77]–[81], however, they have the cost of solving a high number of control states. In [16] a Limit Cycle Oscillator (LCO) has been proposed for synchronization purpose with a high degree of immunity and robustness against perturbations. Moreover, it requires fewer equations to solve than PLLs and Non-PLL [76], helping to reduce the computation requirements.

However, the synchronizations techniques by itself only assure the operation under distorted voltage, and certainly, more elements are required for grid faults, but also to provide a constant power or constant current under unbalanced conditions.

In this Chapter, a current control strategy based on Lyapunov theory and an LCO is introduced. The proposed controller offers stability, a high degree of immunity and robustness against perturbation on the grid. Since the control law is based on the Lyapunov theory, the stability is assured, but also the controller considers the inverter input voltage as part of it. In this sense, the main contribution of this Chapter is a Lyapunov based controller that incorporates a dc-link voltage control loop, which permits to guarantee the stability of this voltage when it is in combination with a MPPT algorithm, making an important advantage versus other recent Lyapunov controllers [43], [74], [75].

The current reference generation is based on active power regulation and an LCO, therefore the proposal assures an efficient harmonic current rejection even under grid faults. Additionally, if constant power scheme is selected, the MPP of the PV panel may be effectively tracked even under unbalance conditions. Therefore, a stable and robust system against distorted and unbalanced conditions is obtained, but also assuring the good operation of the PV panel.

The Chapter is organized as follows. After the introduction, the active power strategies for DPGS are described in Section 4.1. Section 4.2 presents the Lyapunov

control law and its development for the full grid-connected PV system. Section 4.3 shows the complete controller for the power stage, which combines the past two sections with the LCO-FLL. Moreover, simulation and experimental test results are performed to demonstrate the efficiency and applicability of the proposal in Section 4.4 and 4.5. In Section 4.6, a comparison with other current control schemes is given. Finally, the conclusions are drawn in Section 4.7.

4.1 Active Power Strategies

Flexible active power strategies of DPGSs were proposed in [41] to generate the inverter current references. The main strategies deal with balanced injected currents and constant active power under unbalanced voltage faults. These two strategies are briefly explained below and linked to the outputs of the block diagram of Figure 3.5.

4.1.1 Balanced Injected Current Strategy

This strategy can be used when the injected currents are desired to be balanced, even in unbalanced voltage conditions, in this case, this scheme is employed. The currents are calculated by:

$$\mathbf{i}^* = G^+ \mathbf{v}^+, \quad (4.1a)$$

where \mathbf{v}^+ is the positive sequence voltage vector, and G^+ is the scalar conductance defined as:

$$G^+ = \frac{P_{ref}}{|\mathbf{v}^+|^2}, \quad (4.1b)$$

with P_{ref} as the desired active power, and $|\cdot|$ represents the vector module.

If the current vector (4.1a) is used as a reference, balanced positive-sequence sinusoidal waveforms are obtained, even under unbalanced voltage conditions. However, under the fault condition, the instantaneous active power (p) will oscillate around P_{ref} , this can be seen in the equation below:

$$p = \mathbf{v} \cdot \mathbf{i}^* = \underbrace{\mathbf{v}^+ \cdot \mathbf{i}^*}_p + \underbrace{\mathbf{v}^- \cdot \mathbf{i}^*}_{\tilde{p}}, \quad (4.2a)$$

where: \tilde{p} represents the power oscillation.

As it can be observed, there is an interaction between the injected current (positive-sequence) and the negative-sequence of the grid voltage. Then, the reactive power will also oscillate at twice of the fundamental grid frequency [41]:

$$q = |\mathbf{v} \times \mathbf{i}^*| = \underbrace{|\mathbf{v}^+ \times \mathbf{i}^*|}_0 + \underbrace{|\mathbf{v}^- \times \mathbf{i}^*|}_{\tilde{q}}, \quad (4.2b)$$

where: \tilde{q} represents the reactive power oscillation.

When a PV panel is operated, it is desirable that the active power is kept constant in order to assure the MPPT, as it was mentioned before; then, this technique should not be the best for it.

4.1.2 Constant Active Power Strategy

This strategy can be used when the active power P_{ref} is desired to be constant, even in an unbalanced grid voltage. This should be the case with PV panels, in order to assure the MPPT. To achieve it, the following constraints are imposed in the current reference calculation:

$$\mathbf{v}^+ \cdot \mathbf{i}^{*+} + \mathbf{v}^- \cdot \mathbf{i}^{*-} = P_{ref}, \quad (4.3a)$$

$$\mathbf{v}^+ \cdot \mathbf{i}^{*-} + \mathbf{v}^- \cdot \mathbf{i}^{*+} = 0. \quad (4.3b)$$

Therefore, the current reference becomes [41]:

$$\mathbf{i}^* = g^\pm(\mathbf{v}^+ - \mathbf{v}^-). \quad (4.4a)$$

Where g^\pm is the scalar conductance defined as:

$$g^{\pm} = \frac{P_{ref}}{|v^+|^2 - |v^-|^2}. \quad (4.4b)$$

In this case, the reactive power delivered to the grid shows oscillations at twice the fundamental frequency because the injected current vector and the grid voltage vector have different directions [41].

Any of these two strategies can be linked with the outputs of the block diagram of Figure 3.5. Then, a proper current reference may be provided to the Lyapunov control law given below. By making this, it is obtained a robust controller against harmonics, phase-frequency shifts, voltage unbalance, and also the MPP of the PV panel can be fully assured even under unbalance condition if constant power is selected.

4.2 Lyapunov Control Law

A Lyapunov function is considered in order to bring the current vectors to the values indicated in (4.1a) or (4.4a). Moreover, the input voltage v_{dc} is considered into the controller; this permits to assure the stability of this variable when it is used the MPPT algorithm. This extra loop was not included in other schemes, then the stability was not assured for this voltage.

An MPPT scheme with a double power stage may be employed; this is, a dc/dc boost converter should be used to get the MPP, and then, an inverter coupled to the grid with the respective L filter (and its parasite resistance R_L). The schematic diagram of the whole system model is shown in Figure 4.1. Where i_L is the current in the inductor L_1 , v_{dc} is the voltage in the capacitor C_{out} , and i_{inv} is the current drained to the inverter. This part of the system is controlled by the switch S , in order to ensure the power transfer from the PV to the grid with the maximum power. This goal is reached using an MPPT based on the traditional Perturb and Observe (P&O) method, which is an easy and efficient slow control loop in order to guarantee a low error at steady state [71]. P&O method might introduce low frequency oscillations in the v_{dc} if the measure step is quite large in comparison with perturbations in the grid.

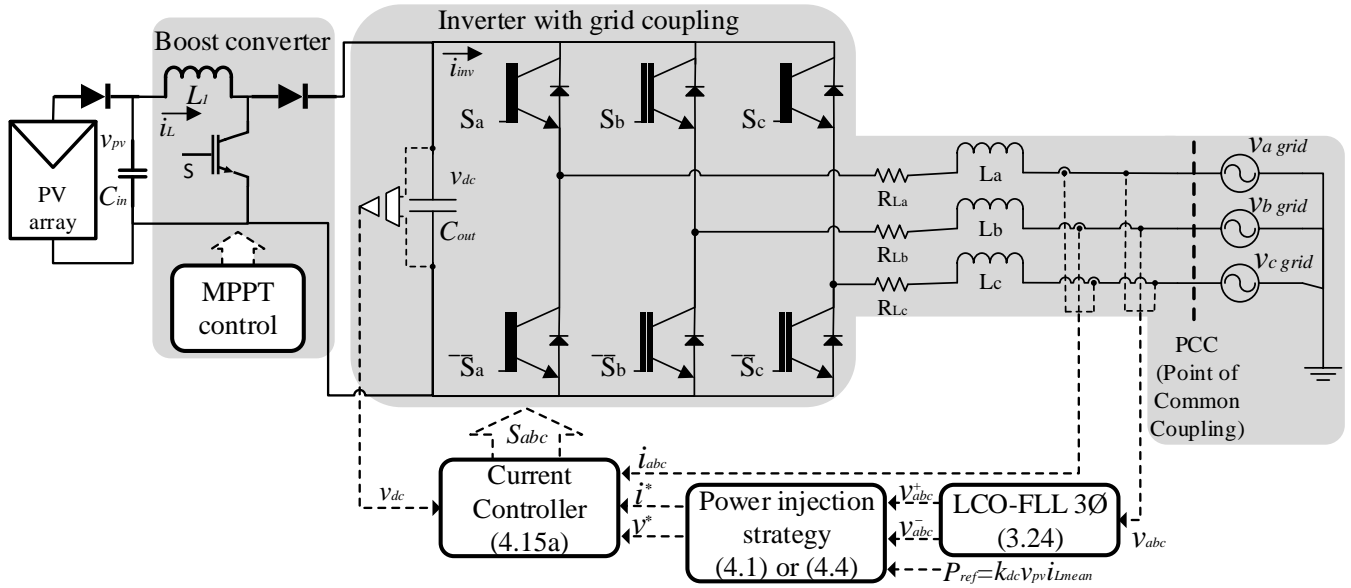


Figure 4.1. PV-Grid connected system with the current injection control system.

In this stage, it is important to define the power P_{ref} in the conductance (4.1b) and (4.4b) as:

$$P_{ref} = k_{dc} v_{pv} i_{Lmean} , \quad (4.5)$$

where i_{Lmean} is the mean current of i_L , v_{pv} is the voltage in C_{in} , and k_{dc} is a variable with information of v_{dc} . The variable k_{dc} regulates the bus voltage in v_{dc} , which will be defined in the following section.

Grid-Connected Inverter

The inverter stage consists of a three-phase grid-connected system for current injection. The dc/dc boost converter voltage (v_{dc}) is not regulated for the first stage, because is used only to track the maximum power available. Therefore, a voltage loop is included in the controller to assure its stability by injecting the proper value of active power P_{ref} (4.5) to do it. The dynamic equations of the inverter coupled to the utility grid can be written as:

$$\begin{bmatrix} \dot{i}_a \\ \dot{i}_b \\ \dot{i}_c \end{bmatrix} = \frac{1}{2} v_{dc} \mathbf{Q}^{-1} \begin{bmatrix} U_a \\ U_b \\ U_c \end{bmatrix} - \frac{1}{g} \mathbf{Q}^{-1} \begin{bmatrix} i_a \\ i_b \\ i_c \end{bmatrix} - \mathbf{R}_L \mathbf{Q}^{-1} \begin{bmatrix} i_a \\ i_b \\ i_c \end{bmatrix}, \quad (4.6)$$

where U is the control law, i is the injected current of the inverter, v_{dc} is the dc-link voltage, g is the conductance ($g = i_j/v_j$), $j = a, b, c$;

$$\mathbf{Q}^{-1} = \begin{pmatrix} 1/L_a & 0 & 0 \\ 0 & 1/L_b & 0 \\ 0 & 0 & 1/L_c \end{pmatrix}, \quad (4.7)$$

$$\mathbf{R}_L = \begin{pmatrix} R_{La} & 0 & 0 \\ 0 & R_{Lb} & 0 \\ 0 & 0 & R_{Lc} \end{pmatrix}. \quad (4.8)$$

The equilibrium point of (4.6) is determined by:

$$i_j^* = \frac{g v_{dc} U_j^*}{2(R_{Lj}g+1)}; j = a, b, c, \quad (4.9)$$

where R_{Lj} is the parasite resistance known previously by the cables from the inverter to the PCC, and U_j^* is the value of the control law. In this stage, it can be set (4.6) around the origin with the next error variables:

$$z_j = i_j - i_j^*; w_j = U_j - U_j^*; j = a, b, c. \quad (4.10)$$

Now, it can be rewritten (4.6) as:

$$\dot{\mathbf{z}} = \frac{1}{2} v_{dc} \mathbf{Q}^{-1} [\mathbf{w} + \mathbf{U}^*] - \left[\left(\frac{1}{g} \mathbf{I} + \mathbf{R}_L \right) \mathbf{Q}^{-1} \right] [\mathbf{z} + \mathbf{i}^*], \quad (4.11)$$

where \mathbf{I} is a 3x3 identity matrix,

$$\mathbf{z} = [z_a \quad z_b \quad z_c]^T, \quad (4.12a)$$

$$\mathbf{w} = [w_a \quad w_b \quad w_c]^T, \quad (4.12b)$$

$$\mathbf{U}^* = [U_a^* \quad U_b^* \quad U_c^*]^T, \quad (4.12c)$$

$$\mathbf{i}^* = [i_a^* \quad i_b^* \quad i_c^*]^T. \quad (4.12d)$$

Now, a Lyapunov function is constructed with the injected current errors \mathbf{z} , and the error between values related with dc-link voltage $v_{dc}/\sqrt{6}$ and the rms value of the grid voltage V_r as:

$$V_L = \frac{1}{2} \mathbf{z}^T \mathbf{Q} \mathbf{z} + \frac{1}{2} \left(\frac{v_{dc}}{\sqrt{6}} - V_r \right)^2. \quad (4.13)$$

In order to get the equilibrium point (4.9) from (4.11), the errors stated in (4.13) as a Lyapunov function, must be diminishing. In other words, (4.13) must be a decreasing function and therefore, its derivative must be negative. In this sense, the derivative of (4.13) is written as:

$$\dot{V}_L = \frac{1}{2} \left\{ v_{dc} z_j (w_j + U_j^*) - 2z_j (z_j + i_j^*) \left(\frac{1}{g} + R_{Lj} \right) \right\} + \left(\frac{v_{dc}}{\sqrt{6}} - V_r \right) \left(-\frac{v_j^2}{2TV_{jr}} \right);$$

$$j = a, b, c, \quad (4.14)$$

where T is the fundamental period. Now, in order to make negative the first term of (4.14), the next control law is proposed:

$$U_j = -(i_j - gv_j^*) + \frac{2v_j^*}{v_{dc}} (R_{Lj}g + 1); j = a, b, c; \quad (4.15a)$$

where i_j are the currents sensed in the PCC, and v_j^* are the voltage signals to track. In this case, v_j^* are the positive-sequence voltage signal obtained in (3.24a) from Figure 3.5, i.e.:

$$[v_a^* \quad v_b^* \quad v_c^*]^T = \mathbf{v}^* = \mathbf{v}^+ = \mathbf{v}_{abc}^+. \quad (4.15b)$$

Moreover, it can be seen that the second term of (4.14) can be made negative ensuring that:

$$\frac{v_{dc}}{\sqrt{6}} > V_r. \quad (4.15c)$$

In this sense, in order to ensure the inequality (4.15c), k_{dc} from (4.5) is defined as follows:

$$k_{dc} = 1 - \left(k_p + k_i \frac{1}{s} \right) e_{dc}, \quad (4.15d)$$

where k_p and k_i are the proportional, integral controller gains, and e_{dc} is the voltage error, defined as:

$$e_{dc} = V_{ref} - v_{dc}, \quad (4.15e)$$

where V_{ref} must be higher than $\sqrt{6}V_{jr}$, according to (4.15c). Then, substituting (4.15a) into (4.10) and (4.14), the following is obtained:

$$\dot{V}_L = -\frac{1}{2} \left\{ z_j^2 \left[v_{dc} + 2 \left(\frac{1}{g} + R_{Lj} \right) \right] \right\} - \left(\frac{v_{dc}}{\sqrt{6}} - V_{jr} \right) \left(\frac{v_j^2}{2TV_{jr}} \right); j = a, b, c. \quad (4.16)$$

It can be seen from (4.16) that its first term is negative due to the control law (4.15a). Moreover, it can be seen that its second term is also negative, just if the inequality (4.15c) is ensured. This inequality is ensured by the modulating variable k_{dc} that regulates the injected power in (4.5), according to the desired dc-link voltage v_{dc} stated in (4.15e).

Hence, (4.14) is negative and the Lyapunov function (4.13) is a decreasing function that diminishes the current and v_{dc} errors. Therefore, the equilibrium point (4.9) is called that it is asymptotically stable in the Lyapunov sense [82], applying the control law (4.15a) and the modulating variable k_{dc} to (4.5). Moreover, it is also assured the stability of v_{dc} when an MPPT is considered, which is an indispensable element for a PV system.

4.3 Current Control for the Inverter-Grid Connected System

Figure 4.1 shows the controller of the inverter connected to the grid. This control scheme is based on three main parts, the synchronization technique (LCO-FLL), the power injection strategy or current reference generation, and the new control law developed by a Lyapunov function.

The three-phase synchronization block, composed by the LCO-FLL (3.24), takes as input, the grid voltages vector v_{abc} in order to generate the positive v_{abc}^+ and negative v_{abc}^- sequence components, which, together with the measured injected current i_{abc} and the dc-link voltage v_{dc} , are the inputs of the current controller block.

The current controller block in Figure 4.1 has the control law (4.15a), but it can be selected as the Balanced Injected Currents (BIC) strategy (4.1) or the Constant Active Power (CAP) strategy (4.4). This is obtained by substituting the conductance $g = i_j^*/v_j^*$ in (4.15a) and using the desired calculated currents i^* (4.1a) or (4.4a) with their respective scalar conductance G^+ (4.1b) or g^\pm (4.4b). However, for PV systems is suggested to use CAP scheme to assure the MPP even under unbalanced grid voltage conditions.

It is important to note that this current control scheme needs to solve just the differential equations of the two LCO-FLL blocks (Figure 3.5) and also the one for the dc voltage v_{dc} , therefore, only seven dynamic states are solved. This feature contributes to reducing the time and computational resources in the current control implementation, in comparison with other current controllers that need to solve between 12 and 26 dynamic states [43], [80], [81].

4.4 Simulation Results

Simulation tests of the system in Figure 4.1 are developed in MATLAB-SIMULINK in order to validate the high performance of the current control for the Voltage Source Converter (VSC) as the interfacing block between the PV panel and the dc/dc boost converter with the grid. It was used the SimPowerSystem library, with the Dormand-Prince Solver (ode45), and a relative tolerance of 1^{-3} . The system was simulated with the model parameters shown in Table IV.1. In this table, the values of the electric parameters as the inductance L_{abc} , parasite resistance R_{Labc} , and the fundamental and switching frequency are shown. Moreover, details about the AC source and the PV array simulator, sensors and type of fault used are depicted. Finally, the MPP and v_{dc} with their respective Short-circuit Current I_{sc} , and Open-circuit Voltage V_{oc} reached in simulation and experimental test are given.

The Figures 4.2 and 4.3 show the simulation results for the proposed current control under BIC and CAP strategies respectively. The Figures 4.2 (a) and 4.3 (a) show the grid voltage under an unbalanced fault type C with 50% of voltage sag started in $t = 0.25$ s (dashed line); which is a symmetrical unbalance. In $t = 0.02$ s, the current control was turned on and the current is injected to the balanced grid during $0.02 < t(s) < 0.25$; as it can be seen, the control law signal, and the current is balanced and correspond with an active power of 1kW (Figures 4.2b-c-d and 4.3b-c-d).

TABLE IV.I
SIMULATION AND EXPERIMENTAL MODEL PARAMETERS

Parameter	Value
<i>Inductance (L_{abc})</i>	<i>7mH</i>
<i>Parasite resistance (R_{Labc})</i>	<i>1Ω</i>
<i>Fund. and Switching freq.</i>	<i>60Hz, 22kHz</i>
<i>AC power source</i>	<i>Chroma 61700</i>
<i>IGBT module</i>	<i>CM75DU-12H Powerex</i>
<i>Voltage and current sensor</i>	<i>LV25-P, LA 55-P/SP1 LEM</i>
<i>Grid voltage ($V_{abc\ grid}$)</i>	<i>110Vrms</i>
<i>Sag type C*</i>	<i>$V_a=110 \angle 0^\circ$, $V_b=55 \angle 140^\circ$, $V_c=55 \angle 220^\circ$</i>
<i>PV array simulator</i>	<i>N8937APV Agilent (15kW DC)</i>
<i>Short-circuit current (I_{sc})</i>	<i>7.34A (Sim), 3.25A (Exp)</i>
<i>Open-circuit voltage (V_{oc})</i>	<i>180V (Sim), 180V (Exp)</i>
<i>MPP, v_{dc}</i>	<i>1.2kW, ~500V (Sim), 550W, ~400V (Exp)</i>

* V_b , $V_c = 97V$ (15% of voltage sag) in experimental tests with 8.55% of unbalance, which it is categorized as a fault according to EN 50160, UL 1741, and IEEE 1547.

After that, when the system is under BIC strategy, the VSC injects balanced currents to the unbalanced grid during $0.25 < t(s) < 0.3$, producing an amplitude decrease of the control law signals, which is depicted in Figure 4.2 (b). Moreover, the current remains perfectly balanced even during the voltage fault, as it can be observed in Figure 4.2 (c) and 4.2 (d). However, the active and reactive power show oscillations around 1kW and 0VAr respectively, at twice of the fundamental frequency.

Nevertheless, when the system is operated under CAP strategy, unbalanced control law signals are produced (See Figure 4.3 (b)). Moreover, during the fault $0.25 < t(s) < 0.3$, the injected current is unbalanced in order to compensate the grid voltage unbalance and to keep almost constant the injected active power to the grid, as it can be seen in Figures 4.3 (c) and 4.3 (d).

Furthermore, in Figures 4.2 (e) and 4.3 (e), is depicted the effect of BIC and CAP strategies in the dc-link voltage v_{dc} , PV voltage v_{pv} , and PV current i_{pv} . It can be seen that the dc-link voltage has a better regulation with CAP strategy than with BIC, under fault conditions. In this sense, CAP strategy ensures a constant active power injection to the grid, that permits a better tracking of the MPP of the PV panel without the need of a large capacitor.

Finally, the Lyapunov function V_L under BIC and CAP is depicted in Figures 4.2 (f) and 4.3 (f), respectively. It can be seen that V_L remains positive, even during grid fault conditions, showing the stability of the current injection system under both active power strategies.

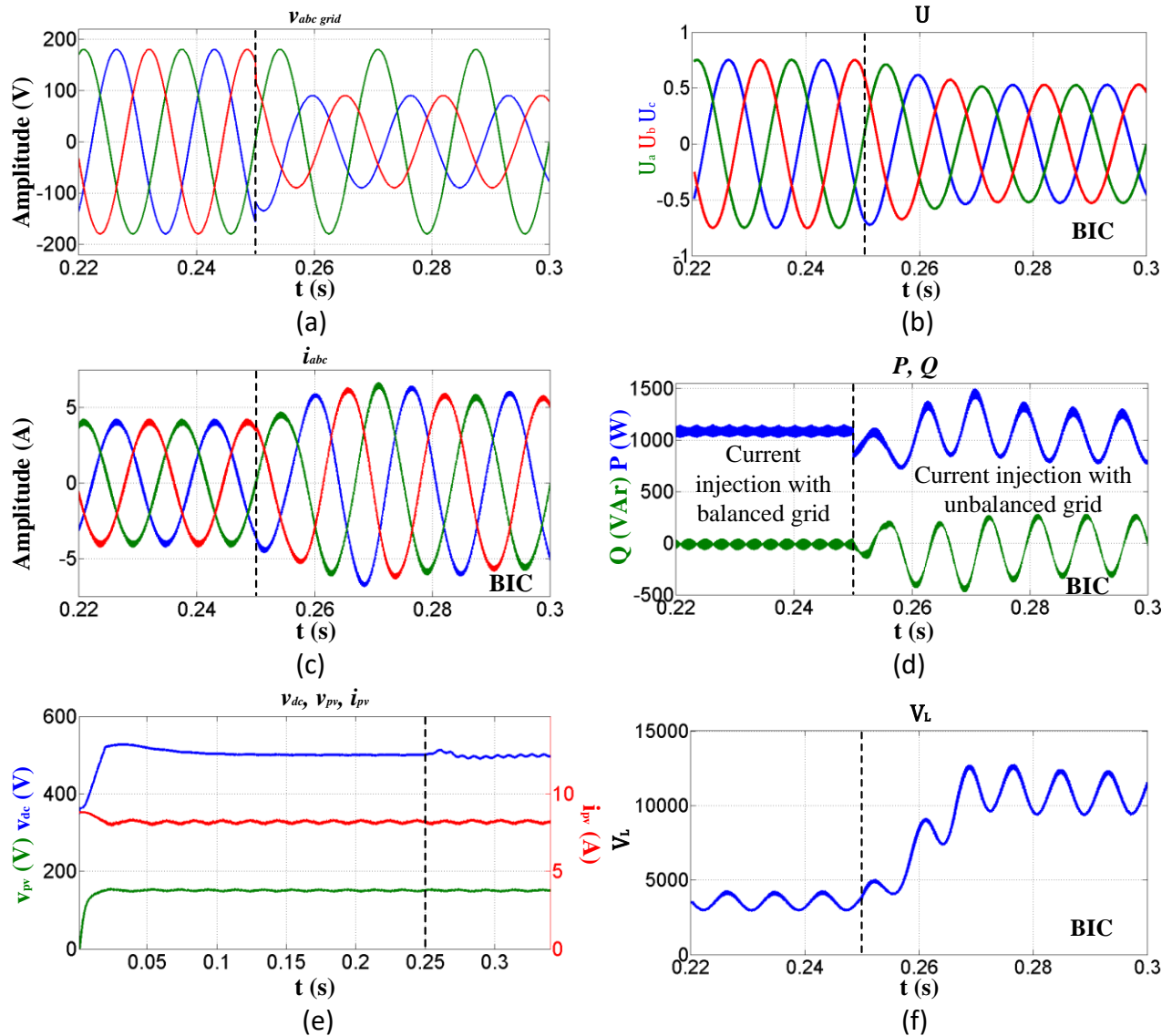


Figure 4.2. Simulation test results for the current control system under BIC strategy. (a) Grid voltages. (b) Control law U under BIC. (c) Injected inverter current to grid under BIC. (d) Active and reactive power under BIC. (e) dc-link voltage v_{dc} , PV voltage v_{pv} , and PV current i_{pv} . (f) Lyapunov function V_L .

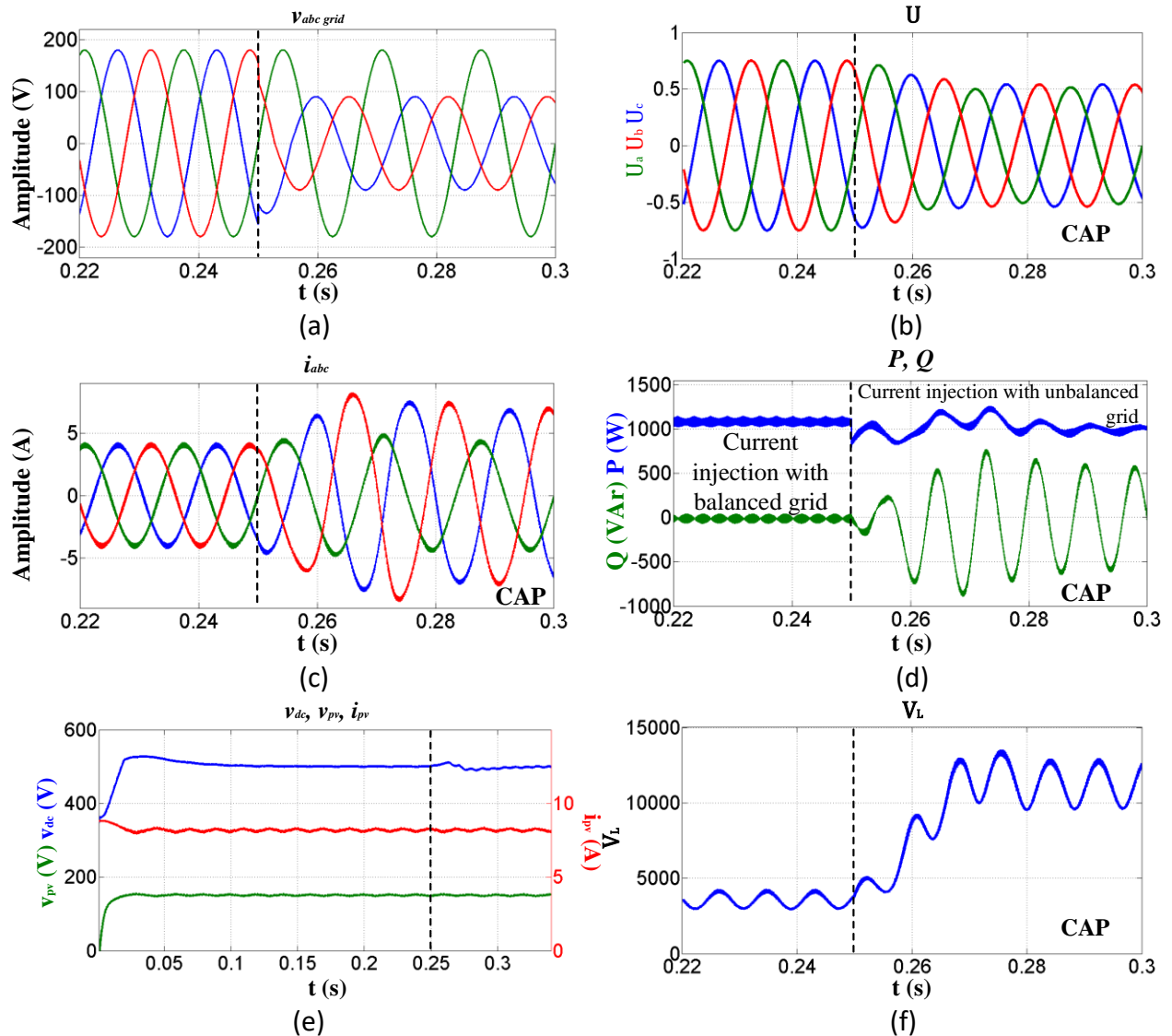


Figure 4.3. Simulation test results for the current control system under CAP strategy. (a) Grid voltages. (b) Control law U under CAP. (c) Injected inverter current to grid under CAP. (d) Active and reactive power under CAP. (e) dc-link voltage v_{dc} , PV voltage v_{pv} , and PV current i_{pv} . (f) Lyapunov function V_L .

4.5 Experimental Test Results

Experimental tests of the system in Figure 4.1 are shown below in order to verify the high performance of the current control. The parameters of the experimental setup are listed in Table IV.I. In this sense, a power supply operated as PV array simulator is

employed (N8937APV of Agilent). The programmable ac power source Chroma 61700 emulates the utility grid. Due to the limitation of the ac power source to receive power, a resistive load is connected to the right side of the PCC in Figure 4.1. The system controller was implemented in a Single Board of National Instruments based on an FPGA Xilinx Spartan-6 LX45 at 2.5 MHz, and the PWM was implemented with a 22kHz carrier frequency. The experimental setup and the technical specifications are shown in the Appendix 9.2.

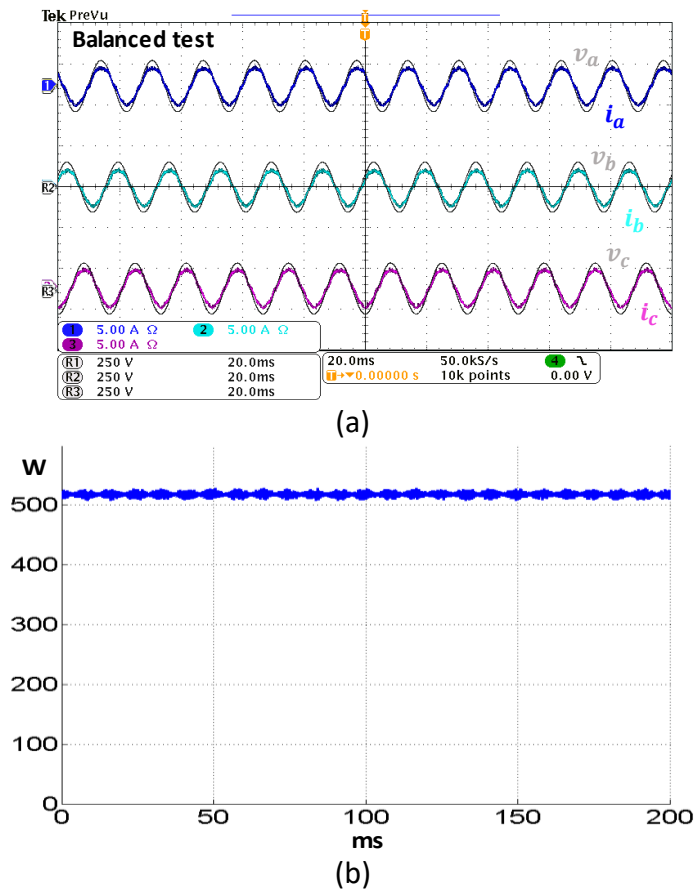


Figure 4.4. Three-phase balanced voltage test under BIC strategy. (a) Three-phase voltage, R1, R2, R3 (250 V/div, 20 ms/div), and three-phase currents (5 A/div, 20 ms/div). (b) Active power injected to the grid (100 W/div, 50 ms/div).

Steady state test. A test of current injection at steady state to a balanced grid was made with the control law (4.15a), no matter which power strategy is selected (BIC or CAP), the injected current looks the same. Figure 4.4 (a) shows the balanced grid voltage and the synchronized sinusoidal injected current. The current THD obtained is 3.5%; the

total constant active power is depicted in Figure 4.4 (b) (around 500W). It is important to mention that the injected currents are in function of i_{inv} which is limited by the MPP of the PV array. However, if the fault is excessive and the physical operation limits of the inverter are exceeded, certainly the system should be shut down by protection purposes, according to actual valid Standards as EN 50160, UL 1741, and IEEE 1547.

Unbalanced tests. Figure 4.5 shows the test under the BIC strategy. A voltage fault type C in the grid occurs in the middle of the graph. In this case, sinusoidal balanced currents are injected into the balanced and unbalanced grid (Figure 4.5 (a)), the current THD for the unbalance condition is also 3.5%. In Figure 4.5 (b) can be observed that there are oscillations at double the grid frequency in the instantaneous active power around 400W, which is in full agreement with the theory.

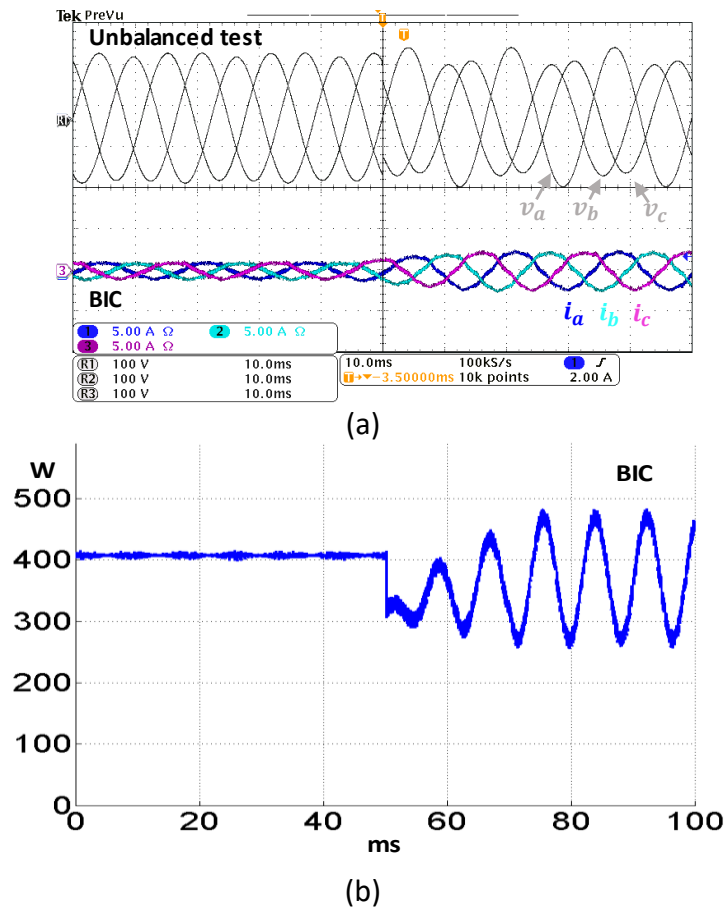


Figure 4.5. Three-phase unbalanced voltage step change test under BIC strategy. (a) Three-phase voltage with sag type C step change, R1, R2, R3 (100 V/div, 10 ms/div), and three-phase balanced currents (5 A/div, 10 ms/div). (b) Active power injected to the grid (100 W/div, 20 ms/div).

The results for the system under CAP strategy are depicted in Figure 4.6, also a grid fault Type C was tested. In this strategy, the current controller injects negative sequence current to the unbalanced grid in order to compensate the oscillations in the instantaneous active power. This is reflected in unbalanced sinusoidal currents with a small increment in the current THD of 4% (Figure 4.6 (a)). As it can be observed, an instantaneous constant active power of 400W is obtained (Figure 4.6 (b)). In all of these cases, the dc voltage v_{dc} was regulated at 400V, that is, the capacitor voltage is stabilized properly by the proposed scheme. Moreover, if the CAP strategy is used, then the MPP is perfectly tracked, and therefore a size reduced capacitor may be employed. This extra loop and the active power strategy is an advantage in comparison with other Lyapunov controllers as [43], [74], [75], [83].

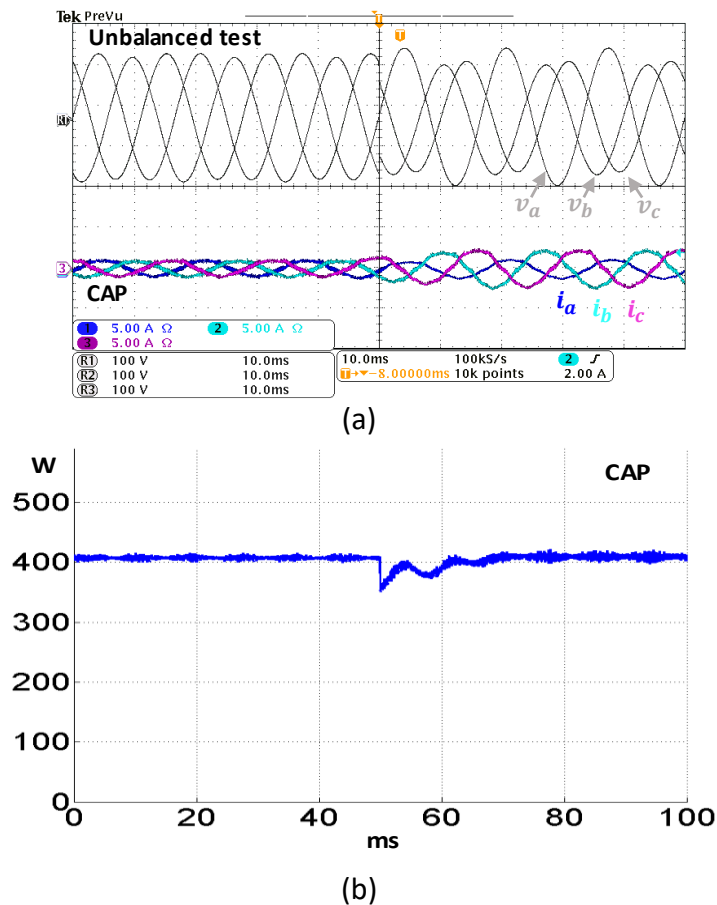


Figure 4.6. Three-phase unbalanced voltage step change test under CAP strategy. (a) Three-phase voltage with sag type C step change, R1, R2, R3 (100 V/div, 10 ms/div), and three-phase unbalanced currents (5 A/div, 10 ms/div). (b) Constant active power injected to the grid (100 W/div, 20 ms/div).

Distortion test. In Figure 4.7 is shown the performance of the system under a distorted voltage with 9% of THD. It is important to highlight that the harmonic current rejection against contamination in the voltage utility grid is due to the synchronization block LCO-FLL. Moreover, it can be seen that the injected current is sinusoidal with a THD less than 3.5% in distortion grid conditions.

With these performed tests, the operation of the proposed system is illustrated. As it can be observed, the proposal offers a high degree of immunity and robustness against perturbation on the grid.

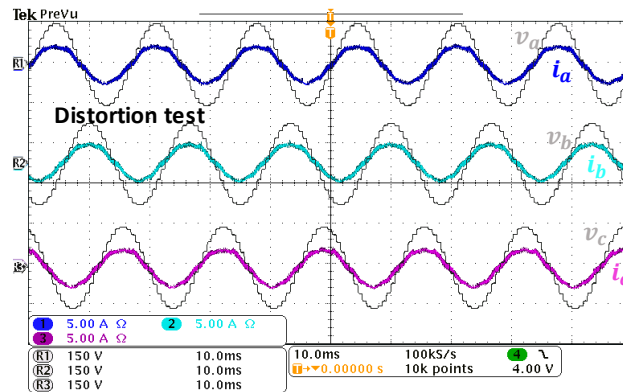


Figure 4.7. Robustness of the injected current versus voltage harmonics components with THD of 9%. Three-phase distorted voltage, R1, R2, R3 (150 V/div, 10 ms/div), and three-phase balanced currents (5 A/div, 10 ms/div).

4.6 Comparison with other schemes

In order to evaluate and to contrast the dc-link specifications and ac characteristics of the proposed controller, a comparison summary of the most representative actual current controllers for grid-connected PV systems is given in Table IV.II. Different controllers are assessed, as the Direct Lyapunov Control (DLC) [43], Fuzzy Probabilistic Wavelet Neural Network (FPWNN) control [64], the Space Vector Fourier Transform (SVFT) control [65], a Proportional Integral – Proportional Resonant control [63], a control to Minimize Peak Currents During Unbalanced Grid (MPCDUG) [61], and a control to Enable Current Limitation Under Unbalanced Faults (ECLUUF) [56].

As it can be seen in Table IV.II, the current controllers apply an MPPT algorithm to get the MPP from the PV panel and to regulate the v_{dc} . However, the SVFT, MPCDUG,

and DLC do not consider a dc-link control, and the v_{pv} and v_{dc} are not regulated by their respective controller. It is important to mention that the actual Lyapunov based controllers [43], [74], [75] are not suitable for PV systems because they do not consider an MPPT and a v_{dc} control loop. In this sense, the contribution of this Chapter is a Lyapunov based controller that incorporates a v_{dc} control loop to warranty its stability.

Furthermore, most of the compared controllers are designed for three-phase systems and all of them are able to still working with sags and unbalance events accomplishing low voltage ride through (LVRT) codes, except the DLC. According to the experimental test of the different controllers for disturbance events, the proposed Lyapunov-LCO controller has an acceptable settling time of 25 ms in contrast with the others controllers, which have settling times between 30-200 ms. Moreover, due to the synchronization system of the proposed control, the current THD_i is relatively smaller than the compared controllers, making this, an important contribution for grid-connected PV systems controllers.

TABLE IV.II
COMPARISON SUMMARY OF DIFFERENT CURRENT CONTROLLERS FOR GRID CONNECTED PV SYSTEMS

	Proposed Lyapunov-LCO	DLC ^a	FPWNN ^b	SVFT ^c	PI-PR ^d	MPCDUG ^e	ECLUUF ^f
dc-link specifications							
<i>MPPT algorithm</i>	<i>P&O</i>	<i>Constant V_{dc} is considered</i>	<i>P&O with mode I and II</i>	<i>Constant V_{pv} is considered</i>	<i>Modified Incremental Conductance</i>	<i>Constant V_{dc} is considered</i>	<i>Hill-climbing method combined with non-MPPT</i>
<i>v_{dc} control loop</i>	<i>yes</i>	<i>no</i>	<i>yes</i>	<i>no</i>	<i>yes</i>	<i>no</i>	<i>yes</i>
ac characteristics							
<i>Grid type</i>	<i>Three-phase</i>	<i>Three-phase</i>	<i>Three-phase</i>	<i>Three-phase</i>	<i>Single-phase</i>	<i>Three-phase</i>	<i>Three-phase</i>
<i>Fault ride through capability</i>	<i>yes</i>	<i>no</i>	<i>yes (under LVRT^b)</i>	<i>yes</i>	<i>yes</i>	<i>yes</i>	<i>yes (under LVRT^b)</i>
<i>Settling time (2% error)</i>	<i>≈ 25 ms @50% sag in V_b</i>	<i>≈ 30 ms @Variation on local load</i>	<i>≈ 200 ms @50% sag in V_{abc}</i>	<i>≈ 16 ms @15% sag in V_b, V_c</i>	<i>≈ 90 ms @40% sag</i>	<i>≈ 30 ms @32% sag in V_b, V_c</i>	<i>≈ 50 ms @37% sag in V_b, V_c</i>
<i>Synchronization system</i>	<i>yes</i>	<i>no</i>	<i>no</i>	<i>no</i>	<i>yes</i>	<i>no</i>	<i>no</i>
<i>THD_i</i>	<i>3.5% ^g</i>	<i>≈ 5%</i>	<i>≈ 8%</i>	<i>≈ 17%</i>	<i><2%</i>	<i>16%</i>	<i>≈4.3%</i>

^a Direct Lyapunov Control [43]; ^b Fuzzy Probabilistic Wavelet Neural Network control [64]; ^c Space Vector Fourier Transform control [65]; ^d Proportional Integral – Proportional Resonant control [63]; ^e Minimizing Peak Currents During Unbalanced Grid control [61]; ^f Enabling Current Limitation Under Unbalanced Faults control [56]; ^g THD_v input = 9%; ^h Low Voltage Ride Through.

4.7 Remarks on Current Control

This Chapter proposes a novel current controller based on a Lyapunov control law and a Limit Cycle Oscillator. The proposed scheme is also combined with power

management strategies as the Balanced Injected Currents (BIC) and the Constant Active Power (CAP) strategy, in order to inject balanced currents or constant active power, even in fault conditions, depending on the user requirements. However, the CAP strategy has been suggested for grid-connected PV systems. This is because the maximum power point tracking can be assured even in an unbalanced grid voltage, and the capacitor size may be reduced.

The main contribution of this Chapter is a Lyapunov based controller that incorporates a dc-link voltage control loop v_{dc} , which permits to guarantee the stability of this voltage, making an important advantage versus other recent Lyapunov controllers [43], [74], [75]. Additionally, the proposed scheme was compared with other actual current controllers for grid-connected PV system, showing an efficient harmonic current rejection with 3.5% of THD_i, and better settling times than the compared current schemes [56], [61], [63]–[65]. Moreover, the proposed controller needs to solve only seven dynamic states over other current controllers that need to solve between 12 and 26 dynamic states [43], [80], [81]. Finally, the stability and performance of the proposed system have been validated through simulation and experimental results.

5.

MODIFIED SANDIA VOLTAGE SHIFT ANTI-ISLANDING TECHNIQUE

In the previous Chapters, a current control based on Lyapunov Theory and LCO has been developed in order to attack disturbances such as impulsive and oscillatory transients, voltage and frequency fluctuations, high-frequency electrical noise, harmonic distortion, and imbalance in three-phase systems. However, disturbances as long duration interruptions cannot be managed by this control. That is why the necessity to develop a system capable to detect this kind of problem and to handle it in a proper way, as it can be seen in Figure 5.1.

Renewable energies, especially, photovoltaic (PV) systems are gaining relevance rapidly in the green energies, as nations promote public policies in order to reduce greenhouse gas emissions from traditional power plants [84]. Particularly, the increased penetration level of PV-Grid connected systems yields certain problems in power quality and safety, some of them are voltage and frequency disturbances, flickering, waveform distortion, and islanding conditions [85]. Among all these problems related to PV-Grid connected systems, unintentional islanding is one of the most important hazards in safety issues.

In electric topics, “islanding” is an electrical phenomenon, which occurs when the electric energy supplied by the power network is interrupted, but the Distributed Power Generation Systems (DPGS) is still supplying energy to the loads [73]. Therefore, this

condition of energized electric lines in an expected disconnected part of the electric network is a serious safety hazard.

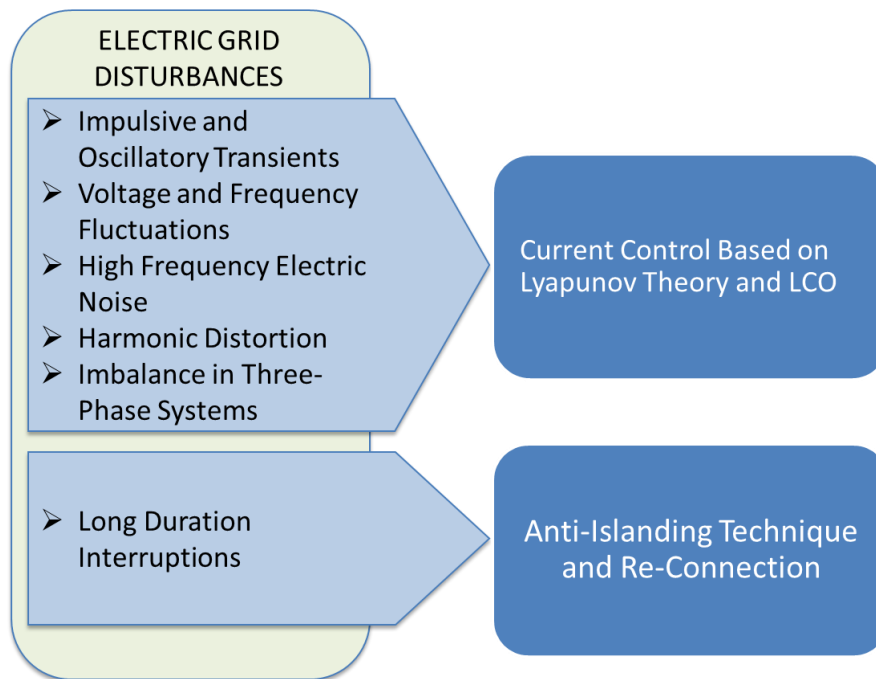


Figure 5.1. Overview of the controller systems to manage different kind of disturbances in the electric grid.

There are numerous Anti-Islanding (AI) techniques which detect islanding conditions and isolate the DPGS from the grid in a short period of time [50], [86]. These techniques can be broadly classified into remote and local methods. Remote-AI techniques are based on communication systems to inform the DPGS of islanding conditions. These schemes are still too expensive but they have very high reliability [87]–[89].

Local AI techniques can be divided into passive, machine learning and active techniques. Passive schemes just monitor voltage, current, and frequency changes at the Point of Common Coupling (PCC) without affecting the power quality. They are simple, low-cost schemes and easy to implement. However, these schemes have large Non-Detection Zones (NDZ) where they could fail to detect islanding conditions [90]–[92].

Machine learning schemes are learning algorithms that need to be trained to classify the islanding and no-islanding cases. They have good performance to classify the events, however, if the electric topology changes, these techniques need to be retrained in the new electric conditions [93]–[98].

Active AI techniques inject perturbations in the current waveform as amplitude, frequency or phase parameters. When there are no islanding conditions, the perturbations are absorbed by the grid, however, when there are islanding conditions, these perturbations carry the system to instability conditions in order to activate the protection system [99]–[107].

The main contribution of this Chapter is a Modified Sandia Voltage Shift (MSVS) active anti-islanding scheme with faster response than Sandia Voltage Shift (SVS) maintaining its small Non-Detection Zone (NDZ) and its good compromise between output power quality, the effectiveness of islanding detection and reduced effects of the system transient response [108]. The improved detection time is due to the exponential-product modification made in the positive feedback to inject current to the grid. This feature gives an original characteristic to the proposed technique, making it a good alternative for anti-islanding systems.

The Chapter is organized as follows. A brief description of the SVS principle and characteristics of the proposed MSVS anti-islanding scheme for DPGS are shown in section 5.1. Experimental results are depicted in section 5.2. Finally, the conclusions are summarized in section 5.3.

5.1 Modified Sandia Voltage Shift

Sandia National Laboratories proposed the change of the chopping fraction of the grid-connected inverter current directly proportional to the instantaneous peak voltage in the Point of Common Coupling (PCC) [108]. This method uses a positive feedback loop of the PCC voltage amplitude to detect islanding. If the voltage amplitude increases/decreases, the inverter rises/reduces its output current and thus the output power; this process continues until the voltage reaches an Over-Under Voltage (OUV) threshold. A block diagram of the basic technique SVS can be seen in the white area of Figure 5.2, where the main equation is the next:

$$I_{ref\ dis} = K_e V_e, \quad (5.1)$$

where $I_{ref\ dis}$ is the disconnection reference current, which is added to the current reference I_{ref} of the inverter current control in order to make the positive feedback loop,

V_e is the voltage error between a voltage peak reference $V_{p\ ref}$ and the measured voltage V_p at PCC, and K_e is a gain to adjust the response time of the algorithm, which decreases or increases the current directly proportional to the voltage error variation V_e . This gain K_e should be chosen large enough to detect the islanding condition avoiding overcurrent which could damage the electric elements [86].

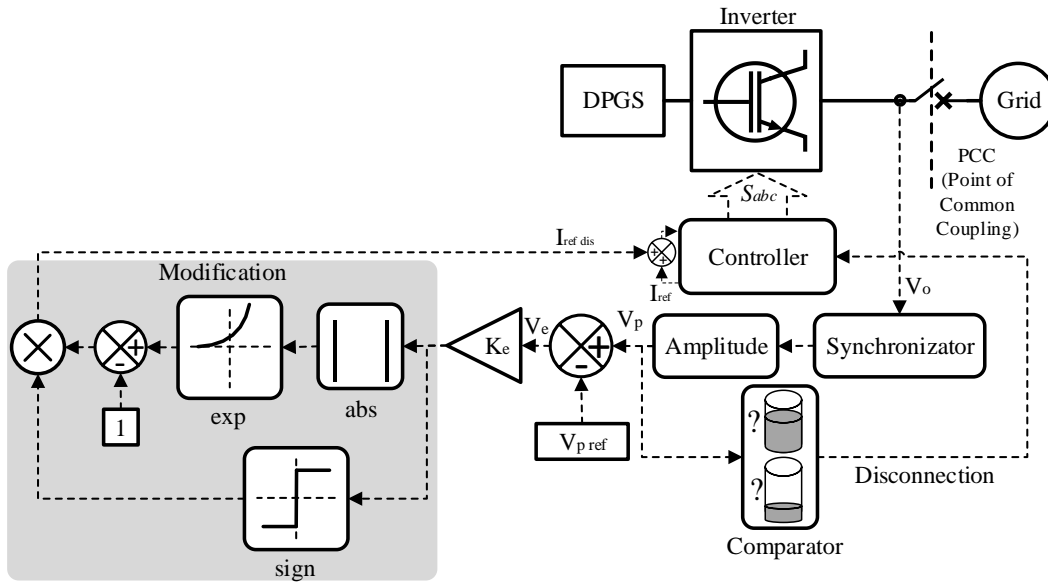


Figure 5.2. Modified Sandia Voltage Shift block diagram.

For the proposed islanding scheme MSVS, a modification block in the positive linear feedback of the normal SVS has been added, making an exponential-product adjustment to inject current into the grid. This proposed variation is showed in Figure 5.2, in the shaded area, and it is composed of a sign, exponential, and an absolute function in order to have the following equation:

$$I_{ref\ dis} = [e^{|K_e V_e|} - 1]sign(K_e V_e). \quad (5.2)$$

It can be deduced from Figure 5.2 and (5.2), that if the measured voltage at PCC increases/decreases, the inverter current will rises/reduces at an exponential rate until the voltage reaches the OUV threshold, having a better islanding detection time than SVS which has linear feedback. It is important to say that increasing the gain K_e in the SVS affects its performance at the steady state of the system. This problem does not happen in the proposed MSVS.

5.2 Experimental Tests

Experimental tests of the system in Figure 5.2 are shown below in order to validate the high performance of the MSVS active anti-islanding technique versus the normal technique SVS. The anti-islanding techniques were implemented in a Single Board of National Instruments based on an FPGA Xilinx Spartan-6 LX45 at 2.5 MHz, moreover, these experimental tests were made in a three-phase inverter connected to a local load, and a programmable ac power source Chroma 61700 which emulates the utility grid.

The experimental test is divided into four cases according to the current flow among the DPGS-Inverter, Load, and Grid (See e.g. Figure 5.3 (a)). Furthermore, every case shows the three-phase voltages in the PCC, and the islanding and detection Boolean flags at the bottom of every graphic (See e.g. Figure 5.3 (b) and (c)), moreover, the power quantities of every case are depicted in Table V.I. Current graphics have been omitted because they have similar waveform of the voltages since a linear load was employed, except for the case 4.

TABLE V.I
EXPERIMENTAL TEST POWER FLOW

Case	DPGS Power	Load Power	Grid Power
1	1000 W	1000 W	0 W
2	300 W	1000 W	700 W
3	1300 W	1000 W	-300 W (<i>Injected</i>)
4	1000 W	750 W	-250W (<i>Injected</i>)

$K_e=0.1$ for MSVS and SVS

The Case 1 is when there is no current injection to the Grid, that is, the current flows only from the DPGS-Inverter to the Load, as it can be seen in Figure 5.3 (a), making it the worst case of study. Certainly, this case is made to verify the NDZ of the proposed technique, as it can be seen in Figure 5.3 (b), the MSVS takes 7ms to detect the islanding condition, however, the SVS takes a longer time of 27ms to detect the islanding condition (See Figure 5.3 (c)). That is more than three times of MSVS detection time.

The Case 2 is shown in Figure 5.3 (d) and it is when the DPGS-Inverter and Grid share the power generation for the Load. It can be seen in Figure 5.3 (e) that the MSVS has a detection time of 2.1ms, however, the SVS technique has a longer detection time of 6.5ms (Figure 5.3 (f)).

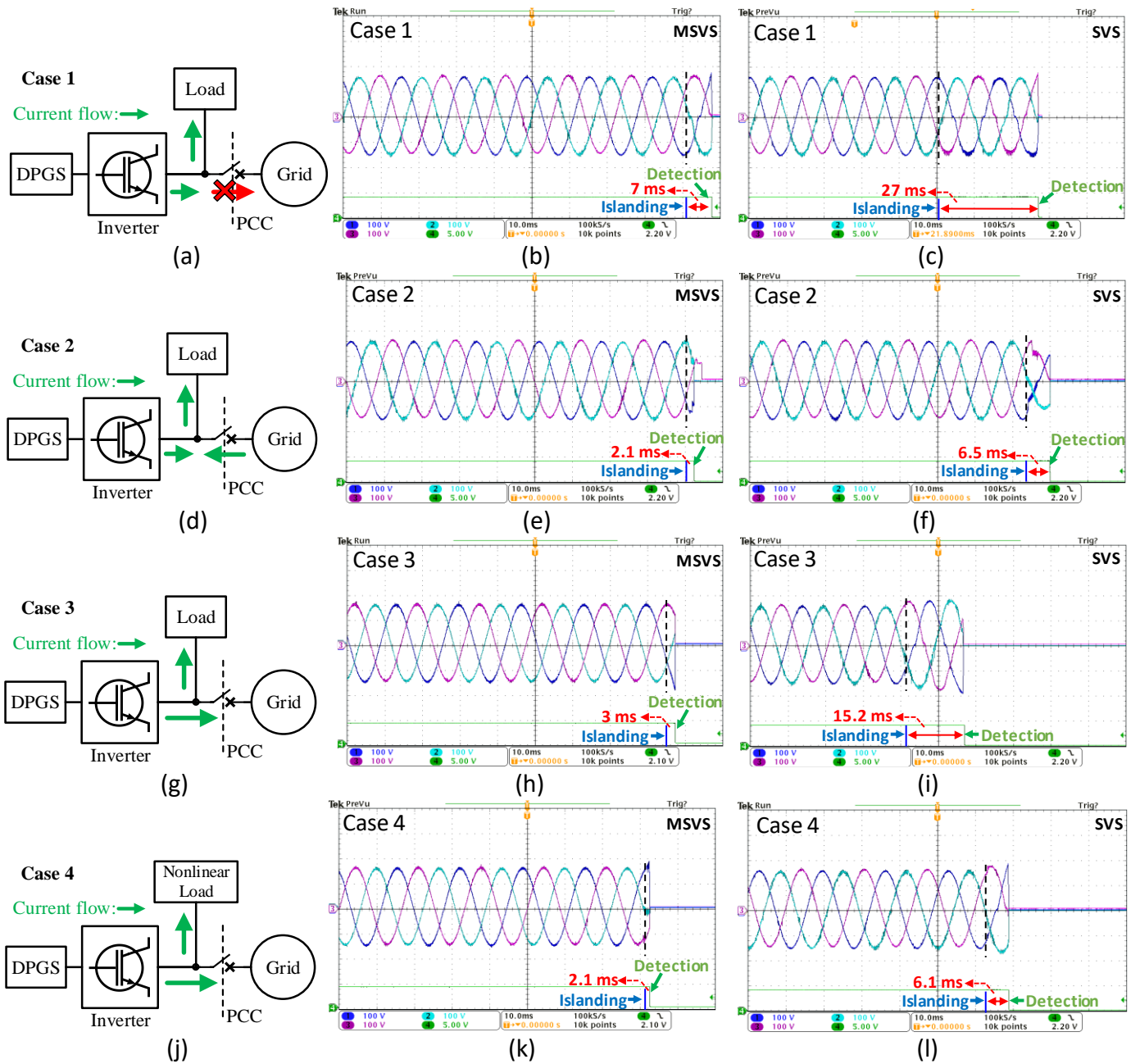


Figure 5.3. Experimental tests. Comparison between MSVS and SVS anti-islanding techniques in four different cases depending in the current flow. PCC voltage (up), and islanding and detection flags (down).

The Figure 5.3 (g) shows the Case 3 where the DPGS-Inverter injects current to the Grid and also feeds the local Load. In this Case, the MSVS technique has a detection time of 3ms and the SVS technique has a longer detection time with 15.2ms (See Figure 5.3 (h) and (i) respectively).

Finally, the Case 4 is showed in Figure 5.3 (j). In this Case, the DPGS-Inverter injects current to the Grid and also feeds a local Nonlinear Load (Three phase rectifier). As it can be seen in Figure 5.3 (k), the MSVS has a detection time of 2.1ms, however, the SVS has longer detection time after the islanding condition with 6.1ms (See Figure 5.3 (l)).

Summarizing the four cases of study, it can be seen that in all the tests, the NDZ has been maintained, moreover, the detection time has been reduced, making the transient response three times faster than SVS, reducing potential damage to the load.

5.3 Remarks on MSVS

This Chapter introduces a Modified Sandia Voltage Shift (MSVS) active anti-islanding scheme that has a faster islanding detection response than Sandia Voltage Shift (SVS) maintaining its small Non-Detection Zone (NDZ) and its good compromise between output power quality, the effectiveness of islanding detection and reduced effects of the system transient response [108]. The improved detection time is due to the exponential-product modification made in the positive feedback to inject current into the grid. This feature gives an important improvement to the proposed technique, making it a good alternative for anti-islanding detection method. This proposed scheme has been validated and verified by experimental results.

6.

RE-CONNECTION OF A DPGS TO THE GRID NETWORK WITH A CRITICAL LOAD

In the previous Chapter, it was introduced a system to prevent islanded conditions for the DPGS. In this Chapter, a DPGS which can be working even in islanded mode is described. For this mode, it is important to consider a re-connection process from an islanded system to a connected system. Moreover, it must be taken in mind different specifications in order to maintain the process reliable, effective and safe. In this sense, in this kind of islanded systems there exist critical loads which must be all the time fed, independently of the process of reconnection, as it can be seen in Figure 6.1. Moreover, the fundamental frequency should be constant with variations within $\pm 0.1 \text{ Hz}$ and the energy quality of the critical loads must be warranted.

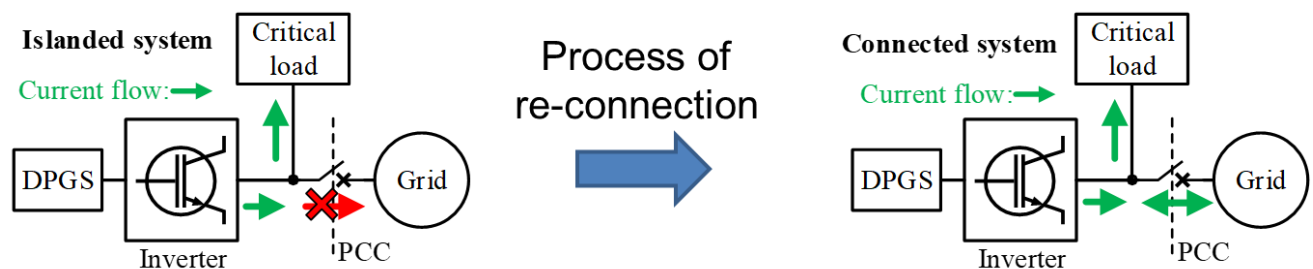


Figure 6.1. Process of re-connection of a DPGS to the grid network with a critical load.

6.1 Proposed DPGS System with Islanding Capability

The proposed DPGS System with islanded capability is depicted in Figure 6.2. As it can be seen, the DPGS needs an LCL filter in order to work in islanded mode and to feed all the time the critical load. Moreover, due to the synchronization techniques have a faster transient in comparison with the fundamental frequency, a pre-synchronization block before the synchronization system is needed, in order to avoid a deterioration of the THD_V in the process of reconnection. It is important to highlight that it can be used other kind of synchronization techniques and not only the LCO-FLL.

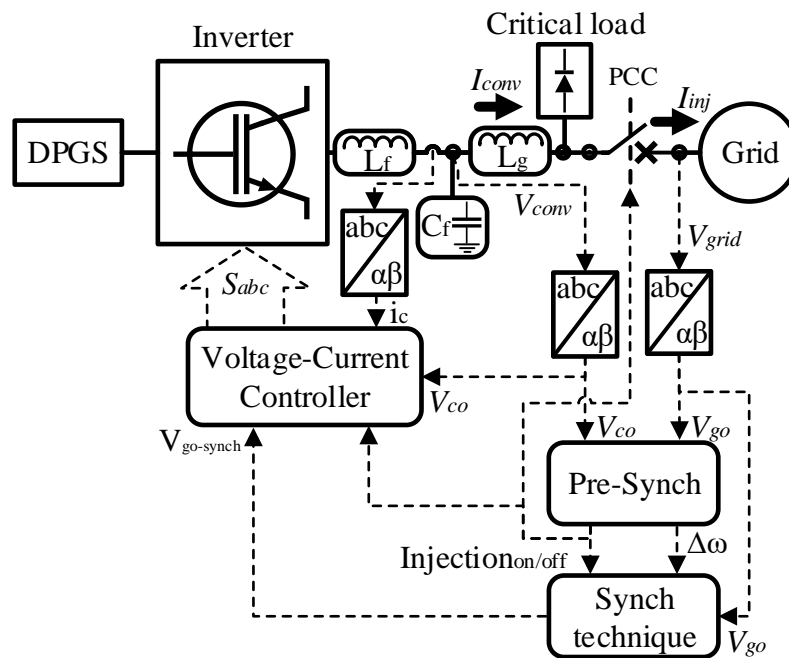


Figure 6.2. Block diagram of the DPGS connected to the electric grid and the control system.

The control of the system from Figure 6.2 has two measure points of voltage, one in the grid side and other in the C_f filter. Both of them, are transformed from abc to $\alpha\beta$ reference frames and they are connected to the pre-synchronization block. This pre-synchronization block makes the decision when to shift the frequency ($\Delta\omega$, which is a constant value) of the islanded system in order to get the same phase as the grid network. Once the islanded system gets the same phase with the grid, this pre-synchronization block makes the decision to start the synchronization block and it sends a signal to the Voltage-Current Controller block to start the current injection to the grid. This Voltage-

Current Controller block has four input signals, the synchronized grid voltages ($V_{go-synch}$), the injection decision signal ($Injection_{on/off}$), the voltage measured in the C_f filter (V_{co}), and the current measured in the L_f filter (i_c).

The next Figures depict the different blocks with more details. The Figure 6.3 shows the Pre-Synchronization block, this system tries to diminish the phase gap between the Grid Voltage (V_{go}) and the voltage generated by the inverter (V_{co}). By mean of a Flip-Flop, a shift frequency ($\Delta\omega$) is added to the fundamental frequency of the inverter in order to match the phase with the grid. Moreover, in this block an islanded detection method is considered when occurs a grid fault. This islanded detection method can be any kind of islanded detection technique existing in the state of the art.

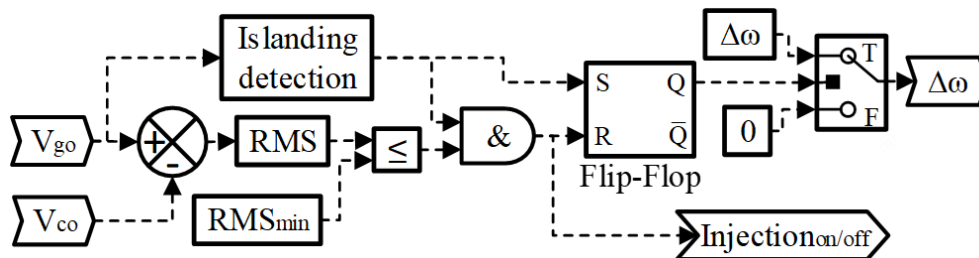


Figure 6.3. Pre-Synchronization block.

Now for the synchronization block. The shift frequency ($\Delta\omega$) is added to ω in the synchronization system in order to match the phase with the grid network, as it can be seen in Figure 6.4. Once both systems, the grid and the islanded DPGS have the same phase, the synchronization block starts to work, and the shift frequency ($\Delta\omega$) becomes zero. In this sense, this block generates the synchronized grid voltages signal ($V_{go-synch}$).

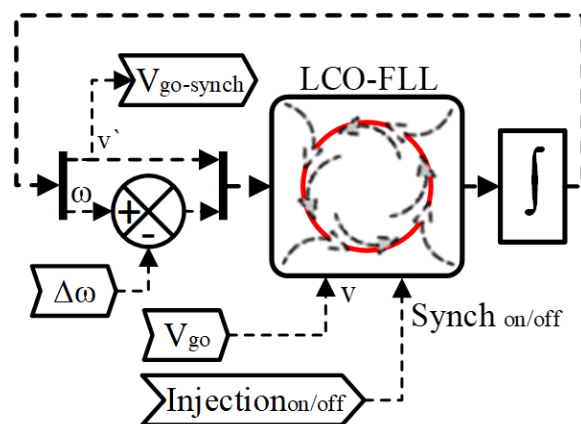


Figure 6.4. Synchronization block.

In order to control the voltages and currents generated by the inverter, two different controllers were used, one is a voltage-current (Proportional-Resonant) PR Controller showed in Figure 6.5, and another one is a Predictive Voltage-Current controller depicted in Figure 6.6. These Voltage-Current controllers have as inputs the synchronized grid voltages signal ($V_{go-synch}$), the voltage measured in the C_f filter (V_{co}), and the current measured in the L_f filter (i_c). Moreover, these two controllers have the capacity to switch from the islanded mode to the grid-connected mode, depending on the injection signal ($Injection_{on/off}$).

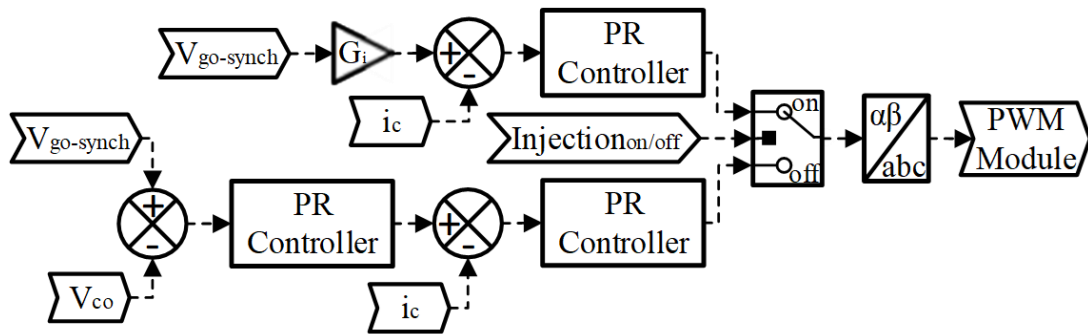


Figure 6.5. Voltage-Current PR controller block.

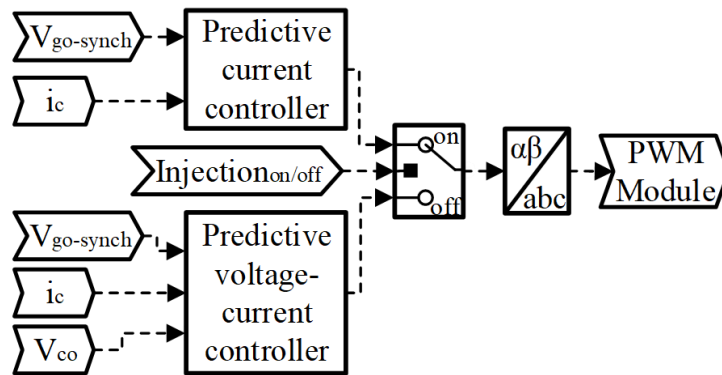


Figure 6.6. Predictive Voltage-Current controller block.

Therefore, the Voltage-Current controller in Figure 6.5 switches from a single PR controller (Grid-connected mode) to a cascade PR controller topology (Islanded mode). For the Predictive controller in Figure 6.6, it switches in the same way as the PR controller, this is, from a Predictive Current controller to a predictive Voltage-Current controller.

6.2 Simulation tests

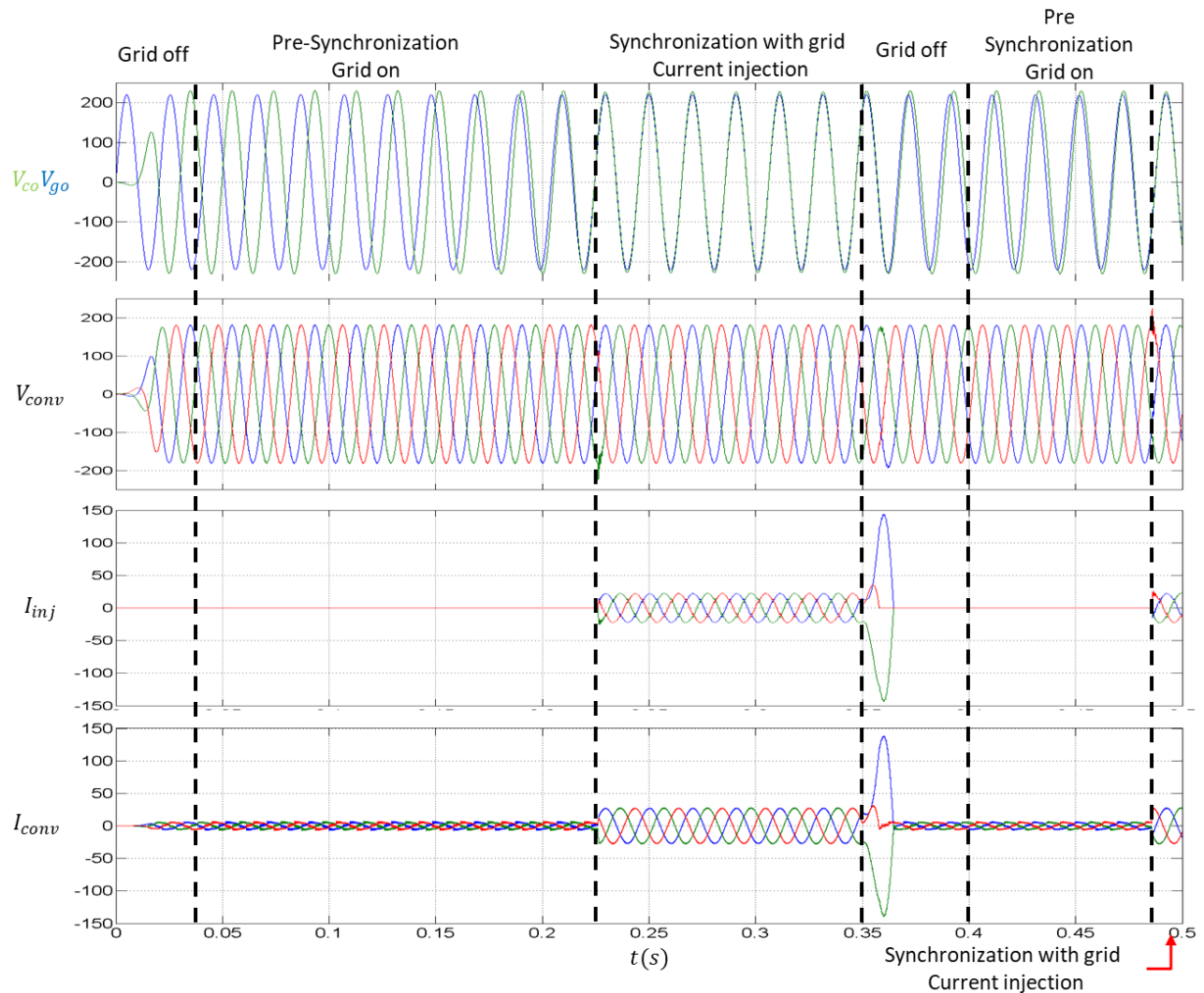


Figure 6.7. Test of the reconnection process of the DPGS to the grid with a critical load using the PR controller.

Simulation tests of the system in Figure 6.2 are shown below in order to validate and to verify the performance and the correct working of the different blocks of the reconnection system. The re-connection system with the PR Controller is evaluated in Figure 6.7. The pre-synchronization system starts to work and the phase gap between the inverter voltage (V_{co} - green line), and the grid voltage (V_{go} - blue line) start to diminish, as it can be seen in the first row of Figure 6.7. After this, the synchronization block starts to work and the DPGS starts to inject current to the grid (I_{inj}) as it is showed in the third

row of Figure 6.7. In order to see the behavior of the system in a grid fault, an interruption is caused at 0.35 s. In this point, the voltage generated by the converter (V_{conv}) is not affected, however, an overshoot is generated in the injected current when occurs the switch from the grid connected to the islanded mode, as it can be seen in the third (I_{inj}) and fourth (I_{conv}) row of Figure 6.7. It is important to highlight that the critical load is always fed by the DPGS (I_{conv}) and the quality of the converter voltage (V_{conv}) is also ensured.

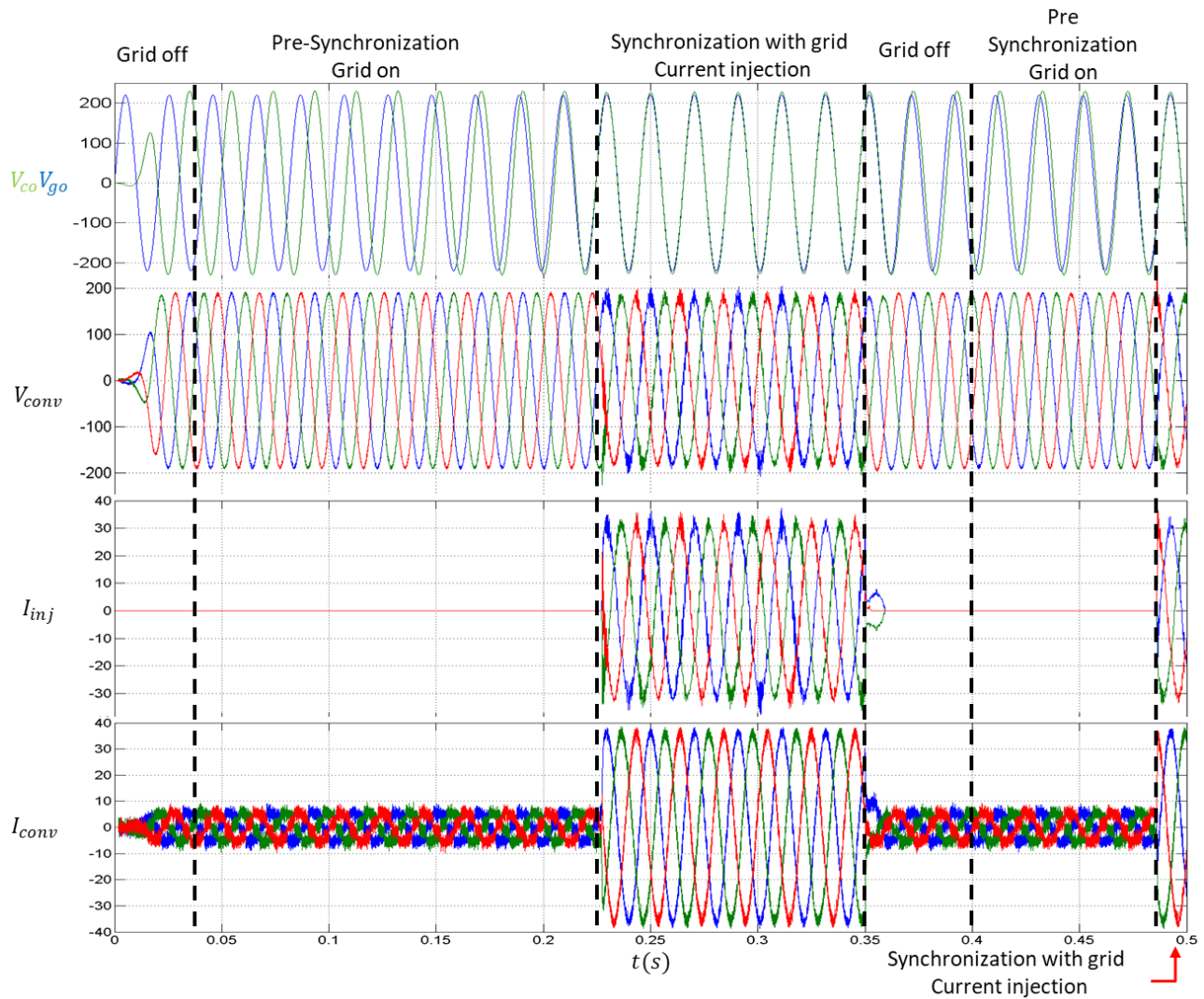


Figure 6.8. Test of the reconnection process of the DPGS to the grid with a critical load using the Predictive Voltage-Current controller.

The same simulation test was made for the Predictive controller block which is depicted in Figure 6.8. The re-connection system has similar behavior than the previous system, however, as it can be seen in the third (I_{inj}) and fourth (I_{conv}) row of the graphic in Figure 6.8, there are no currents overshooting in the switching process from Predictive current controller, which is for grid-connected mode to Predictive Voltage-Current controller, which is for islanded mode. Moreover, it can be seen electric noise immerse in the voltage (V_{conv}) in the grid-connected mode in the second row of the graphic.

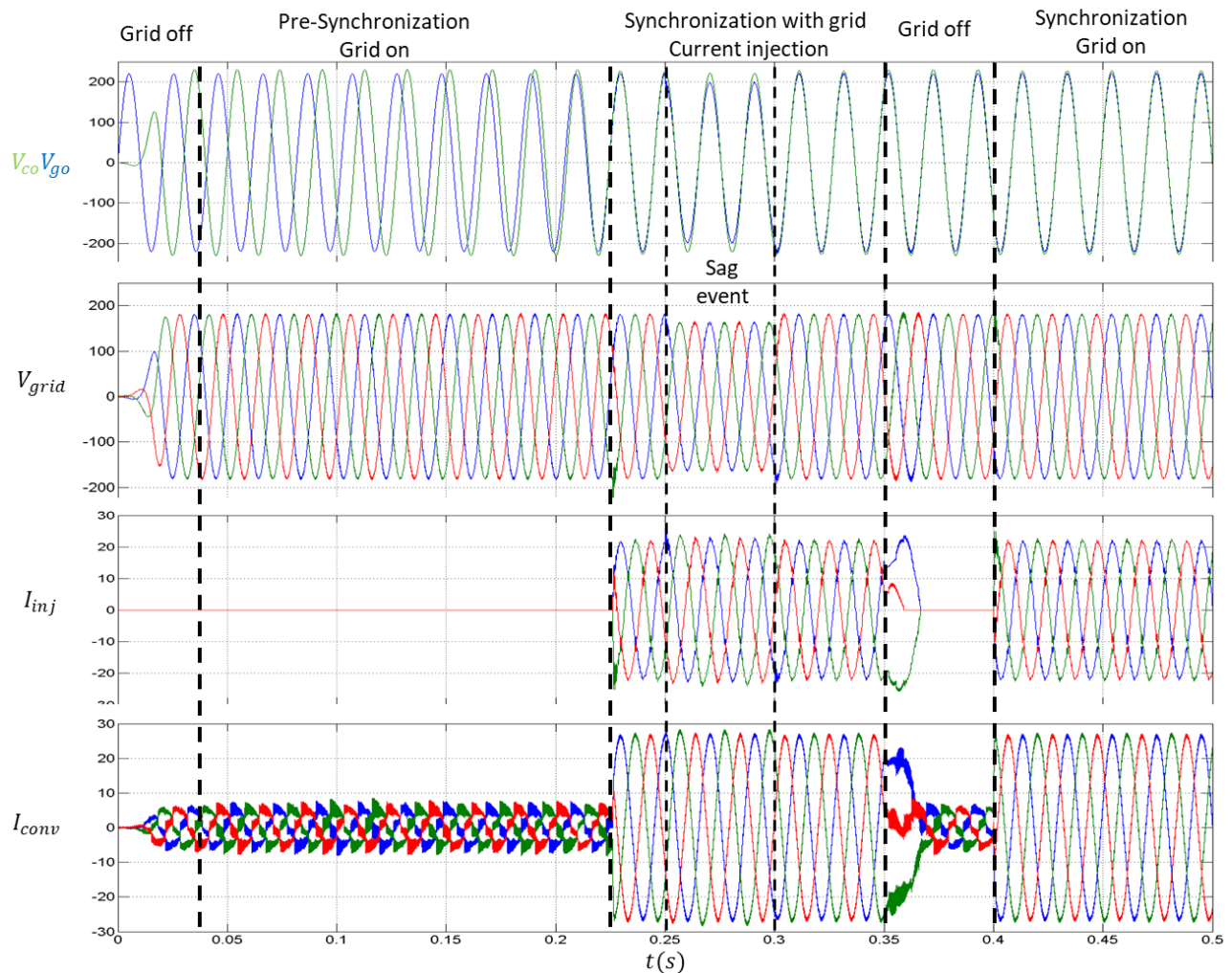


Figure 6.9. Test of the DPGS connected to the grid with a critical load with a Sag event using the PR controller.

Another simulation is made with the same characteristics than in Figure 6.7 and 6.8, but now a fault condition (Sag event) is applied from 0.25 s to 0.3 s, as it can be seen in Figure 6.9. In this case, the PR controller is working with the LCO-FLL as the synchronization block, that is why the injected current generated by the inverter remains with the same amplitude, even with the sag event, as it can be seen in the third (I_{inj}) and fourth (I_{conv}) row of the graphic in Figure 6.9.

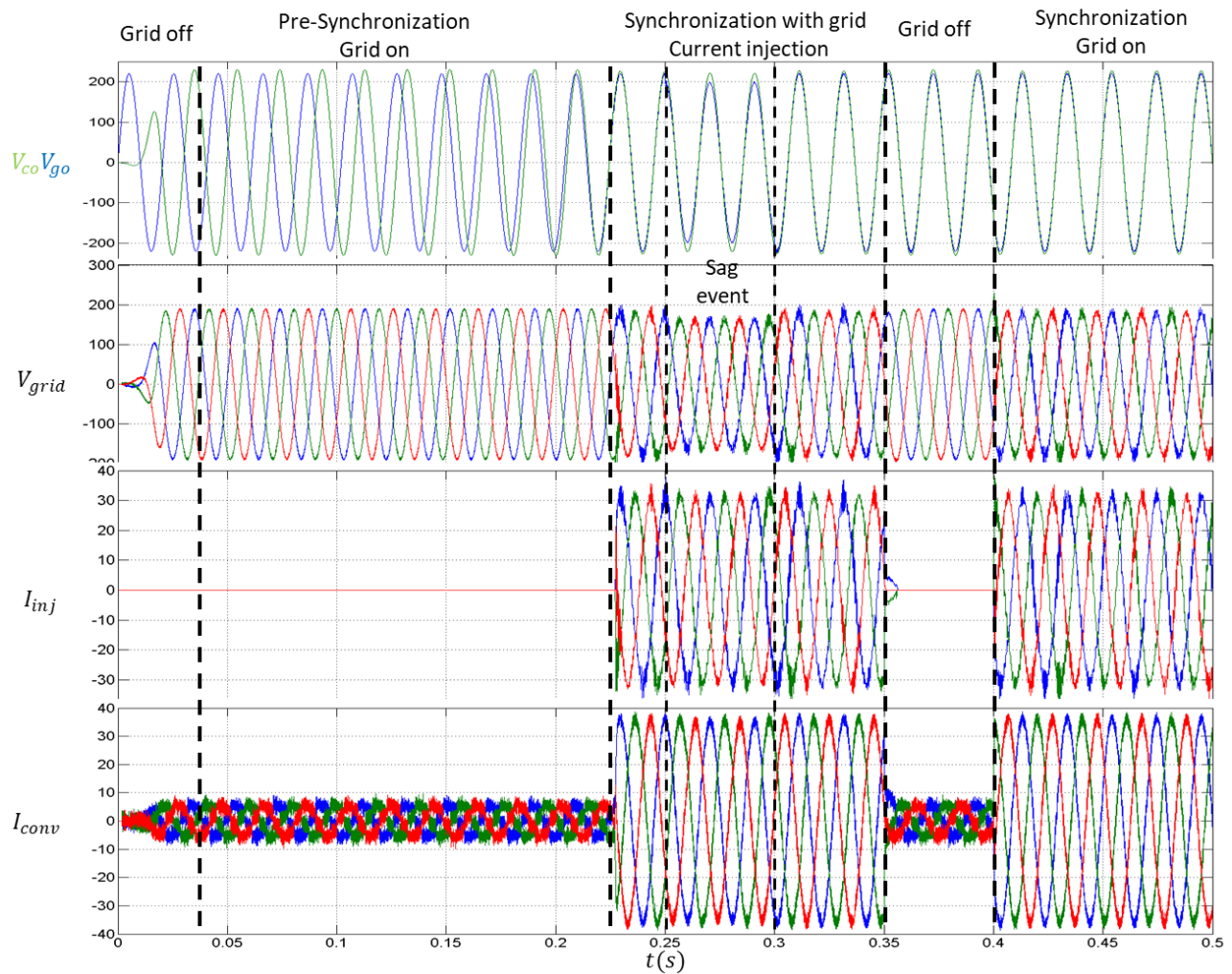


Figure 6.10. Test of the DPGS connected to the grid with a critical load with a Sag event using the Predictive Voltage-Current controller.

Finally, in the Figure 6.10 is depicted a simulation with the same characteristics than in Figure 6.9 with a Sag event from 0.25 s to 0.3 s, but in this case, the Predictive controller

is working together with the LCO-FLL synchronization block. It can be seen that the injected currents remain with the same amplitude during the fault event, due to the LCO-FLL synchronization block.

7.

CONCLUSION AND FINAL REMARKS

The conclusions and final remarks are related with the specific objectives introduced in Section 1.3.

The following conclusions are addressed to the first specific objective:

- A new synchronization system based on the concept of LCO for grid-connected converters is developed. A stability analysis for the single LCO was given, moreover, local stability and a numerical stability analysis confirm the stability of the interconnected LCO-FLL. The proposed method was compared with different synchronization techniques under optimized parameters for every system. Different tests were made, showing that the LCO-FLL provides suitable transients with better settling times than the compared systems.
- The LCO-FLL produces synchronized signals with constant amplitude despite variations within the normal operation marked in IEEE 1547 Standard.
- The LCO-FLL structure is based on the estimation of the grid voltage frequency since the grid frequency variable is more robust than the voltage phase angle during transient faults. Moreover, the LCO-FLL does not process any trigonometric function since any conventional voltage-controlled oscillator is used in its implementation. This feature contributes to reducing the time and computational resources.

- The three-phase LCO-FLL is a suitable solution to accurately detect the fundamental-frequency positive and negative sequence components of the grid voltage, under highly distorted and unbalanced grid scenarios in less than a half grid voltage cycle.
- The extended version of the three-phase LCO-FLL has the capacity to detect the positive and negative sequence components of the multiple harmonics of the fundamental frequency, characterizing the harmonic spectrum of the three-phase grid network.

The final conclusions are addressed to the second specific objective:

- A current controller based on the Limit Cycle Oscillator nonlinear theory and combined with a Lyapunov control law under Balanced Injected Currents (BIC) or Constant Active Power (CAP) strategy has been developed for a PV-Grid connected system.
- One advantage of the proposed control scheme is that the dc bus voltage is included into the controller, which permits to be suitable to consider the MPPT algorithm, making an important advantage versus other actual Lyapunov controllers.
- It only requires to solve a seventh order differential equation over other current controllers that need to solve differential equations between the 12th and 26th order to secure an efficient harmonic current rejection and active power compensation during the current injection in an unbalanced grid.
- A Modified Sandia Voltage Shift (MSVS) active anti-islanding scheme is introduced. It has a faster islanding detection response than Sandia Voltage Shift (SVS), moreover, it maintains its small Non-Detection Zone (NDZ) and its good compromise between output power quality, the effectiveness of islanding detection and reduced effects of the system transient response.
- A re-connection system with the electric grid for DPGS with critical loads is developed, maintaining the energy quality and the stability system.

It is important to highlight that the development of the extended version of the three-phase LCO-FLL (Section 3.7 and 3.8), the MSVS active anti-islanding technique (Chapter 5), and the re-connection system with the electric grid for DPGS with critical

loads (Chapter 6), was a great effort to give an integral and complete solution to grid synchronization systems under a wide range of different grid faults.

In conclusion, it is possible to diminish electric grid disturbances by means of synchronization of Distributed Power Generation Systems (DPGS), in specific a Photovoltaic (PV) system, using Lyapunov control in combination with Limit Cycle Oscillators (LCOs), which is the hypothesis of this dissertation.

7.1 Future Work

The research opens different important questions in the field of synchronization systems and current injection to the electric grid. Some of these research paths are summarized below:

- Perform a deeper analysis of the stability disconnected regions found in the stability analysis with the direct Lyapunov method. This issue has an important relevance because most of the stability analysis for synchronization systems have reached only limited conclusions because they have been made with linearized models. Therefore, a stability analysis with nonlinear models might get a wider understanding in the behavior of these systems.
- Detect sub-harmonics and inter-harmonics and detect their positive and negative sequence components with an improved three-phase LCO-FLL. Grid signal analyzers need a great computation requirement since the complex mathematics operations. Therefore, signal analyzers with a small percentage of computation resources might be an important technological contribution.
- Analyze the conditions to detect sub-harmonics and inter-harmonics. This issue is important in order to know the limitations and weaknesses of the system to detect the positive and negative sequence components.
- Inject energy to a weak electric grid and analyze the characteristics of its impedance. Nowadays, weak electric grid is a novel topic due to the high penetration of intermittent renewable energy. Therefore, grid impedance in connected systems is an important issue in power electronic topics.
- Analyze the dynamical behavior of a micro-grid with two or more DPGS in order to study the interaction between them and the electric grid. A micro-grid

interconnected system is a huge topic with an important growth in industrial applications. Therefore, it is a significant niche of opportunity in scientific and technological research.

- Compensate modelling errors with the Lyapunov current control.

8.

REFERENCES

- [1] International Renewable Energy Agency, “Data and Statistics - IRENA Resource,” *Capacity and Generation*, 2018. [Online]. Available: <http://resourceirena.irena.org/gateway/dashboard/?topic=4&subTopic=16>. [Accessed: 05-Jul-2018].
- [2] C. Lins *et al.*, “REN21 STEERING COMMITTEE EXECUTIVE SECRETARY INDUSTRY ASSOCIATIONS Chinese Renewable Energy Industries Association (CREIA) Irene Giner-Reichl Global Forum on Sustainable Energy (GFSE) Mali Folkecenter (MFC) / Citizens United for Renewable Energy and Sustainability World Council for Renewable Energy (WCRE) MEMBERS AT LARGE SCIENCE AND ACADEMIA.”
- [3] F. Blaabjerg, Y. Yang, D. Yang, and X. Wang, “Distributed Power-Generation Systems and Protection,” *Proceedings of the IEEE*, vol. 105, no. 7. pp. 1311–1331, Jul-2017.
- [4] G. D. J. Martinez-Figueroa, D. Morinigo-Sotelo, A. L. Zorita-Lamadrid, L. Morales-Velazquez, and R. D. J. Romero-Troncoso, “FPGA-Based Smart Sensor for Detection and Classification of Power Quality Disturbances Using Higher Order Statistics,” *IEEE Access*, vol. 5, pp. 14259–14274, 2017.
- [5] IEEE Standards Coordinating Committee 22 on Power Quality, *IEEE Recommended Practice for Monitoring Electric Power Quality*. Institute of Electrical and Electronics Engineers, 1995.
- [6] IEEE, *998-2012 IEEE Guide for Direct Lightning Stroke Shielding of Substations*. 2013.
- [7] J. Arrillaga, M. H. J. Bollen, S. Member, and N. R. Watson, “Power quality following deregulation,” *Proc. IEEE*, vol. 88, no. 2, pp. 246–261, Feb. 2000.
- [8] C. B. Cooper, “IEEE Recommended Practice for Electric Power Distribution for Industrial Plants,” *Power Eng. J.*, vol. 2, no. 2, p. 103, 1988.
- [9] M. H. J. Bollen, “Characterisation of voltage sags experienced by three-phase adjustable-speed drives,” *IEEE Trans. Power Deliv.*, vol. 12, no. 4, pp. 1666–1671, 1997.
- [10] M. H. J. Bollen, *Understanding power quality problems: voltage sags and interruptions*.

- New York, NY: IEEE Press, 2000.
- [11] M. H. J. Bollen and R. A. A. de Graaff, "Behavior of AC and DC drives during voltage sags with phase-angle jump and three-phase unbalance," *IEEE Power Eng. Soc. 1999 Winter Meet. (Cat. No.99CH36233)*, vol. 2, pp. 1225–1230 vol.2, 1999.
 - [12] A. Rolán, J. Pedra, and F. Córcoles, "Detailed study of DFIG-based wind turbines to overcome the most severe grid faults," *Int. J. Electr. Power Energy Syst.*, vol. 62, pp. 868–878, Nov. 2014.
 - [13] M. H. J. Bollen, "Voltage recovery after unbalanced and balanced voltage dips in three-phase systems," *IEEE Trans. Power Deliv.*, vol. 18, no. 4, pp. 1376–1381, Oct. 2003.
 - [14] D. Shmilovitz, "On the definition of total harmonic distortion and its effect on measurement interpretation," *IEEE Trans. Power Deliv.*, vol. 20, no. 1, pp. 526–528, Jan. 2005.
 - [15] IEEE-Standard, *519-2014 - IEEE Recommended Practice and Requirements for Harmonic Control in Electric Power Systems*. 2014.
 - [16] E. Oviedo, N. Vazquez, and R. Femat, "Synchronization Technique of Grid-Connected Power Converters Based on a Limit Cycle Oscillator," *IEEE Trans. Ind. Electron.*, vol. 65, no. 1, pp. 709–717, 2018.
 - [17] F. Blaabjerg, R. Teodorescu, M. Liserre, and A. V Timbus, "Overview of control and grid synchronization for distributed power generation systems," *IEEE Trans. Ind. Electron.*, vol. 53, no. 5, pp. 1398–1409, 2006.
 - [18] R. W. Wall, "Simple Methods for Detecting Zero Crossing," in *IECON Proceedings (Industrial Electronics Conference)*, 2003, vol. 3, pp. 2477–2481.
 - [19] S. Vazquez, J. A. Sanchez, M. R. Reyes, J. I. Leon, and J. M. Carrasco, "Adaptive vectorial filter for grid synchronization of power converters under unbalanced and/or distorted grid conditions," *IEEE Trans. Ind. Electron.*, vol. 61, no. 3, pp. 1355–1367, Mar. 2014.
 - [20] X. Wang and E. E. Yaz, "Smart Power Grid Synchronization with Fault Tolerant Nonlinear Estimation," *IEEE Trans. Power Syst.*, vol. 31, no. 6, pp. 4806–4816, Nov. 2016.
 - [21] E. V. Appleton, "Automatic synchronization of triode oscillators," *Proc. Cambridge Phil. Soc.*, vol. 21, no. III, p. 231, 1923.
 - [22] H. Bellescize, "La reception synchrone," *Onde Electr.*, vol. 11, pp. 230–240, 1932.
 - [23] G. C. Hsieh and J. C. Hung, "Phase-locked loop techniques - A survey," *IEEE Trans. Ind. Electron.*, vol. 43, no. 6, pp. 609–615, Dec. 1996.
 - [24] D. Jovcic, "Phase locked loop system for FACTS," *IEEE Trans. Power Syst.*, vol. 18, no. 3, pp. 1116–1124, Aug. 2003.
 - [25] H.-S. Song and K. Nam, "Instantaneous phase-angle estimation algorithm under unbalanced voltage-sag conditions," *IEE Proc. - Gener. Transm. Distrib.*, vol. 147, no. 6, p. 409, 2000.
 - [26] M. Karimi Ghartemani, S. A. Khajehoddin, P. K. Jain, and A. Bakhshai, "Problems of startup and phase jumps in PLL systems," *IEEE Trans. Power Electron.*, vol. 27, no. 4, pp. 1830–1838, Apr. 2012.
 - [27] M. Karimi-Ghartemani and M. R. Iravani, "A new phase-locked loop (PLL) system," in *Proceedings of the 44th IEEE 2001 Midwest Symposium on Circuits and Systems. MWSCAS*

- 2001 (Cat. No.01CH37257), 2001, vol. 1, pp. 421–424.
- [28] L. Hadjidemetriou, E. Kyriakides, Y. Yang, and F. Blaabjerg, “A synchronization method for single-phase grid-tied inverters,” *IEEE Trans. Power Electron.*, vol. 31, no. 3, pp. 2139–2149, Mar. 2016.
- [29] H. Karimi, M. Karimi-Ghartemani, and M. R. Iravani, “Estimation of Frequency and its Rate of Change for Applications in Power Systems,” *IEEE Trans. Power Deliv.*, vol. 19, no. 2, pp. 472–480, Apr. 2004.
- [30] M. Karimi-Ghartemani, H. Karimi, and M. R. Iravani, “A magnitude/phase-locked loop system based on estimation of frequency and in-phase/quadrature-phase amplitudes,” *IEEE Transactions on Industrial Electronics*, vol. 51, no. 2, pp. 511–517, Apr-2004.
- [31] A. Nagliero, R. A. Mastromauro, M. Liserre, and A. Dell’Aquila, “Synchronization techniques for grid connected wind turbines,” *2009 35th Annu. Conf. IEEE Ind. Electron.*, pp. 4606–4613, Nov. 2009.
- [32] X. Yuan, W. Merk, H. Stemmler, and J. Allmeling, “Stationary-frame generalized integrators for current control of active power filters with zero steady-state error for current harmonics of concern under unbalanced and distorted operating conditions,” in *IEEE Transactions on Industry Applications*, 2002, vol. 38, no. 2, pp. 523–532.
- [33] P. Rodríguez, R. Teodorescu, I. Candela, A. V. Timbus, M. Liserre, and F. Blaabjerg, “New positive-sequence voltage detector for grid synchronization of power converters under faulty grid conditions,” in *PESC Record - IEEE Annual Power Electronics Specialists Conference*, 2006, pp. 1–7.
- [34] M. Ciobotaru, R. Teodorescu, and F. Blaabjerg, “A new single-phase PLL structure based on second order generalized integrator,” in *PESC Record - IEEE Annual Power Electronics Specialists Conference*, 2006, pp. 1–6.
- [35] P. Rodríguez, A. Luna, I. Candela, R. Mujal, R. Teodorescu, and F. Blaabjerg, “Multiresonant frequency-locked loop for grid synchronization of power converters under distorted grid conditions,” *IEEE Trans. Ind. Electron.*, vol. 58, no. 1, pp. 127–138, Jan. 2011.
- [36] A. Nicastrì and A. Nagliero, “Comparison and evaluation of the PLL techniques for the design of the grid-connected inverter systems,” in *IEEE International Symposium on Industrial Electronics*, 2010, pp. 3865–3870.
- [37] P. Rodríguez, A. Luna, M. Ciobotaru, R. Teodorescu, and F. Blaabjerg, “Advanced grid synchronization system for power converters under unbalanced and distorted operating conditions,” in *IECON Proceedings (Industrial Electronics Conference)*, 2006, pp. 5173–5178.
- [38] D. Yazdani, A. Bakhshai, G. Joos, and M. Mojiri, “A nonlinear adaptive synchronization technique for grid-connected distributed energy sources,” *IEEE Trans. Power Electron.*, vol. 23, no. 4, pp. 2181–2186, Jul. 2008.
- [39] P. Rodríguez, A. Luna, R. S. Muñoz-Aguilar, I. Etxeberria-Otadui, R. Teodorescu, and F. Blaabjerg, “A stationary reference frame grid synchronization system for three-phase grid-connected power converters under adverse grid conditions,” *IEEE Trans. Power Electron.*, vol. 27, no. 1, pp. 99–112, Jan. 2012.
- [40] IEEE Standards Coordinating Committee 21, *IEEE Application Guide for IEEE Std 1547™*,

- IEEE Standard for Interconnecting Distributed Resources with Electric Power Systems*, no. April. Institute of Electrical and Electronics Engineers, 2009.
- [41] P. Rodriguez, A. V. Timbus, R. Teodorescu, M. Liserre, and F. Blaabjerg, "Flexible active power control of distributed power generation systems during grid faults," *IEEE Trans. Ind. Electron.*, vol. 54, no. 5, pp. 2583–2592, Oct. 2007.
- [42] B. Singh, C. Jain, S. Goel, A. Chandra, and K. Al-Haddad, "A multifunctional grid-tied solar energy conversion system with ANF-based control approach," in *IEEE Transactions on Industry Applications*, 2016, vol. 52, no. 5, pp. 3663–3672.
- [43] E. Pouresmaeil, M. Mehraza, and J. P. S. Catalão, "A multifunction control strategy for the stable operation of DG units in smart grids," *IEEE Trans. Smart Grid*, vol. 6, no. 2, pp. 598–607, Mar. 2015.
- [44] H. Khalil, "Nonlinear systems," Prentice H., New Jersey, 2002, p. ch. 2 and 4.
- [45] S. Strogatz, "Nonlinear dynamics and chaos," Addison-Wesley Publishing Company, 1994, p. 203.
- [46] J. Jacques, E. Slotine, Li, and W., "Applied nonlinear control," New Jersey: Prentice Hall, 1991, p. Ch. 3.
- [47] J. Blackburn, "Symmetrical components for power systems engineering," New York, NY: Marcel Dekker, Inc., 1993, p. ch. 4.
- [48] S. Golestan, M. Monfared, and F. D. Freijedo, "Design-oriented study of advanced synchronous reference frame phase-locked loops," *IEEE Trans. Power Electron.*, vol. 28, no. 2, pp. 765–778, Feb. 2013.
- [49] C. Ma, F. Gao, G. He, and G. Li, "A Voltage Detection Method for the Voltage Ride-Through Operation of Renewable Energy Generation Systems under Grid Voltage Distortion Conditions," *IEEE Trans. Sustain. Energy*, vol. 6, no. 3, pp. 1131–1139, Jul. 2015.
- [50] B. Guha, R. J. Haddad, and Y. Kalaani, "Anti-islanding techniques for Inverter-based Distributed Generation systems - A survey," in *Conference Proceedings - IEEE SOUTHEASTCON*, 2015, vol. 2015–June, no. June, pp. 1–9.
- [51] R. J. Ferreira, R. E. Araújo, and J. A. Peças Lopes, "A comparative analysis and implementation of various PLL techniques applied to single-phase grids," in *Proceedings of the 2011 3rd International Youth Conference on Energetics (IYCE)*, 2011, pp. 1–8.
- [52] Y. Zhang, N. Gatsis, and G. B. Giannakis, "Robust energy management for microgrids with high-penetration renewables," *IEEE Trans. Sustain. Energy*, vol. 4, no. 4, pp. 944–953, Oct. 2013.
- [53] Yingyuan Zhang, Meiqin Mao, Ming Ding, and Liuchen Chang, "Study of energy management system for distributed generation systems," in *2008 Third International Conference on Electric Utility Deregulation and Restructuring and Power Technologies*, 2008, no. April, pp. 2465–2469.
- [54] F. Katiraei and M. R. Iravani, "Power management strategies for a microgrid with multiple distributed generation units," *IEEE Trans. Power Syst.*, vol. 21, no. 4, pp. 1821–1831, Nov. 2006.
- [55] J. M. Carrasco *et al.*, "Power-electronic systems for the grid integration of renewable energy sources: A survey," *IEEE Transactions on Industrial Electronics*, vol. 53, no. 4. pp.

- 1002–1016, Jun-2006.
- [56] E. Afshari *et al.*, “Control Strategy for Three-Phase Grid-Connected PV Inverters Enabling Current Limitation under Unbalanced Faults,” *IEEE Trans. Ind. Electron.*, vol. 64, no. 11, pp. 8908–8918, Nov. 2017.
 - [57] M. Mirhosseini and V. G. Agelidis, “Performance of large-scale grid-connected photovoltaic system under various fault conditions,” in *Proceedings of the IEEE International Conference on Industrial Technology*, 2013, pp. 1775–1780.
 - [58] A.-E. Abdallah and A. Mordi, “Grid-connected photovoltaic systems for grid voltage correction,” in *2014 15th International Conference on Sciences and Techniques of Automatic Control and Computer Engineering (STA)*, 2014, pp. 809–812.
 - [59] G. M. S. Azevedo, P. Rodriguez, M. C. Cavalcanti, G. Vazquez, and F. A. S. Neves, “New control strategy to allow the photovoltaic systems operation under grid faults,” in *2009 Brazilian Power Electronics Conference*, 2009, vol. 1, no. 1, pp. 196–201.
 - [60] M. Mirhosseini, J. Pou, and V. G. Agelidis, “Single-stage inverter-based grid-connected photovoltaic power plant with ride-through capability over different types of grid faults,” in *IECON Proceedings (Industrial Electronics Conference)*, 2013, pp. 8008–8013.
 - [61] J. Miret, M. Castilla, A. Camacho, L. G. De Vicuña, and J. Matas, “Control scheme for photovoltaic three-phase inverters to minimize peak currents during unbalanced grid-voltage sags,” *IEEE Trans. Power Electron.*, vol. 27, no. 10, pp. 4262–4271, Oct. 2012.
 - [62] H. Dehghani Tafti *et al.*, “Study on the unbalanced current injection capability of grid-connected photovoltaic neutral-point-clamped inverter,” in *ECCE 2016 - IEEE Energy Conversion Congress and Exposition, Proceedings*, 2016, pp. 1–6.
 - [63] I. I. Perpinias, N. P. Papanikolaou, and E. C. Tatakis, “Applying fault ride through capability to single phase grid connected PV systems,” in *2015 17th European Conference on Power Electronics and Applications, EPE-ECCE Europe 2015*, 2015, pp. 1–10.
 - [64] F.-J. Lin and K.-C. Lu, “Design of Fuzzy Probabilistic Wavelet Neural Network Controller and Its Application in Power Control of Grid-Connected PV System During Grid Faults,” *2016 IEEE Int. Conf. Fuzzy Syst. (FUZZ-IEEE), Vancouver, BC*, pp. 1725–1732, Jul. 2016.
 - [65] F. A. S. Neves, M. Carrasco, F. Mancilla-David, G. M. S. Azevedo, and V. S. Santos, “Unbalanced grid fault ride-through control for single-stage photovoltaic inverters,” *IEEE Trans. Power Electron.*, vol. 31, no. 4, pp. 3338–3347, Apr. 2016.
 - [66] C. H. Benz, W. T. Franke, and F. W. Fuchs, “Low voltage ride through capability of a 5 kW grid-tied solar inverter,” in *Proceedings of EPE-PEMC 2010 - 14th International Power Electronics and Motion Control Conference*, 2010.
 - [67] H. M. Hasanien, “An Adaptive Control Strategy for Low Voltage Ride Through Capability Enhancement of Grid-Connected Photovoltaic Power Plants,” *IEEE Trans. Power Syst.*, vol. 31, no. 4, pp. 3230–3237, Jul. 2016.
 - [68] Y. Li, X. Yang, W. Chen, T. Liu, and F. Zhang, “Neutral-Point Voltage Analysis and Suppression for NPC Three-Level Photovoltaic Converter in LVRT Operation under Imbalanced Grid Faults with Selective Hybrid SVPWM Strategy,” *IEEE Transactions on Power Electronics*, pp. 1–1, 2018.
 - [69] F. Blaabjerg, R. Teodorescu, M. Liserre, and A. V. Timbus, “Overview of control and grid

- synchronization for distributed power generation systems,” *IEEE Transactions on Industrial Electronics*, vol. 53, no. 5, pp. 1398–1409, Oct-2006.
- [70] A. N. A. Ali, M. H. Saied, M. Z. Mostafa, and T. M. Abdel- Moneim, “A survey of maximum PPT techniques of PV systems,” in *2012 IEEE Energytech*, 2012, pp. 1–17.
- [71] A. Soualmia and R. Chenni, “A survey of maximum peak power tracking techniques used in photovoltaic power systems,” in *FTC 2016 - Proceedings of Future Technologies Conference*, 2017, pp. 430–443.
- [72] A. H. El Khateb, N. A. Rahim, J. Selvaraj, and B. W. Williams, “DC-to-DC Converter With Low Input Current Ripple for Maximum Photovoltaic Power Extraction,” *IEEE Trans. Ind. Electron.*, vol. 62, no. 4, pp. 2246–2256, Apr. 2015.
- [73] C. 21 IEEE Standards Coordinating, *IEEE Guide for Design, Operation, and Integration of Distributed Resource Island Systems with Electric Power Systems*, no. July. Institute of Electrical and Electronics Engineers, 2011.
- [74] H. Komurcugil, S. Bayhan, and H. Abu-Rub, “Lyapunov-function based control approach with cascaded PR controllers for single-phase grid-tied LCL-filtered quasi-Z-source inverters,” in *2017 11th IEEE International Conference on Compatibility, Power Electronics and Power Engineering, CPE-POWERENG 2017*, 2017, pp. 510–515.
- [75] M. Mehrasa, E. Pouresmaeil, and J. P. S. Catalao, “Direct lyapunov control technique for the stable operation of multilevel converter-based distributed generation in power grid,” in *IEEE Journal of Emerging and Selected Topics in Power Electronics*, 2014, vol. 2, no. 4, pp. 931–941.
- [76] R. R. Behera and A. N. Thakur, “An overview of various grid synchronization techniques for single-phase grid integration of renewable distributed power generation systems,” in *International Conference on Electrical, Electronics, and Optimization Techniques, ICEEOT 2016*, 2016, pp. 2876–2880.
- [77] M. Fallah, M. Imani, H. M. Kojabadi, M. Abarzadeh, M. T. Bina, and L. Chang, “Novel structure for unbalance, reactive power and harmonic compensation based on VFF-RLS and SOGI-FLL in three phase four wire power system,” in *2015 IEEE Energy Conversion Congress and Exposition, ECCE 2015*, 2015, pp. 6254–6260.
- [78] C. Jain and B. Singh, “A SOGI-FLL based control algorithm for single phase grid interfaced multifunctional SPV under non ideal distribution system,” in *11th IEEE India Conference: Emerging Trends and Innovation in Technology, INDICON 2014*, 2015, pp. 1–6.
- [79] D. G. Patino, E. G. Erika, J. R. Fuelagan, and E. E. Rosero, “Implementation a HERIC inverter prototype connected to the grid controlled by SOGI-FLL,” in *2015 IEEE Workshop on Power Electronics and Power Quality Applications, PEPQA 2015 - Proceedings*, 2015, pp. 1–6.
- [80] C. A. Busada, S. Gomez Jorge, A. E. Leon, and J. A. Solsona, “Current Controller Based on Reduced Order Generalized Integrators for Distributed Generation Systems,” *IEEE Trans. Ind. Electron.*, vol. 59, no. 7, pp. 2898–2909, Jul. 2012.
- [81] A. Timbus, M. Liserre, R. Teodorescu, P. Rodriguez, and F. Blaabjerg, “Evaluation of current controllers for distributed power generation systems,” *IEEE Trans. Power Electron.*, vol. 24, no. 3, pp. 654–664, Mar. 2009.
- [82] H. K. Khalil, *Nonlinear Systems*, vol. 470. Prentice Hall, 2017.

- [83] S. S. Seyedalipour, H. A. Aalami, and A. Barzegar, "A Lyapunov function-based adaptive fuzzy control for integration of distributed generation resources to electrical networks," in *5th Iranian Joint Congress on Fuzzy and Intelligent Systems - 16th Conference on Fuzzy Systems and 14th Conference on Intelligent Systems, CFIS 2017*, 2017, pp. 184–189.
- [84] Y. K. Wu, J. H. Lin, and H. J. Lin, "Standards and Guidelines for Grid-connected Photovoltaic Generation Systems: a Review and Comparison," *IEEE Trans. Ind. Appl.*, vol. 53, no. 4, pp. 3205–3216, Jul. 2017.
- [85] IEEE Std 929, *IEEE Recommended Practice for Utility Interface of Photovoltaic (PV) Systems*, vol. 2000. Institute of Electrical and Electronics Engineers, 2000.
- [86] C. L. Trujillo, D. Velasco, E. Figueres, and G. Garcerá, "Analysis of active islanding detection methods for grid-connected microinverters for renewable energy processing," *Appl. Energy*, vol. 87, no. 11, pp. 3591–3605, Nov. 2010.
- [87] M. E. Ropp, K. Aaker, J. Haigh, and N. Sabbah, "Using power line carrier communications to prevent islanding," in *Conference Record of the IEEE Photovoltaic Specialists Conference*, 2000, vol. 2000–Janua, pp. 1675–1678.
- [88] C. Abbey, Y. Brissette, and P. Venne, "An autoground system for anti-islanding protection of distributed generation," *IEEE Trans. Power Syst.*, vol. 29, no. 2, pp. 873–880, Mar. 2014.
- [89] P. Pena, A. Etxegarai, L. Valverde, I. Zamora, and R. Cimadevilla, "Synchrophasor-based anti-islanding detection," in *2013 IEEE Grenoble Conference PowerTech, POWERTECH 2013*, 2013, pp. 1–6.
- [90] H. Laaksonen, "Advanced islanding detection functionality for future electricity distribution networks," *IEEE Trans. Power Deliv.*, vol. 28, no. 4, pp. 2056–2064, Oct. 2013.
- [91] A. H. Mohammadzadeh Niaki and S. Afsharnia, "A new passive islanding detection method and its performance evaluation for multi-DG systems," *Electr. Power Syst. Res.*, vol. 110, pp. 180–187, May 2014.
- [92] B. Guha, R. J. Haddad, and Y. Kalaani, "A novel passive islanding detection technique for converter-based distributed generation systems," in *2015 IEEE Power & Energy Society Innovative Smart Grid Technologies Conference (ISGT)*, 2015, pp. 1–5.
- [93] B. Matic-Cuka and M. Kezunovic, "Islanding detection for inverter-based distributed generation using support vector machine method," *IEEE Trans. Smart Grid*, vol. 5, no. 6, pp. 2676–2686, Nov. 2014.
- [94] L. Shi and F. Wu, "An islanding detection algorithm based on fuzzy adaptive phase drift control," in *2013 IEEE International Conference on Information and Automation (ICIA)*, 2013, vol. 1, no. August, pp. 225–229.
- [95] P. K. Dash, M. Padhee, and T. K. Panigrahi, "A hybrid time-frequency approach based fuzzy logic system for power island detection in grid connected distributed generation," *Int. J. Electr. Power Energy Syst.*, vol. 42, no. 1, pp. 453–464, Nov. 2012.
- [96] S. R. Mohanty, P. K. Ray, N. Kishor, and B. K. Panigrahi, "Classification of disturbances in hybrid DG system using modular PNN and SVM," *Int. J. Electr. Power Energy Syst.*, vol. 44, no. 1, pp. 764–777, Jan. 2013.
- [97] M. Heidari, G. Seifossadat, and M. Razaz, "Application of decision tree and discrete wavelet transform for an optimized intelligent-based islanding detection method in distributed

- systems with distributed generations,” *Renew. Sustain. Energy Rev.*, vol. 27, pp. 525–532, Nov. 2013.
- [98] M. S. ElNozahy, E. F. El-Saadany, and M. M. A. Salama, “A robust wavelet-ANN based technique for islanding detection,” in *IEEE Power and Energy Society General Meeting*, 2011, pp. 1–8.
- [99] Sungyul Park, Minho Kwon, and S. Choi, “A new anti-islanding method for indirect current control of grid connected inverter,” in *2017 IEEE 3rd International Future Energy Electronics Conference and ECCE Asia (IFEEC 2017 - ECCE Asia)*, 2017, pp. 1230–1234.
- [100] R. Varier and N. M. Pindoriya, “A novel active anti-islanding protection scheme for grid-interactive roof-top solar PV system,” in *2014 18th National Power Systems Conference, NPSC 2014*, 2015, pp. 1–6.
- [101] C.-C. Hou and Y.-C. Chen, “Active anti-islanding detection based on pulse current injection for distributed generation systems,” *IET Power Electron.*, vol. 6, no. 8, pp. 1658–1667, Sep. 2013.
- [102] M. Tedde and K. Smedley, “Anti-islanding for three-phase one-cycle control grid tied inverter,” *IEEE Trans. Power Electron.*, vol. 29, no. 7, pp. 3330–3345, Jul. 2014.
- [103] W. Cai, B. Liu, S. Duan, and C. Zou, “An islanding detection method based on dual-frequency harmonic current injection under grid impedance unbalanced condition,” *IEEE Trans. Ind. Informatics*, vol. 9, no. 2, pp. 1178–1187, May 2013.
- [104] P. Gupta, R. S. Bhatia, and D. K. Jain, “Average absolute frequency deviation value based active islanding detection technique,” *IEEE Trans. Smart Grid*, vol. 6, no. 1, pp. 26–35, Jan. 2015.
- [105] S. Akhlaghi, A. A. Ghadimi, and A. Akhlaghi, “A novel hybrid islanding detection method combination of SMS and Q-f for islanding detection of inverter-based DG,” in *2014 IEEE Power and Energy Conference at Illinois, PECE 2014*, 2014, pp. 1–8.
- [106] B. Wen, D. Boroyevich, R. Burgos, Z. Shen, and P. Mattavelli, “Impedance-based analysis of active frequency drift islanding detection for grid-tied inverter system,” *IEEE Trans. Ind. Appl.*, vol. 52, no. 1, pp. 332–341, 2016.
- [107] S. Bifaretti, A. Lidozzi, L. Solero, and F. Crescimbeni, “Anti-Islanding Detector Based on a Robust PLL,” *IEEE Trans. Ind. Appl.*, vol. 51, no. 1, pp. 398–405, Jan. 2015.
- [108] J. Stevens, R. Bonn, J. Ginn, and S. Gonzalez, “Development and Testing of an Approach to Anti-Islanding in Utility-Interconnected Photovoltaic Systems,” *Other Inf. PBD 1 Aug 2000*, no. August, p. 58, Aug. 2000.

9.

APPENDIX

9.1 Lyapunov stability analysis of LCO

Since (3.1b) is decoupled from (3.1a), the fixed point $r = A$ of (3.1a) can be analyzed. Then, a Lyapunov function for (3.1a) is:

$$V = \left(1 - \frac{r^2}{A^2}\right)^2 \frac{A^2 \omega}{4} \quad (9.1)$$

which $V(A) = 0$ and $V(r) > 0$ in the domain $D_L - \{A\}$ with $D_L = \{r > 0, \omega > 0\}$. Furthermore:

$$\dot{V} = - \left(\left(1 - \frac{r^2}{A^2}\right) r \omega \right)^2 \quad (9.2a)$$

which is:

$$\dot{V}(r) < 0 \quad (9.2b)$$

in $D_L - \{A\}$ and it can be rewritten with (3.1a) as:

$$\dot{V} = -\dot{r}^2. \quad (9.2c)$$

Then, the fixed point $r = A$ of (3.1a) is asymptotically stable.

9.2 Technical specifications

In this section, it can be seen physical details about the experimental setup and the different components of the instrumentation elements used for the experimental part. The different parts of the experimental setup are depicted in Figure 9.1.

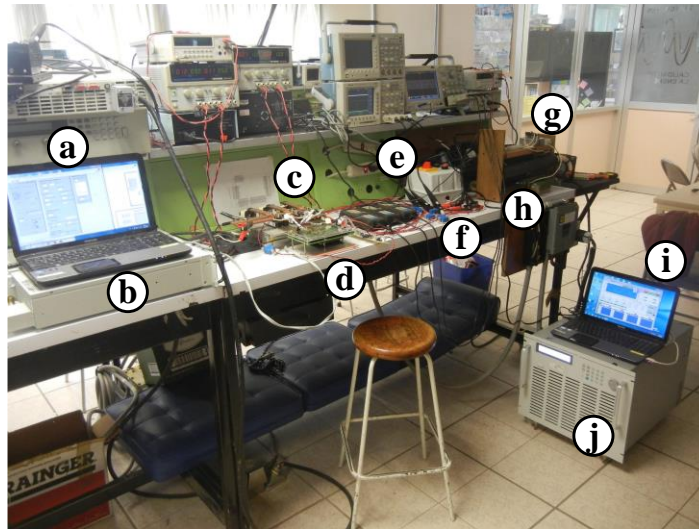


Figure 9.1. Experimental setup. (a) LabView main control panel. (b) N8937APV Agilent PV array simulator. (c) Inverter. (d) FPGA Xilinx Spartan-6 LX45. (e) PCC. (f) Current and voltage sensors. (g) Nonlinear load. (h) Dump load. (i) Control panel for AC source. (j) Chroma 61700 AC power source.

The three-phase inverter, its inductors, amplifiers, and the control board used for experimental purposes are shown in detail in Figure 9.2.

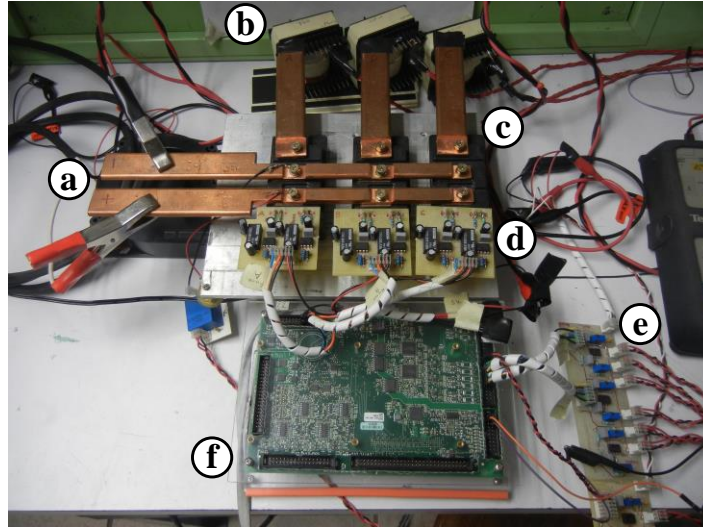
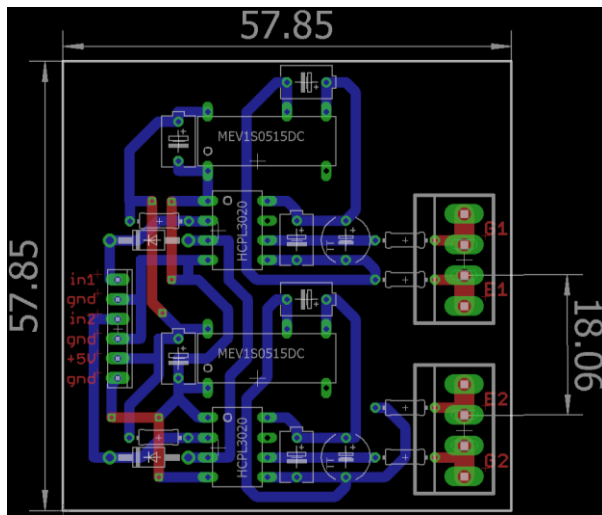


Figure 9.2. Main parts of the inverter and instrumentation. (a) DC bus input. (b) Inductors. (c) CM75DU-12H Powerex IGBT module. (d) IGBT driver. (e) Current and voltage amplifiers. (f) FPGA Xilinx Spartan-6 LX45.

Moreover, the printed circuit board (PCB) of the IGBT driver, and its different elements mounted on it, are depicted in Figure 9.3.



(a)



(b)

Figure 9.3. IGBT driver. (a) Printed Circuit Board (PCB). (b) Electronic elements mounted in the PCB.

Furthermore, the PCBs for the current and voltage sensors used in the experimental section, and the amplifiers used to connect the sensors to the control board, are shown in Figure 9.4.

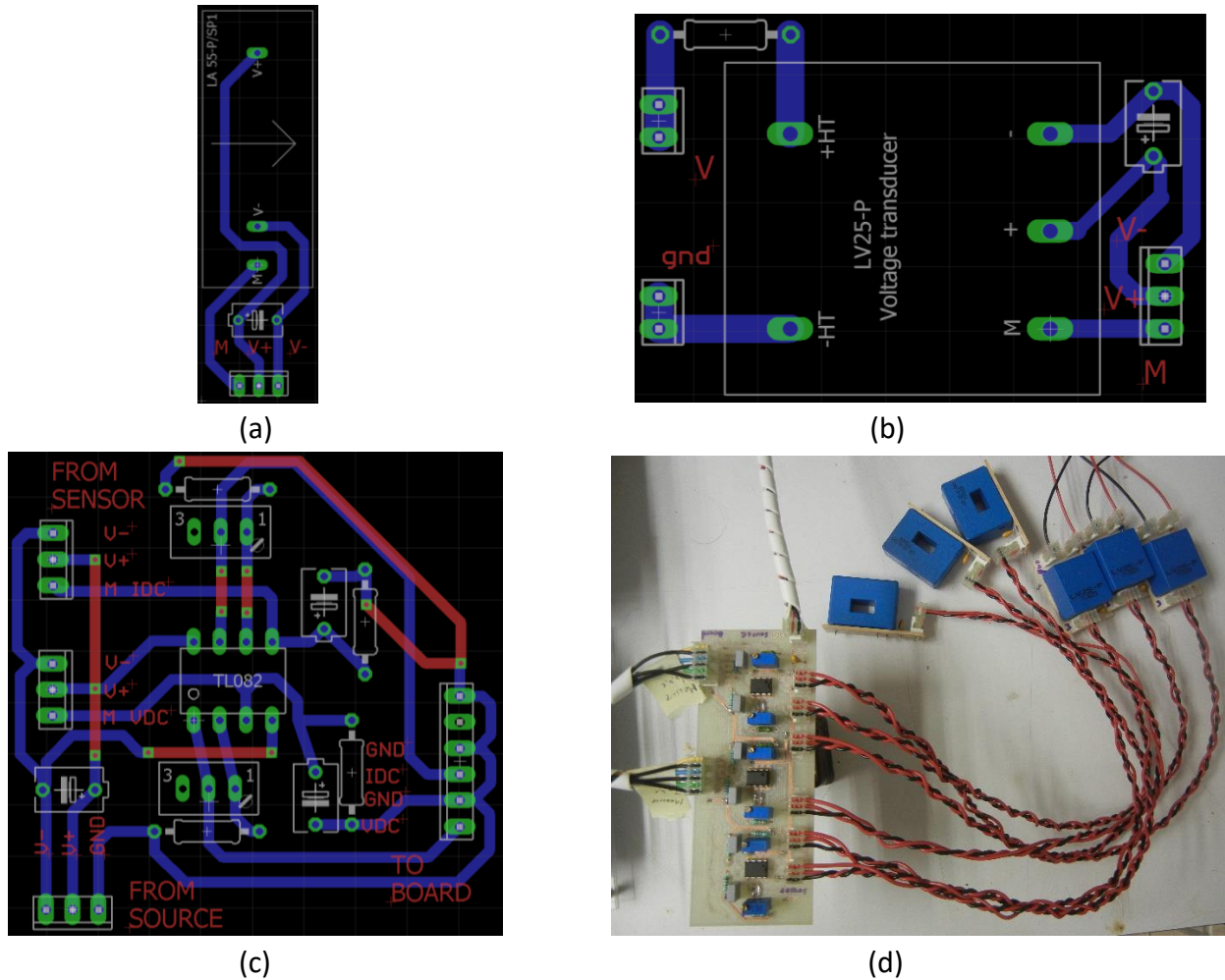


Figure 9.4. Current and voltage sensors, and amplifiers. (a) PCB of current sensor. (b) PCB of voltage sensor. (c) PCB of voltage amplifier. (d) Amplifiers connected with current and voltage sensors.

Finally, the block diagram of the LCO-FLL implemented in LabView is depicted in Figure 9.5.

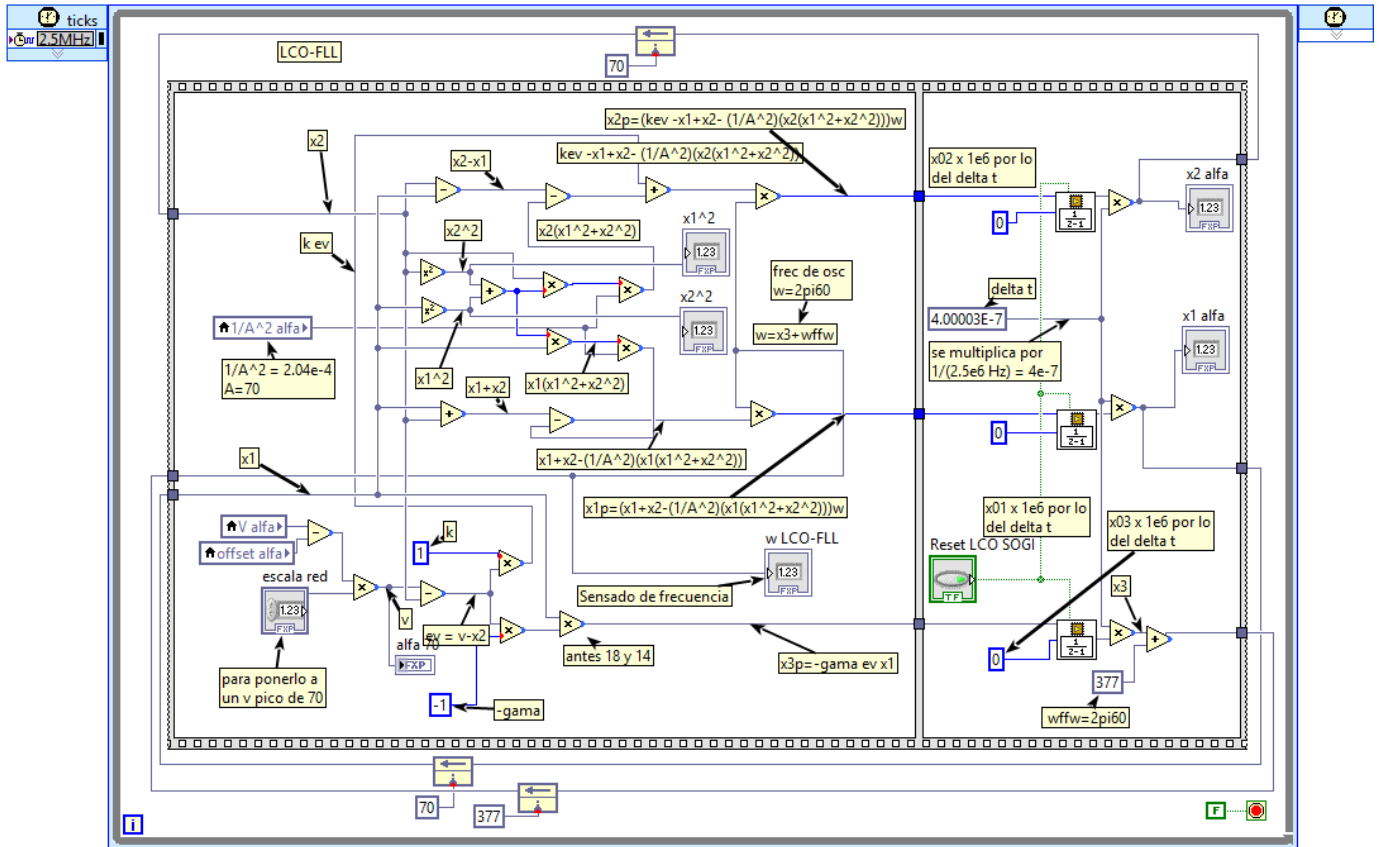


Figure 9.5. Block diagram of the LCO-FLL implemented in LabView.